Development of Wireless Position Trackable Sensors Enabling Instant Pervasive Sensing

Submitted to
Graduate School of Information Science and Technology
Osaka University

January 2021

Ryo SHIRAI

Publications

Journal Articles (Refereed)

[J1] Ryo Shirai and Masanori Hashimoto, "DC Magnetic Field Based 3D Localization with Single Anchor Coil," *IEEE Sensors Journal*, vol. 20, no. 7, pp. 3902–3913, 2020.

International Conference Papers (Refereed)

[I1] Ryohei Shimizu, Ryo Shirai, and Masanori Hashimoto, "Position and Posture Estimation of Capsule Endoscopy with a Single Wearable Coil Toward Daily Life Diagnosis," in *Proceedings of International Midwest Symposium on Circuits and Systems (MWSCAS)*, pp. 57–60, August 2020.

[I2] Pei Hao Chen, Ryo Shirai, Masanori Hashimoto, "Coverage-scalable Instant Tabletop Positioning System with Self-localizable Anchor Nodes," in *Proceedings of the 24th International Conference on Intelligent User Interfaes (IUI2019)*, pp. 57–58, March 2019.

[I3] Ryo Shirai, Tetsuya Hirose, and Masanori Hashimoto, "A Multifunctional Sensor Node Sharing Coils in Wireless Power Supply, Wireless Communication and Distance Sensing Modes," in *2018 16th IEEE International New Circuits and Systems Conference (NEWCAS)*, pp. 152–156, June 2018.

[I4] Ryo Shirai, Tetsuya Hirose, and Masanori Hashimoto, "Dedicated Antenna Less Power Efficient OOK Transmitter for mm-Cubic IoT Nodes," in *Proceedings of the 47th European Microwave Conference (EuMC)*, pp. 101–104, October 2017.

[I5] Ryo Shirai, Jin Kono, Tetsuya Hirose, and Masanori Hashimoto, "Near-Field Dual-Use Antenna for Magnetic-Field Based Communication and Electrical-Field Based Distance Sensing in mm^3 -Class Sensor Node," in *Proceedings of IEEE International Symposium on Circuits and Systems (ISCAS)*, pp. 124–127, May 2017.

International Conference Paper (Nonrefereed)

[C1] Masanori Hashimoto, Ryo Shirai, Yuichi Itoh, and Tetsuya Hirose, "Toward Real-Time 3D Modeling System with Cubic-Millimeters Wireless Sensor Nodes (Invited)," in *Proceedings of IEEE International Conference on ASIC (ASICON)*, pp. 1087–1091, October 2017.

Domestic Conference Paper (Nonrefereed)

[D1] Ryo Shirai, Pei Hao Chen, Ryohei Shimizu, and Masanori Hashimoto, " DC Magnetic Field Based Localization with Single Anchor Coil," *IEICE technical report*, vol. 118, no. 373, pp. 11–14, December 2018. (in Japanese)

[D2] Ryohei Shimizu, Ryo Shirai, Pei Hao Chen, and Masanori Hashimoto, "Motion prediction using time-series data of geomagnetic sensor array," *IEICE technical report*, vol. 118, no. 373, pp. 55–58, December 2018. (in Japanese)

[D3] Ryo Shirai, Jin Kono, Tetsuya Hirose, and Masanori Hashimoto, "Near-Field Dual-Use Antenna for Magnetic-Fied Based Communication and Electrical-Field Based Distance Sensing in mm^3-Class Sensor Node," *IEICE technical report*, vol. 117, no. 343, pp. 101–105, December 2017. (in Japanese)

[D4] Ryo Shirai, Tetsuya Hirose, and Masanori Hashimoto, "Dedicated Antenna Less Power Efficient OOK Transmitter for mm-Cubic IoT Nodes," *IEICE technical report*, vol. 117, no. 343, pp. 159–163, December 2017. (in Japanese)

Summary

Ambient intelligence (AmI) is an environment that allows us to take advantage of information gathered by distributed devices without making us aware of them. AmI technology is expected to significantly improve our quality of life (QoL) by utilizing ambient information that has never been used and fed back to us so far. There are various types of information that surround us, and they can be ultimately divided into two types: information that we are usually aware of or not. For example, the information that should be aware of includes Todo list, medical checkup, parking location, meeting schedule, and we manage them each time. On the other hand, we do not usually perceive where and when we used daily necessities, how long to whom we talked, in what posture we spent a day, etc. However, once we lose our property, or when we want to select the meeting participants most effectively, the information mentioned above will be needed immediately. AmI gathers these information unconsciously and contributes to improve our QoL by providing not only gathered but also processed information to us.

The pervasive sensing technology supports AmI's information gathering from the hardware layer. AmI gathers information through the sensor node of pervasive sensing and processes it with the assistance of other technology (e.g. artificial intelligence, big data analysis, etc.). After information processing, AmI presents information to us and controls devices on behalf of us, sometimes with the sensor nodes also used for information gathering. Therefore, sensor nodes utilized in pervasive sensing directly engage in information in/output. Conventionally, to introduce the pervasive sensing into our environment, application-specific sensor nodes should be designed and implemented first. However, these application specific sensor nodes cannot be diverted to other application, and hence the cost of introducing pervasive sensing into a new environment is high. To address this issue, this dissertation proposes the concept of "instant pervasive sensing," which allows us to introduce pevasive sensing into the environment only by attaching the "instant pervasive sensor." Sensor nodes for instant pervasive sensing are equipped with basic components which are required for all applications, and can be upgraded with additional components for application-specific purposes. The following explains the basic components required for the sensor node for instant pervasive sensing.

Sensor nodes for instant pervasive sensing have to prevent the user from being distracted when acquiring information and presenting information to the user; otherwise, the obtained information could be highly biased. Hence, the ideal sensor node for in-

stant pervasive sensing should work properly even without our recognition of its existence, which means the sensor node should be implemented as small as possible and also should be maintenance free. The sensor node for instant pervasive sensing should be equipped with a computation circuit, a communication circuit, a power management circuit, and sensing circuits. For the computation and sensing, mm^3 to cm^3-class high-performance circuits have being realized thanks to the advancement of CMOS and MEMS technology. As for the communication circuit and the power management circuit, on the other hand, there are still room to be studied. Recently, wireless sensor nodes are highly demanded to remove the restriction on the installation location of sensor nodes and to make those nodes maintenance free. However, research on wireless sensor nodes is not conducted sufficiently since original pervasive sensing utilized wired sensor nodes and conventional research supposed wired nodes. To make sensor node wireless and maintenance free, the sensor node should be equipped with the wireless communication circuit as well as the wireless power transfer (WPT) circuit. These wireless communication function and WPT function are first two basic components and discussed in this dissertation in first two chapters.

Although wireless communication methods for tiny sensor nodes are aggressively studied, the size of the transmitter of conventional research cannot be smaller than the volume of the antenna. The size of antenna is determined by the wavelength of the signal, and hence cannot be smaller without deteriorating the radiation efficiency. Here is the another challenge on the wireless transmitter for instant pervasive sensing; the transmitter should be not only small but also energy efficient since the capacity of the battery or energy source equipped to the sensor node is highly limited. To address these issues, this dissertation proposes a compact wireless transmitter that uses coils for radiation as well as oscillation, eliminating the need for an external antenna. In addition to proposing the transmitter structure, this dissertation introduces the energy efficient baseband encoding method to reduce the energy consumption per bit to less than 100 pJ/b even with the energy consuming carrier wave based communication.

As for WPT, the system required for instant pervasive sensing is the 1-to-n WPT system while conventional research mainly focuses on 1-to-1 WPT system. In 1-to-1 WPT system, one power transmitter is responsible for one power receiver. Research on this 1-to-1 WPT system has been conducted over decades, and many findings on efficiency and robustness improvement are reported. On the other hand, 1-to-n WPT system is less discussed since few applications are available so far and is in low demand unlike 1-to-1 WPT system which is already commercially available. Although conventional applications did not require the 1-to-n WPT system, the pervasive sensing highly demands 1-to-n WPT system since the number of the sensor nodes in the system is huge compared to conventional systems. A major challenge is that the feasibility is unknown and even the analytical key equations of the 1-to-n WPT system are not available. To address this issue, this dissertation discusses the feasibility of the 1-to-n WPT systems based on the analysis of both the circuit and the magnetic field. The the-

oretical analysis reveals that the sensor nodes of instant pervasive sensing application can receive sufficient power while the coupling coefficient is very low and even close to 0 as long as the circuit constants are set appropriately. In addition, this dissertation proposes and evaluates a suitable WPT receiver circuit structure for the sensor node in instant pervasive sensing application. Adopting Junction FET as the switching element enables to connect two coils even when the node is out of energy, realizing a structure that automatically switches to the WPT mode.

Apart from the requirement on the sensor volume, sensor nodes for instant pervasive sensing should be equipped with the localization function as well as a basic component since the value of information elevates significantly when it is associated with the location information. Also, the expected human-computer interaction greatly depends on its location and surrounding environment, and hence the location of the sensor node should be acquired. Conventional localization methods suffer from two major problems: robustness and installation cost problem. The robustness inherently depends on the type of signals to be utilized for localization. For instance, camera based localization methods suffer from the occlusion problem and AC magnetic field based methods cannot tolerate daily non-ferrous metallic material. The installation cost problem is mainly caused by the number of anchor nodes required for localization. Conventional methods require more than one, sometimes dozens of accurately installed anchor nodes, and hence the installation cost is high and instant pervasive sensing cannot be achieved. To solve these issues, this dissertation proposes a DC magnetic field based 3D localization method with single anchor coil. The proposed localization method can achieve less than 15 cm localization error in room scale and can achieve even less than 1 cm accuracy on the tabletop.

As described above, sensor nodes for instant pervasive sensing should be equipped with sensing circuits in addition to three basic components: wireless communication, 1-to-n WPT, and localization, as described above. On the other hand, the information of the location and movement of the sensor node is an important information itself, and hence can be utilized for AmI since AmI takes advantage of all information surrounding us. The sensor node only with three basic components described above can provide motion tracking as a basic function, and shall greatly contribute to AmI. Besides, currently available motion tracking methods require the installation of dedicated equipment and the environment for a specific purpose, which cannot be easily diverted to other systems. To address this issue, this dissertation proposes a DC magnetic field-based 6-DoF motion tracking method with a single reference node expanding the localization method proposed in this dissertation. Experimental results showed that the proposed method can estimate the 3-DoF sensor posture of the sensor node with the maximum error of 1.65 degrees and achieved the 3-DoF position estimation with the maximum error of 9.69 mm in the range of 350mm from the reference node. Evaluations on example applications revealed that the motion tracking of the sensor node, which is a basic function of the sensor node, can contribute to the AmI, and thus the effectiveness of the wireless

trackable sensor for instant pervasive sensing is confirmed.

Acknowledgments

First of all, I would like to express my deepest gratitude to Professor Masanori Hashimoto in Osaka University for providing me a precious opportunity and an excellent environment to study as a doctoral student in his laboratory. All of my productive researches are credited to none other than him. His advanced perspective and thoughtful advice led me to the achievements.

I would like to appreciate Professor Haruo Takemura, Professor Noriyuki Miura, and Associate Professor Yuichi Itoh in Osaka University for detailed reviews and insightful suggestions.

I would like to appreciate Professor Takao Onoye, Professor Tetsuya Hirose, Associate Professor Ittetsu Taniguchi in Osaka University, and Associate Professor Jaehoon Yu in Tokyo Institute of Technology for the precious suggestions and enormous help throughout my doctoral research.

My appreciation also goes to Associate Professor Akira Tsuchiya in The University of Shiga Prefecture and Ms. Kaori Matsumoto in Kobe University for technical discussions and suggestions on the wireless transmitter circuit and CMOS chip design.

I would like to express my sincere appreciation to Assistant Professor Yutaka Masuda in Nagoya University, and Assistant Professor Wang Liao in Kochi University of Technology, for precious discussions and support.

I would like to thank other colleagues who belong or belonged to the Integrated System Design Laboratory in Osaka University for daily discussions and their support: Dr. Tomoki Sugiura, Dr. Koichi Mitsunari, Dr. Jun Chen, Dr. Ryutaro Doi, Mr. Tai-Yu Cheng, Mr. Pei-Hao Chen, Mr. Ryohei Shimizu, Mr. Yuichiro Neo, and Mr. Dehua Liang. I express my heartfelt thanks to all members of the Integrated System Design Laboratory in Osaka University for having an interesting and comfortable time in the laboratory. I would like to thank laboratory secretaries Ms. Asako Murakami and Ms. Naoko Isozaki for their various support.

I appreciate the financial support from the Japan Society for the Promotion of Science.

I would like to extend my gratitude to my mother Masako, my brother Ken, other relatives, and my friends. They always support me and encourage me with their best wishes, inspiration, and suggestion.

Finally, I hope my gratitude will reach to my father, Dr. Satoshi Shirai in heaven.

Contents

List of Figures

List of Tables

Abbreviations

AI	Artificial Intelligence
AmI	Ambient Intelligence
APT	Acoustic Power Transfer
ASK	Amplitude Shift Keying
BLE	Bluetooth Low Energy
CMOS	Complementary MOS
CPT	Capacitive Power Transfer
CU	Coding Unit
DoF	Degree of Freedom
ENIAC	Electronic Numerical Integrator And Computer
FET	Field Effect Transistor
FM	Frequency Modulation
FOD	Foreign Object Detection
GPS	Global Positioning System
HCI	Human Computer Interaction
HII	Human Information Interaction
IoT	Internet of Things
IPT	Inductive Power Transfer
JFET	Junction FET

LBS	Location Based Service
LC OSC	Inductor-Capacitor OSC
LOD	Living Object Detection
LUT	Look Up Table
MCU	Micro Controller Unit
MEMS	Micro Electro Mechanical Systems
ML	Machine Learning
MOS	Metal Oxide Semiconductor
MPT	Microwave Power Transfer
OOK	On-Off-Keying
OPT	Optical Power Transfer
OSC	Oscillator
Q-factor	Quality-factor
QoL	Quality of Life
RANSAC	Random Sample Consensus
RC OSC	Resistor-Capacitor OSC
RF	Radio Frequency
RFID	Radio Frequency Identifier
RSS	Received Signal Strength
S-P	Series-Parallel
S-S	Series-Series
SNR	Signal to Noise Ratio
ToF	Time of Flight
UHF	Ultra High Frequency
VHF	Very High Frequency
WPT	Wireless Power Transfer

Chapter 1

Introduction

This dissertation focuses on developing tiny wireless position trackable sensors which can instantly change our daily environment into the smart environment based on the pervasive sensing technology. This chapter describes the research background and objectives of this dissertation. Section 1.1 describes the history and background of pervasive sensing and how pervasive sensing can contribute to ambient intelligence (AmI) and Internet of things (IoT), which are both expected to improve our quality of life (QoL). Section 1.2 introduces the concept of "instant pervasive sensing", which is proposed in this dissertation, and describes required components and functions for the sensor required for instant pervasive sensing. Section 1.3 introduces the related work on element technologies for instant pervasive sensing and points out issues preventing us from actualizing instant pervasive sensing. Section 1.4 summarizes current issues of conventional work and introduces major challenges of this research. Finally, the objectives and overall organization of this dissertation are presented in Section 1.5.

1.1 Background

Over the decades, research on the volume reduction technology of electronic devices is aggressively conducted. In particular, the development of scaling technology for computers and processors is outstanding. ENIAC [1, 2], which was the first general-purpose electronic computer developed in 1946, required an implementation area of 167 m^2 or 1800 sq ft [3], while as of 2020, a processor chip with tens of millions of times the computing performance of ENIAC has been realized in an area of several dozens of mm^2 or even less. Not only computation units but also sensors and actuators that are in charge of information in/output are aggressively being miniaturized. In 1967, Harvey C. Nathanson et al. introduced device manufacturing with Micro Electro Mechanical Systems (MEMS) technology based on the advanced semiconductor technology [4]. With this MEMS technology, sensors and actuators are now possibly implemented on a silicon die whose size is also several mm^2 although those sensors and actuators were

originally required a size of several dozens of cm^3 or more decades ago.

Taking advantage of these device miniaturization technologies, the concept of "*disappearing computer*" is proposed and several projects under this concept started in European Union (EU) in 2001 [5]. An objective of this concept was to actualize the Human-Computer-Interaction (HCI) and Human-Information-Interaction (HII) without letting us perceive the existence of computers or devices. Therefore, the word of "disappearing" does not necessarily mean that the device becomes invisible as it becomes smaller while the volume reduction of the device to some extent is necessary. Rather than that, "disappearing" means that we will not be able to recognize individual devices because everything around us is sensed unknowingly, while, of course, some devices will be literally invisible with the small-volume implementation technology in the future. In this context, the required criteria of device miniaturization is about mm^3 to cm^3 volume while the device volume of several mm^3 to cm^3 is visible for us. In addition to the device miniaturization, method and knowledge on how to sense every stuffs or persons around us are also an important factor for actualizing the unconscious HCI and HII.

Ambient intelligence (AmI) can be treated as an extended concept of disappearing computer. AmI aims to actualize an environment in which our living environment is unknowingly sensed and persons control the environment not manually but unconsciously through information manipulation [6–9]. The environment that adopts AmI technology is called a smart environment. Smart home and smart city, which are becoming trend terms in recent years, denote the home and city which adopt smart environment, respectively. As a similar concept, Internet of Things (IoT) has been proposed. IoT senses the information of all objects surrounding us and connecting the acquired information through the internet [10, 11]. A lot of IoT research has been conducted focusing on how to gather information and which information should be acquired from environments [12]. In contrast, AmI aims not only to directly use the gathered information but also to process and utilize the information with the help of, for example, machine learning (ML)-based artificial intelligence (AI) and huge database stored in advance. Besides, AmI takes advantage of the information from not only "things" but also the behavior of persons, each person's habits, and thought presumed from his/her behavior, etc. Therefore, IoT, which mainly focuses on gathering and exchanging information each other, can be regarded as an infrastructure that supports AmI. The smart environment is an application of the most advanced technologies available at the time. In the past, smart environments were built with IoT-based technologies, but are now being replaced by AmI-based technologies, which have a higher degree of freedom. With the emergence of more comprehensive concepts in the future, AmI may hand over the position as a technology utilized for smart environment to a new technology. At present, AmI is a comprehensive concept that takes advantage of other technologies. The technology that supports AmI from the lower layers is the sensing technology improved with the development of IoT technology.

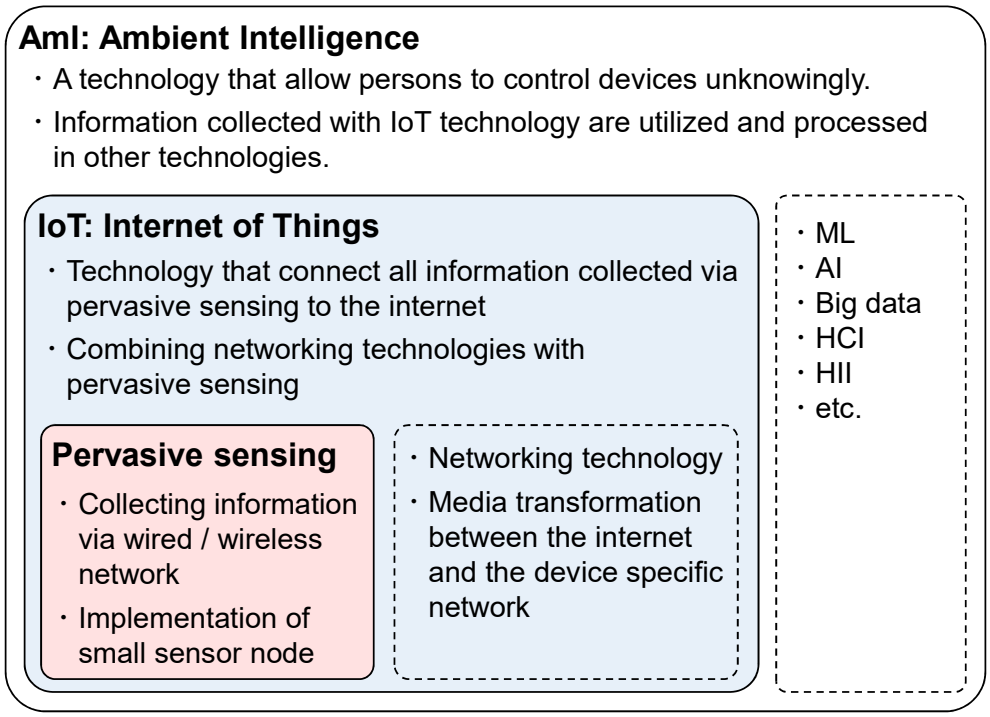

Figure 1.1: Relationship between AmI, IoT, and pervasive sensing.

Notably, pervasive sensing technology can be regarded as the fundamental technology supporting IoT. Fig. 1.1 clarifies the difference between the word of AmI, IoT, and pervasive sensing. Fig. 1.1 describes that AmI is supported by IoT technology in terms of the interconnection of information. In pervasive sensing, wired or wireless sensor nodes installed in various environment (e.g. our daily environment, factory, office, etc.) are in charge of collecting information, and they support IoT and AmI from the hardware layer. For this reason, the performance of the feasible smart environment based on AmI or IoT greatly depends on the performance of pervasive sensing.

Conventionally, sensor nodes utilized in various applications are designed for each specific purpose and could not be diverted for other purposes. In advance to the sensor design, the user needs to scrutinize the installation location of these sensor nodes and the information to be collected. The sensor nodes must be designed and implemented to meet the specific requirements determined by the user. The information acquired by the sensor should be associated with the position information of the sensor to its practical use, which will be explained later. As for application specific sensor nodes, the installation location is known and may not change, and therefore the sensor node does not necessarily have to estimate its own position. In addition to this, wired connection may be used for communication and energy supply depending on the location of the sensor node. Furthermore, the number of these application specific sensor nodes is limited, and hence regular maintenance can be performed by the user.

On the other hand, these application specific sensor nodes significantly limit the application area. J. Wilkins points out that to achieve practical pervasive sensing, sensor nodes should be robust and should not require maintenance or calibration once installed [13]. However, sensor nodes for pervasive sensing, which have these characteristics, also require an intensive preliminary investigation for their installation. Therefore, the installation cost for introducing pervasive sensing in our daily environment is still high.

1.2 Instant pervasive sensing

To solve the introduction cost problem of pervasive sensing, this work proposes the concept of "instant pervasive sensing." The objective of the proposed instant pervasive sensing concept is to enable us to install sensor nodes to everywhere without intensive site survey. Besides, the instant pervasive sensing concept allows us to instantly transform things around us into devices that can acquire information. This work divides the functions of sensor nodes required for instant pervasive sensing into two classes: one is the basic functions, which are required for all sensor nodes, and the other is the application specific functions. Basic functions are embedded into all sensor nodes for instant pervasive sensing, and therefore, they should be actualized first. Here, the sensor node for pervasive sensing is generally equipped with following circuits and these are regarded as basic functions: a computation circuit, a communication circuit, a power management circuit, and sensing circuits. Similar to the concept of "disappearing computer," pervasive sensing aims to gather information without disturbing user experience [14, 15]. Therefore, the ideal sensor node for pervasive sensing should work properly even without our recognition of its existence, which means basic functions should be implemented as small as possible and also should be maintenance free. The following discusses on challenges and requirements on each circuit.

The first three circuits are the minimum requirements for sensor nodes of pervasive sensing and should be implemented as small as possible for us not to perceive the existence of sensor nodes. Fortunately, aggressive CMOS scaling technology has enabled us to implement the computation circuit even in mm^3-class volume with sufficient computation power keeping the energy consumption low. Similarly, many of the sensing circuits can be also implemented in mm^3 to cm^3 class volume with the advanced MEMS technology as described above. However, as for the communication and power management circuits, there are still room to be studied since the sensor node should work wirelessly to keep the sensor node maintenance free and the findings on conventional wired-application are no longer sufficient.

In the context of original pervasive sensing, each sensor node does not necessarily have to be connected to the network wirelessly as explained above. On the other hand, the wired sensor nodes severely limit the installation location which losses the pervasiveness consequently. Therefore, the sensor nodes in the instant pervasive sens-

ing should be connected to the network wirelessly. When we remove the cable that connects to the sensor nodes, the problem about the power supply to each node also appear at the same time. To keep the sensor node wireless in terms of both communication and power supply, both wireless communication function and wireless power transfer (WPT) function are indispensable. To keep the introduction cost of the instant pervasive sensing to the low level, the number of communication and power transmission hosts should be small as possible. Even when we introduce instant pervasive sensors to the indoor environment, which require a shorter communication range and power transmission range compared to outdoor environment, each sensor node should work properly at the range of several meters from the host node.

To apply instant pervasive sensing technologies to AmI or IoT, the concept of location-based service (LBS) gains its importance [16,17] since the value of information elevates significantly when it is associated with the location information [18]. C. Perera et al. point out the importance of position estimation of an object because advanced HCI greatly depends on its location and surrounding environment [17]. LBS plays an important role even when fusing the IoT and other new technologies. B. K. Kim et al. report that the estimation of object position facilitates the introduction of robot technology into our living environment [19]. Thus, detecting the position of an object is expected to promote various location-based services in our living environment and enhance our QoL. The sensor node for conventional pervasive sensing applications is installed to the specific position, and hence the installation location of the sensor node is known beforehand. On the other hand, the sensor node for instant pervasive sensing, which allows users to instantly attach sensor nodes to objects and persons, the sensor location is unknown at the point when the sensor is designed and implemented. For this reason, the sensing circuit should contain not only the function for gathering information, but also the function of localization for practical instant pervasive sensing. As described above, the distance between the host node and sensor node can be several meters even in indoor environment. In indoor environment, the localization error of several cm should be achieved since the distance between persons and objects is at most dozens of centimeters.

Based on these discussions, this work concludes that the following element technologies should be further studied to actualize instant pervasive sensing.

- Meter scale wireless communication
- Meter scale WPT
- Meter scale localization with the error of several cm

The great challenge among actualizing these functions is that all of these functions have to be implemented in at most several cm^3 volume not to limit the installation location of sensor nodes and disturb user experiences as described above. Following Section 1.3 will introduce related work on each of wireless communication, WPT, and localization of the sensor node.

1.3 Related work

As discussed in the previous section, performances of wireless communication, WPT, and localization function of the sensor node should be improved to actualize the instant pervasive sensing. Therefore, Sections 1.3.1, 1.3.2, and 1.3.3 introduce related work on each of these three element technologies. Section 1.3.4, on the other hand, introduces the AmI technologies that utilize the motion information of things or persons and explains that AmI can enhance our QoL if the instant position trackable sensor is actualized.

1.3.1 Wireless communication

As described in the previous section, small volume nodes are desirable since they can be attached to everything around us, and millimeter-cubic class nodes have the potential to change our life significantly. To eliminate restrictions on the installation location of sensors used in pervasive sensing, the small volume nodes should be equipped with wireless communication function. On the other hand, in many cases, integrating a high-performance transmitter is extremely difficult since the size of the nodes is extremely small. Fortunately, high communication speed is not demanded in most of AmI applications, especially for small volume sensor nodes. Rather, low power operation is more important than the communication performance since each node is expected to operate for a long time with a compact and small capacity battery. For example, if the sensor circuit continues to consume 100 μW of power, the non-rechargeable Li-Fe battery whose volume is 1 cm^3 will not last for 6 months [20]. Even when the power is wirelessly provided via WPT function and the transmitter operates intermittently, the amount of energy stored in such a small volume is highly limited, and low energy operation is indispensable. The above discussion suggests that the following features are required for small wireless nodes for instant pervasive sensing.

- Low standby power
- Low energy per bit
- Small volume

The first two standby power and energy per bit problems are related to each other. The most effective way to reduce standby power is to enable the transmitter only during wireless communication and disable the transmitter immediately after the end of communication. Similarly, reducing the time of a symbol, which represents a 1-bit signal, as short as possible is effective from the viewpoint of minimizing energy per bit. As a communication method which satisfies both of these characteristics, the inductive coupling-based communication method has been proposed and research on it has been actively conducted [21–25]. As another method, the carrier wave-based communication, which is the general communication method, is also actively studied toward actualizing small volume transmitter. The following will discuss the detail of each communication

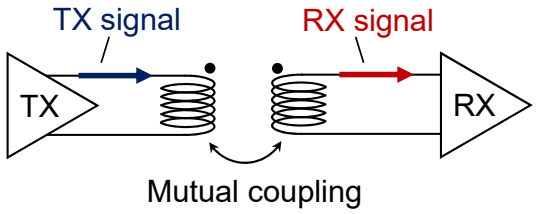

Figure 1.2: Basic circuit structure of the inductive coupling based transceiver.

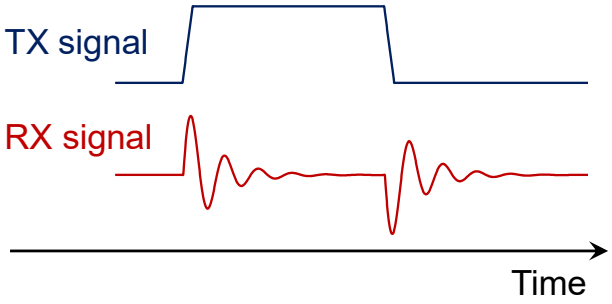

Figure 1.3: General waveform of signals utilized and observed in the inductive coupling based communication.

method.

Inductive coupling-based communication

Fig. 1.2 shows the general structure of the inductive coupling-based communication system. In inductive coupling-based communication, the transmitter applies a short pulse signal to the coil inside the node as shown in Fig. 1.3. The receiver node receives information by observing the signal induced in the receiver coil. This inductive coupling-based method can be implemented in a smaller volume than a modulated signal-based transmitter, and can achieve low energy per bit.

N. Miura et al. propose the inductive coupling based communication method for a wireless bus for vertically stacked chips [21] with a 0.35 μm CMOS technology. They achieve the maximum data rate of 1.25 Gb/s/channel with the power consumption of 43 mW which means the achieved energy per bit is 32.0 pJ/b. They also report that the energy per bit is reduced to 1 pJ/b with the 65nm CMOS technology [26]. Based on the findings on the coil design for the inductive coupling reported by N. Miura et al. [27], S. Lee et al. propose inductive coupling-based transceiver which achieves 0.475 pJ/b of energy per bit by optimization of symbol transmission time [23, 24].

The inductive coupling based communication method is mainly targeting for short distance chip-to-chip communication. In the context of the chip-to-chip wireless communication, the energy efficiency per bit is more important than communicable distance since the most of the chip-to-chip communication is done in the range of less than sev-

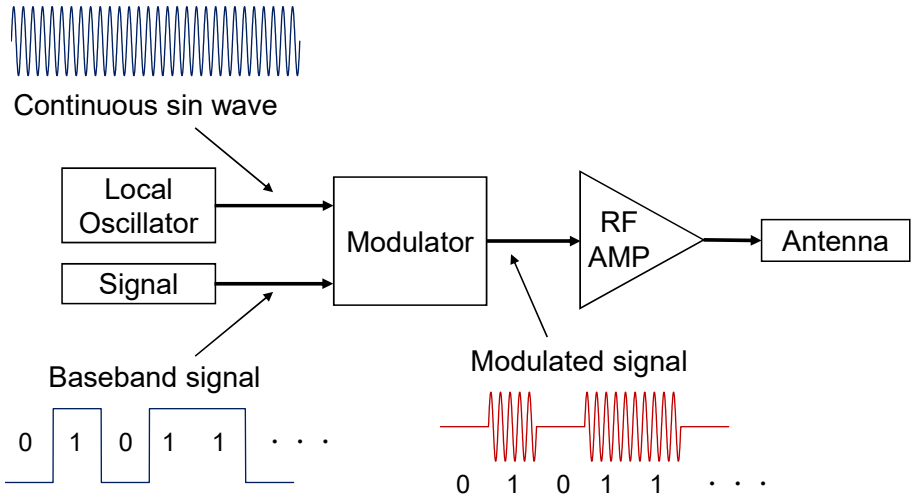

Figure 1.4: General transmitter structure utilizing carrier wave and modulation. As an example, the waveform in this figure is illustrated based on ASK-OOK-modulation.

eral cm. Hence, the communication range is set to at most several cm [22–24] and somtetimes set to even smaller than 1 mm [25] to achieve higher energy efficiency per bit. On the other hand, as for pervasive sensing, the communicable distance of several meters is more important than extremely efficient energy per bit. This is because the sensor nodes for pervasive sensing are scattered everywhere in our living environment, and therefore other sensor nodes, which can act as repeaters, are not necessarily installed near one sensor node. The inductive coupling based communication method also suffers from the misalignment problem. To keep communication quality at a sufficient level, the coil in each of the inductive coupling transmitter and receiver should face each other, which results in the reduced degree of freedom in the installation location and posture of sensor nodes.

Carrier wave-based communication

In terms of the robustness of the wireless communication, the carrier wave-based communication is more applicable for pervasive sensing. Fig. 1.4 shows the general transmitter for carrier wave-based communication. Fig. 1.4 indicates that this type of transmitter has to be equipped with not only the modulator to generate the RF-signal to be emitted but also the local oscillator (OSC) to generate the carrier wave. To ensure the communication quality at a certain level, the local OSC should be equipped with a frequency reference with high stability. As the frequency reference, following five types of frequency reference are often used for the small transmitter.

- Quartz crystal
- MEMS resonator
- Ring OSC

- Resistor-capacitor OSC (RC OSC)
- Inductor-capacitor OSC (LC OSC)

As the frequency reference, quartz crystal and MEMS based resonator show excellent characteristics in terms of the frequency stability. For example, the frequency stability of the quartz crystal is located around 10 ppm to 100 ppm [28], and hence the wireless transmitter for high-quality communication is often equipped with the quarts crystal as the frequency reference. When it comes to the small volume transmitter, CT-C. Nguyen points out that quartz crystal is a bottleneck in reducing the volume of transmitters like the inductor and the capacitor in the RF-front end circuit [29]. Therefore, structures that realizes high frequency stability with MEMS are being studied aggressively [29–32]. On the other hand, B. Wheeler et al. argue that utilizing a single CMOS process without additional processing such as MEMS is more preferable for mass production applications such as transmitters for pervasive sensing [33].

Transmitters without quartz crystal and MEMS resonator should be equipped with either of on-chip ring OSC, RC OSC, and LC OSC. Ring, RC, and LC based OSC are highly influenced by the surrounding environment (e.g. temperature) and therefore the frequency stability is not sufficient in its original circuit. The frequency stability of the ring OSC and RC OSC is more than 300 ppm/°C [34] and 250 ppm/°C [35], respectively while the frequency stability of the quartz crystal is less than 100 ppm as described above. However, X. Zhang et al. report that the frequency stability of the ring OSC can be improved to 85 ppm/°C by implementing the temperature compensation circuit [34]. Similarly, the frequency stability of RC OSC is also improved to several dozens of ppm/°C with the temperature compensation [35–37]. Moreover, O. Khan et al. report that RC OSC without the temperature compensation circuit can be calibrated to an accuracy of 70 ppm/°C or less by synchronizing the time with a circuit operating with a precise and accurate crystal quartz [38]. These findings enable us to utilize the ring and RC OSC as long as an appropriate compensation circuit for environment is installed. Although the frequency stability of ring and RC OSC is improved to several dozens of ppm/°C, the characteristic difference between those and crystal quartz is still large. Several studies have reported that LC OSC provides very high frequency stability compared to ring and RC OSC. Y. Wang et al. and E. O. Ates et al. report that the frequency stability of LC OSC can be improved to less than 1.7 ppm/°C with the help of temperature compensation [39, 40].

LC OSC's far higher frequency stability than ring and RC OSC strongly motivates us to adopt LC oscillations to the small sensor node for pervasive sensing. However, F. Zhang et al. point out that the LC OSC with small inductor with low quality-factor (Q-factor) consume larger energy compared to other methods [41]. To minimize the energy consumption per single communication bit, minimizing the operating time of LC OSC is important. There are two factors that prevent us from minimizing the operating time of LC OSC: the dead time and the time required for oscillation growth. Fig. 1.5 shows the circuit schematic of the Hartley oscillator, which is one of the well-known

LC OSCs, and two signals to be observed. Fig. 1.6 introduces the waveform of two signals $V1$ and $V2$ simulated with LTspice. Fig. 1.6 clearly indicates that the dead time, which denotes the time when no valid oscillation waveform is observed, is around 500 ns and the time required for growing oscillation is 1000 ns. The required start-up time, which denotes the sum of the dead time and the time required for growing oscillation, is more than 1500 ns in total. This long start-up time is a problem not only in terms of the energy consumption per bit but also the communication speed since the start-up time of 1500 ns limits the communication speed to 667 kbps. In pervasive sensing applications, many sensor nodes will share the same frequency band, and hence each communication should finish as fast as possible to ensure the valid communication system.

The start-up time of the LC OSC depends on the open-loop-gain of the amplifier and the Q-factor of the resonator as long as the input energy and the circuit structure are left unchanged [42]. Hence, some research focuses on shorting the start-up time by changing the circuit structure. Notably, J. Kim et al. shortened the start-up time by introducing the asymmetric structure for cross-coupled LC OSC circuit, which normally have a symmetric structure [43]. On the other hand, even the sophisticated circuit structure proposed by J. Kim et al. cannot make the start-up time zero and hence the time required for sending single bit still have room to be improved.

In addition to the OSC structure, the size of the antenna prevent us from miniaturizing the transmitter volume. Some research have successfully integrated almost all transmitter circuits into a single silicon-die. However, even those kind of transmitter chips cannot accommodate the antenna on a die. The size of the antenna required for the transmitter depends on the RF-signal frequency [44], and hence even the high frequency 2.4 GHz signal requires the antenna whose size is several cm. Currently, many transmitters devote some area or volume for dedicated antenna. A new structure is highly demanded that enables effective use of the limited volume.

1.3.2 Wireless power transfer

For over a century, research on wireless power transfer (WPT) system has been actively conducted after the first experiment of WPT conducted by N. Tesla [45]. Especially in recent decades, researches focusing on efficiency enhancement, robustness improvement, and application extension have been aggressively conducted and many findings are reported and accumulated [46–51]. Besides, application utilizing WPT technologies are already available on the market (e.g. chargers for smartphones, personal computers, and tablets), and widely used by people [46, 52].

WPT technologies are classified into five types according to the energy transmission mediums [49]:

- acoustic power transfer (APT) [53–59],
- optical power transfer (OPT) [60–62],
- microwave power transfer (MPT) [63–65],

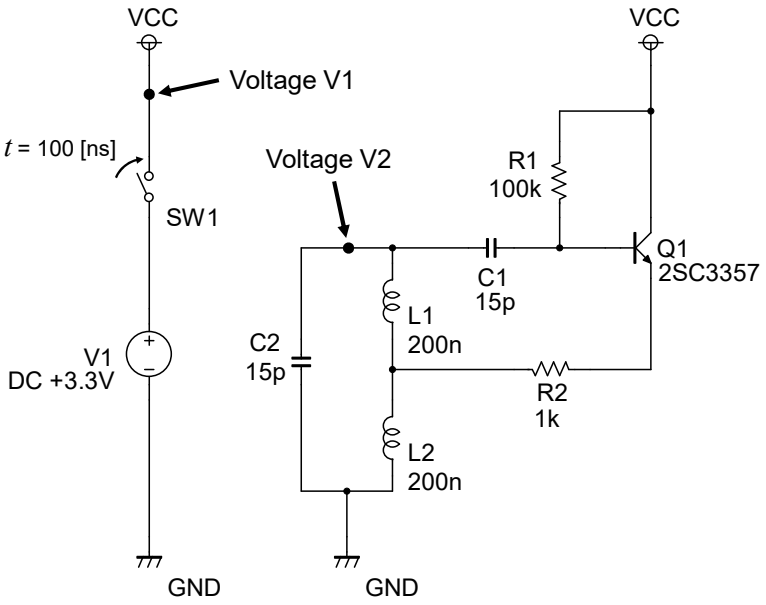

Figure 1.5: The schematic of the Hartley oscillator, one of the well-known LC OSCs.

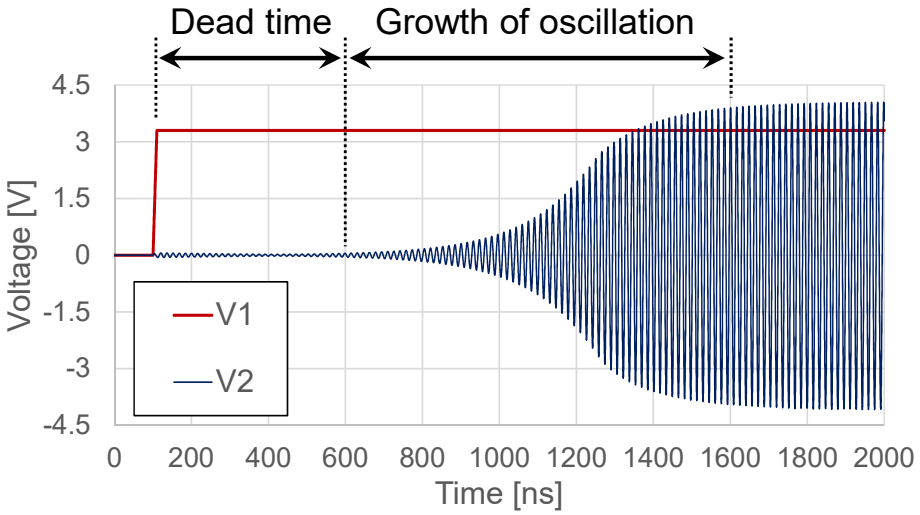

Figure 1.6: The waveform of signals defined in Fig. 1.5.

- capacitive power transfer (CPT) [49, 66],
- inductive power transfer (IPT) [51, 67].

To apply these WPT technologies to pervasive sensing in our daily life, following three factors are important in terms of practical use: robustness, safety, and transmission efficiency. Let me review each technology briefly from these perspectives. Research on APT based system is still in basic stage, however, its characteristic and specification are attracting attention. APT can achieve higher efficiencies compared to IPT, which

is currently the most promising technology and will be discussed later in detail, at the transmission distance of several times the diameter of transducer or coil [55, 57, 58]. In addition, acoustic wave, which is the transmission medium of the APT system, can propagate through not only air [56], but also water [57] and metal [59]. On the other hand, APT signal has higher beam directivity than the electromagnetic signal [55], and therefore APT systems suffer from the robustness problem. This directivity characteristic can contribute to higher efficiency in a specific situation where the system location is fixed, however, is not appropriate for most of WPT applications which require the flexibility on the installation location of the systems. Therefore, APT system is not applicable for applications to be utilized in our daily life. OPT systems can achieve high power conversion efficiency. S. D. Jarvis et al. report that the sophisticated electrical component can convert the optical energy to electricity with the efficiency of more than 40 %. However, OPT systems also suffer from the signal directivity problem in addition to the safety problem. Some research focuses on achieving the OPT indoor, while the system can turn on only at night or has to be shut down to avoid dangerous situation when humans approach the system [61, 62]. Hence, OPT is not applicable for our daily use in the current form. Similar to OPT systems, the microwave signal utilized in MPT also has the high directivity and safety issue. Research on MPT systems is actively conducted since it is applicable for two specific applications: the application that have to transfer energy at long distance with high directivity [63] and the application that handles only small amount of energy [65]. These application limitations originate from the characteristic of directivity and safety, and hence MPT will not be used for the daily applications.

CPT systems are applicable only for the WPT system which requires a short distance power transfer, such as several mm to cm, while the IPT systems can be applied to the both of millimeter-scale and meter-scale WPT [55, 66, 68]. Despite of the limitation on the transmission distance, research on CPT systems is actively conducted since CPT systems can handle larger amount of power than IPT, and is even applicable for kilowatt power level applications [66]. Compared to CPT, IPT handles less power than CPT since IPT systems suffer from the problem of eddy current-losses and copper-losses [49]. On the other hand, apart from the special application which requires only short distance power transfer, IPT system the most prevalent method in terms of safety [49] and practicability. Safety issue of both CPT and IPT is discussed in terms of living object detection (LOD) foreign object detection (FOD) [48].

LOD problem in CPT systems is much more important issue compared to FOD. CPT systems utilize electrodes to transfer power. Here, the capacitive coupling between transmitter and receiver is very weak [69], and hence not only the required frequency becomes higher but also the voltage applied to electrodes can be even kV level [49]. High voltage signals may cause electric shock to living object, which is an inherent problem for CPT systems. Besides, high frequency signals can possibly cause damage to human body [49] and hence LOD has to be implemented to CPT, while the LOD is

much more difficult than FOD. The foreign object in CPT system is also problematic but is not fatal since the foreign object will cause performance degradation, but not cause a safety problem.

IPT systems also have to be designed not to cause dangerous situations. Related to LOD concept, which is implemented not to hart living things, IPT has to utilize the signal which is safe for human body since some implantable system utilize IPT [70]. When the signal frequency is low enough, the signal is harmless to the human body while the higher frequency signal can cause damage to human body, where IEEE Standard C95.1-2005 provides safety standard [71]. When the system is implemented in a small volume, the coil size is also small and hence the resonance frequency is shifted to a higher frequency [72–74]. However, unlike the electric shock problem in CPT, this problem is avoidable by designing and tuning system correctly. On the other hand, unlike the CPT system tolerating the foreign metal, IPT system needs to monitor foreign metals with special attention since those can cause system damage or failure [75]. Qi standard [76] is a currently well-known WPT standard, and Qi version 1.1 allows system to transfer power to devices with the limit of 5W. Here, let me give an example, a power dissipation of only 0.5W to 1W in small metallic objects such as a coin and gold ring can heat up stuffs above temperature of 80°C [46]. To solve this issue of foreign object heating, many FOD methods for IPT system have been proposed [69, 77–79]. Therefore, as long as one of these FOD methods is implemented in the system, IPT can be a promising method of WPT for pervasive sensing in terms of its robustness and safety.

Several research on the power transmission efficiency of IPT systems has been conducted to derive theoretical limitation. A. Kurs et al. derive a formula which introduces the theoretical limitation of power transmission efficiency on 1-to-1 power transmission [68]. They report that the power transmission efficiency can be more than 90 % when the power receiver is placed near the transmitter, and can be around 40 % even when the distance between the receiver and the transmitter is set to eight times the diameter of the coil. The method proposed by A. Kurs makes each of transmitter and receiver be equipped with two coils respectively to enhance transmission distance while normal IPT system requires only one coil for each of transmitter and receiver in a minimal configuration. On the other hand, based on the theoretical circuit analysis, C.-J. Chen et al. and D.-W. Seo et al. revealed that installing more than one additional coil very close to transmitter and receiver is regarded as adding an impedance matching network, and concludes that only two coils in the system are directly involved in the long-distance power transmission through the magnetic field [80, 81]. Therefore, D.-W. Seo introduces another theoretical formula both for two-coil and multiple-coil based IPT focusing on utilizing multiple coils as repeaters of the power transmitter [82]. The theoretical analysis done by D.-W. Seo is only limited to 1-to-1 IPT system, while the power transmitter of pervasive sensing has to be responsible for numerous sensor nodes. For this reason, the knowledge on the analysis of 1-to-n wireless power transfer is highly

demanded. In addition to this, the requirements on the coil and circuit installed in the small sensor node are currently less discussed, and hence should be clarified.

1.3.3 Localization

To enable instant pervasive sensing technology to provide LBS, each sensor node should be localizable as described in Section 1.2. The most common position estimation method is a global positioning system-based (GPS-based) method, and its accuracy improvement is actively studied [83]. However, in the context of pervasive sensing, sensor nodes are not necessarily installed outdoor. Rather than that, sensor nodes should be scattered both indoor and outdoor for comprehensive information gathering. Therefore, the localization method for instant pervasive sensing should be applicable both for outdoor and indoor applications. The GPS signal severely attenuates indoors and cannot provide enough accuracy. Also, the localization error of the GPS-based method is in meter scale in many cases, and hence it is not capable of sensing subtle object movement. For these reasons, the indoor localization has much more difficulty compared to outdoor localization. Meanwhile, indoor localization methods, which can achieve cm-scale or even mm-scale error, can be applied to motion tracking. Such indoor localization can be applied to many applications such as table-top localization and indoor navigation, and therefore numerous methods have been reported and tested [84].

There are four popular ideas for indoor localization: proximity, fingerprint, camera and triangulation. Each idea utilizes different types of signal or information. The following first explains each idea briefly and then introduces several methods based on each idea.

Proximity based methods

The proximity based method estimates the sensor position using pre-installed multiple anchor nodes. Fig. 1.7 exemplifies the proximity based method. The sensor node detects the nearest anchor node and sets the position of the anchor node as sensor node's own position as shown in the right bottom table in Fig. 1.7. Here, the location of all the anchor nodes in the system must be known beforehand.

As a proximity method, M. Andries et al. develop load-sensing-floor that accurately estimates the positions of people and objects for the realization of ambient intelligence, where the load-sensing-floor is implemented with a large number of tiles consisting of multiple strain gauges [85]. In this method, the position estimation accuracy improves as the density of the anchor nodes is intensified. This work, on the other hand, suffers from installation cost and the difficulty in positioning small and light objects, and therefore it can be adopted only for some specific applications. As a proximity method that utilizes low-cost anchor node, RFID and the like which is small enough and can be installed anywhere are often used as the anchor node [86] since the position estimation accuracy highly depends on the density of anchor nodes and such small anchor nodes can be easily

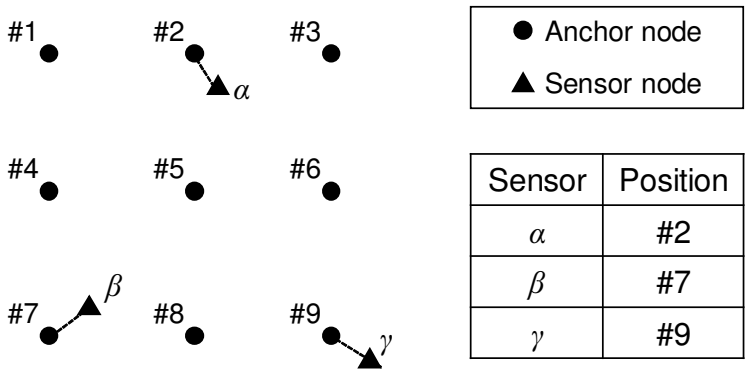

Sensor	Position
α	#2
β	#7
γ	#9

Figure 1.7: Proximity based localization method.

distributed densely. On the other hand, there is a disadvantage that the installation cost is relatively high because the number of anchor nodes is quite large and their locations must be measured beforehand.

Fingerprint based methods

The fingerprint based method estimates the position by finding the most similar data from the previously measured data with the data presently acquired by the sensor node. Here, *fingerprint* means each location has unique measurement data, and the pairs of position information and measurement data are stored in Look Up Table (LUT).

Wi-Fi signal is often used for fingerprint based method [87, 88]. Wi-Fi localization is advantageous in terms of installation cost since it does not require new equipment dedicated for position estimation. On the other hand, the fingerprint method suffers from the disadvantage that the preliminary measurement is necessary to build a LUT. In many Wi-Fi based position estimation methods, site survey needs to be performed to construct the LUT every time the indoor environment changes, which results in high operation cost. To avoid this problem, Wu et al. propose a Wi-Fi based localization method that makes site survey omittable by using the information collected by smartphones for LUT update [89]. Another concern of the Wi-Fi based localization method is the risk of privacy being violated by man-in-the-middle attacks via the Wi-Fi network [90].

Camera based method

The camera based method utilizes image processing techniques, e.g. Hough transform and machine learning, to estimate object positions. In camera based localization, depth cameras are often used in addition to RGB cameras. Figueiredo et al. propose an RGB-D camera based localization method that estimates the position of daily items using Random Sample Consensus (RANSAC) and Hough transform [91]. D. Murray et al. propose a motion tracking method based on the frame differences and achieved

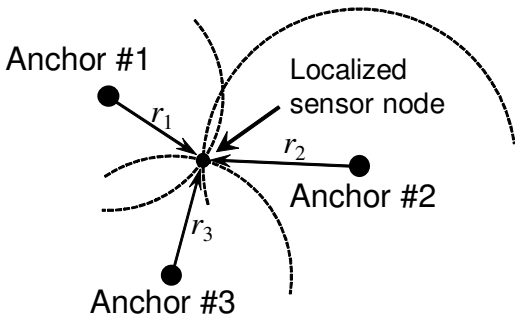

Figure 1.8: Lateration based localization.

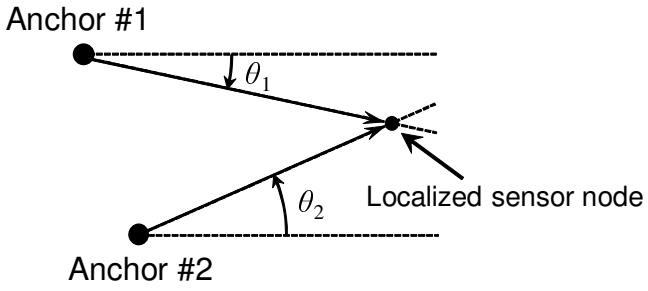

Figure 1.9: Angulation based localization.

high accuracy by compensating the camera pose. On the other hand, the camera-based method inherently involves an occlusion problem [92]. K. Kjarside et al. propose a marker-based motion tracking system that installs multiple cameras to avoid the occlusion problem [93]. However, the coverage area of this system is limited to a small space such as a dressing room, and it cannot be applied to a large space. Furthermore, the camera-based method has a privacy issue preventing dairy usage.

Triangulation based methods

Triangulation includes two methods: lateration and angulation. Fig. 1.8 illustrates lateration. The distance between the sensor node and the anchor node is obtained by, for example, time of flight (ToF) and received signal strength (RSS), and the position is identified with the distances to three anchor nodes. When there are more than three anchor nodes, redundant distance information can be used to mitigate the effect of measured distance error on the localization accuracy. Note that the anchor nodes are supposed to be accurately localized beforehand.

As a signal for distance estimation, magnetic field is often used [94–96]. W. Kim et al. theoretically demonstrate that we can estimate the position and posture of the sensor node with the AC magnetic signal [97]. Angelis et al. propose an AC magnetic

field based localization method which can localize the sensor position in the range of several meters from the anchor nodes [95]. J. Huang et al. have proposed a method to detect subtle movements of the fingertip with high accuracy using a large number of reference nodes in the distance of dozens of cm [98]. K.-Y. Chen et al. and E. Whitmire et al. implement motion tracking using a handy reference node achieving high degrees of freedom [99, 100]. There is an advantage that the coverage area is wide since AC magnetic field propagates farther than DC one. However, the AC magnetic field-based methods share the problem that the AC magnetic signal is significantly affected by not only ferrous materials but also non-ferrous metallic materials [95], although those materials are included in many of our everyday objects. Eq. (1.1) is the Maxwell-Faraday equation.

$$\mathrm{rot}\,\mathbf{E} + \frac{\partial \mathbf{B}}{\partial t} = 0, \tag{1.1}$$

where $\mathbf{E}$ and $\mathbf{B}$ are electric and magnetic fields, respectively. Eq. (1.1) indicates that when a conductive material is placed in an AC magnetic field, an eddy current flows inside the conductor. The eddy current generates a new AC magnetic field that interferes with the original AC magnetic field generated by the reference node. F. S. Parizi et al. and E. Whitmire et al, both of which propose AC magnetic field-based motion tracking methods, evaluate the impact of this weakness [101, 102]. The experiments performed by F. S. Parizi et al. and E. Whitmire et al revealed that non-ferrous metallic objects used in daily life, e.g., smartphones and personal computers, need to be placed at least 10 cm to 20 cm away from the system. Thus, the AC magnetic field-based approaches work correctly only in a specific environment where the metallic object is not positioned nearby. To overcome this problems, J. Blankenbach et al. propose DC magnetic field-based room-scale localization methods [96, 103]. P. H. Chen et al. propose a method that can extend the coverage area by placing new self-localizable reference nodes for tabletop applications [104]. All of these methods need multiple reference nodes for the localization. On the other hand, the multiple reference nodes-based methods are not suitable for our objective in terms of the installation cost. Therefore, the method which can localize sensor nodes with a single anchor node is eagerly demanded. As for the coverage area, the DC magnetic field-based system covers a narrower area than the AC magnetic field-based system. This problem on the coverage area comes from the signal propagation characteristic and the signal to noise ratio (SNR) [94]. While the signal voltage in the AC magnetic field-based system can be boosted by utilizing a higher frequency signal, DC magnetic field-based signal cannot be amplified without the active amplifier, which degrades SNR substantially. To overcome this coverage area problem, DC magnetic field-based methods have to give larger power to the reference coil compared to the AC magnetic field-based methods. Therefore the power consumption of the DC magnetic field-based method tends to be larger than that of the AC magnetic field-based method. For this reason, the DC magnetic field-based method is not suitable for the environment where a power outlet is not available. On the other hand, the

objective of this work is to provide the indoor meter-scale tracking infrastructure, and the reference coil can be supposed to be powered from the power outlet. Therefore, this relatively larger energy consumption is not a crucial issue.

Next, angulation is explained with Fig. 1.9. Angulation utilizes anchor-to-node relative angle information to localize the node whereas lateration utilizes node-to-anchor distance information. Angulation has an advantage that two anchor nodes are sufficient for positioning. As described above, the minimum number of anchor nodes required for lateration-based localization is three, and hence the angulation-based localization can reduce anchor nodes and the installation cost compared to lateration-based method. To further reduce the number of anchor nodes, S. Song et al. propose a hybrid method combining lateration and angulation, in which AC magnetic field is used for position estimation [105]. This hybrid method can estimate the sensor position with a single anchor coil by using the relative angle of the sensor viewed from the anchor in addition to the anchor-node distance information. The single anchor node brings the advantage of low installation cost and require no anchor localization. However, this method cannot be used in the environment including metallic objects since AC magnetic field cannot penetrate metal [95]. At the same time, this method is not suitable for small sensor nodes since each sensor node requires a complex structure coil.

1.3.4 Ambient intelligence based on motion tracking

Sections 1.3.1, 1.3.2, and 1.3.3, introduced conventional research on element technologies required for actualizing instant pervasive sensing. This section, on the other hand, reviews the conventional research on motion tracking-based AmI to show the potential applications of sensor nodes equipped with the three element technologies described above. The motion information of the sensor node is highly related to the position information of the sensor node. In terms of AmI, gathering even only motion information can greatly enhance our QoL, and hence, this section introduces how the motion information contributes to AmI and describes the existing problem on utilizing motion tracking information for AmI.

AmI utilizes not only "things" targeted by the IoT, but also information such as human positions and behavior. People output information during the conversation, working, and even when sleeping. Information emitted by a person includes not only verbal one but also non-verbal one such as body movement, the direction in which the person is facing, and the number of nodding actions during meetings, etc. Many researchers in both psychology and engineering fields have worked aiming at making conversations and meetings more effective and improving work environments with the assistance of information unconsciously emitted by people (e.g. [106–110]).

Especially, utilizing the position and behavior of a person as non-verbal information has been actively studied. T. Kim et al. try to improve the interaction within a group by utilizing the information of, for example, the people's movements during a meeting

and the distance and positional relationship between participants [111]. K. Fujita et al. sense the hand and head movements and the number of utterances for estimating the participants' activities in a standing party [112, 113]. These studies report that the participants retain their activity at a high level when the estimated activity is fed back to them through a display installed on the wall and floor.

Collecting information via wearable sensors is also actively studied, aiming to realize ambient intelligence. K. Ara et al. collect behaviors and interactions of people in an organization with wearable sensors to realize and utilize the concept of "business microscope [107]." K. Ara et al. aim to enable organizations and people to work more efficiently in the future by understanding human behavior and make use of knowledge and information.

All research mentioned above attempts to create a society that utilizes AmI by sensing the positions and movements of objects and people in our living environment. These studies illustrate the effectiveness from different aspects of AmI, and therefore taking advantage of all aspects of ambient intelligence should improve our QoL.

1.4 Issues and challenges

As described in Section 1.2, performance of three technologies should be improved: wireless communication, WPT, and localization. First, this section summarizes current issues of conventional work on these three technologies and clarifies the challenge for enabling instant pervasive sensing. Also, as described in Section 1.3.4, AmI can greatly enhance our QoL with the motion information of the objects and persons. Therefore, the later of this section points out the current issues that prevent us from showing the practicability of the motion tracking-based AmI.

In wireless communication, major challenge is to reduce both the sensor volume and the energy consumption at the same time. As described in Section 1.3.1, the sensor node for the instant pervasive sensing should be equipped with the carrier wave-based wireless communication function to achieve the communication range of several meters. On the other hand, currently available wireless transmitter requires several cm^3 volume for implementation while the transmitter circuit it self is implemented in mm^3-class volume. The main factor determining the volume of the transmitter is the dedicated antenna for the radiation. The size of the antenna is determined according to the wavelength, and hence the transmitter cannot be smaller as long as it apply the dedicated antenna. Hence, the dedicated antenna-free transmitter structure is highly demanded. In addition, the carrier wave-based transmitter requires a LC OSC-based frequency reference, which takes a long time for the signal output to be stabilized. A method for minimizing the time required for oscillation stabilization must also be developed since the transmitter wastes energy until the signal output stabilizes.

As for WPT, major challenge is to establish the analytical theory of 1-to-n WPT system and shows the feasibility based on it. Currently available WPT systems mainly

focus on 1-to-1 WPT, and the 1-to-n system is less discussed. Unlike in the 1-to-1 WPT system, the power transmitter is responsible for numerous number of receiver nodes in 1-to-n WPT system, and hence the transmission efficiency should be evaluated based on the total received power by receiver nodes. However, the analysis and formula on this 1-to-n WPT system is not discussed so far in detail, and hence the feasibility is not confirmed yet. For this reason, the analysis and theory establishment for 1-to-n WPT system is required. Also, the receiver circuit structure in the 1-to-n WPT system should be discussed and proposed.

Localization is also the important technology required for instant pervasive sensing. Conventional localization methods do not tolerate either occlusion situation or daily non-ferrous metallic material or both. In addition, currently available localization techniques require multiple anchor nodes and hence the installation cost is high. Furthermore, some methods require complex structure for sensor node and cannot achieve the sensor volume suitable for pervasive sensing. For these reasons, the localization method which can solve these three remaining problems, the robustness, the installation cost, and the sensor volume problem, should be provided.

As for motion tracking-based AmI, major challenge is to establish the instant motion tracking method which is not specialized for only one application. Each system described in Section 1.3.4 requires the installation of dedicated equipment and the environment for a specific purpose. Generally, this equipment and environment cannot be diverted to other systems. Therefore, the currently available researches cost significantly to introduce the equipment and environment for ambient intelligence. Hence, the system which can instantly enable us to track object and persons with low installation cost should be provided.

1.5 Objective and Organization

The overall objective of this dissertation is to develop the high-performance sensor node required for actualizing instant pervasive sensing. To achieve this objective, this dissertation addresses and solves four problems described in the previous sections: the wireless communication, the WPT, the localization, and the motion-tracking based AmI. The following will introduce the contribution of each chapter in this dissertation. Fig. 1.10 shows the relationship among Chapters 2, 3, 4, and 5, and the contributions of each chapter. To actualize the sensor node for instant pervasive sensing, basic three components should be realized and embedded into the sensor node:

- meter scale wireless communication,
- meter scale 1-to-n WPT,
- meter scale localization with the error of several cm.

These three components will be actualized and evaluated in Chapters. 2, 3, and 4. Fig. 1.10 shows that application-specific components must be installed on the sensor in order for the instant pervasive sensor to meet requirements of the given application. On

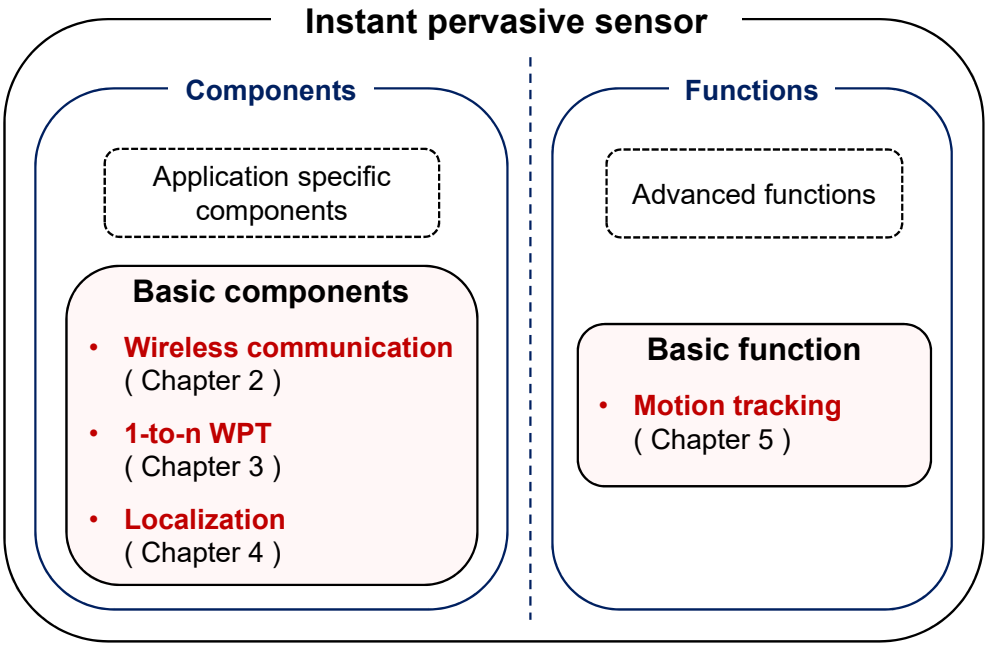

Figure 1.10: Relationship among Chapters 2, 3, 4, and 5, and contribution of each chapter.

the other hand, the sensor node only with the three basic components discussed above can provide motion tracking as a basic function. As explained in the previous section, motion tracking should make a significant contribution to AmI. Therefore, to show the effectiveness of the instant pervasive sensor proposed in this dissertation, Chapter 5 evaluates the feasibility of motion tracking with basic components and its contribution to AmI.

The first contribution in Chapter 2 is to propose a compact VHF-band OOK transmitter. There are two difficulties on actualizing transmitter for the instant pervasive sensing: the volume reduction of the dedicated antenna for smaller volume and the start-up time reduction of the LC OSC for higher communication speed. To solve the first issue of the volume reduction, the proposed transmitter uses coils for radiation as well as oscillation, eliminating the need for an external antenna. This feature contributes to fewer number of components, smaller volume and and lower cost. This work prototyped the transmitter with 2.8 mm $\times$ 2.8 mm $\times$ 4.2 mm volume. For shortening the start-up time and enabling high-speed communication, this work devises a scheme that provides a weak current for quick start of LC oscillation. Measurement results show that the dead time of LC oscillation is reduced from 400 ns to 40 ns, and 1m communication at 3Mbps is possible. The minimum energy consumption per bit of the proposed transmitter is 205 pJ/b with the bare baseband signal, and is improved to 51.8 pJ/b with the proposed energy efficient baseband encoding.

The second contribution in Chapter 3 is to show the theoretical analysis on the 1-to-n

WPT system and propose the appropriate power receiver design. Three primary difficulties on this topic are to analyze the 1-to-n WPT system theoretically unlike conventional work focusing only on 1-to-1 WPT, to confirm the feasibility of the 1-to-n WPT system based on the analysis, and to establish the appropriate WPT receiver circuit structure for the wireless nodes for pervasive sensing. For first two challenges, this work derives theoretical formulas based on circuit analysis and the theory of magnetics and reveals that the power transmission efficiency can be more than several dozens of % as long as the circuit constants are appropriately tuned. As for WPT receiver circuit, this work proposes the structure that the circuit automatically enters the WPT mode in case of the energy depletion utilizing Junction Field Effect Transistor (JFET). In addition to these, this chapter also proposes the method to share the coil among the wireless communication and WPT mode to minimize the required volume for sensor node. Experimental results show that, in the WPT mode, the two coils are automatically connected to each other, and the node can receive power even if there is no energy left in the node. In the wireless communication mode, 1 kbps communication is possible at a distance of 10 cm.

The third contribution in Chapter 4 is to establish the indoor localization method with low installation cost. The main difficulty here is to achieve single anchor based localization which can tolerate daily stuffs including metallic objects. To solve this issue, this chapter proposes a DC magnetic field based robust indoor 3D localization method with a single anchor coil. The proposed method estimates the sensor position from both geomagnetism and artificially generated DC magnetic field and not affected by non-ferrous metallic objects. The proposed method does not require any pre-measurement or multi-anchor nodes in the minimal configuration, and hence it can realize instant 3D localization with lower installation cost. This work experimentally evaluated the proposed method supposing tabletop-scale and room-scale applications. For table-top scale applications, the proposed method estimates the 3D position with the maximum error of 6.5 mm in the range of 250 mm. For room-scale applications, which require coverage area expansion with multiple anchor coils, the proposed method localizes the sensor with the maximum error of 14.7 cm in 3.0 m $\times$ 1.5 m area.

The fourth contribution in Chapter 5 is to show the application and potential of this work with the prototyped tiny sensor nodes. The sensor nodes for AmI application should be equipped with not only three element technologies described above but also specific sensing technologies (e.g. light and vibration sensor for security, cardiac sensor for health, etc.). On the other hand, the potential application based on the minimal sensor node which adopts only several of new techniques developed in this dissertation is huge and can even solve the conventional problem. To show the practicability of the prototyped sensor node, Chapter 5 builds an indoor magnetic tracking system based on the developed techniques that enable us to track the movement and orientation of people and objects by only attaching tiny electronic trackers to them. The size of the prototyped tracker is only 25.4mm $\times$ 25.4mm $\times$ 10.0mm, and hence it can be readily

attached to almost anything and immediately activated. The experimental result shows that by sensing the motion of the persons and objects, the working contents and status of persons are successfully estimated.

The rest of this dissertation is organized as follows. Chapter 2 proposes the tiny wireless transmitter structure which does not require volume-consuming dedicated antenna. With the proposed structure and the energy efficient baseband encoding technique, low energy consumption per bit is achievable. Chapter 3 reveals the feasibility of the 1-to-n WPT system based on the theoretical analysis and proposes the WPT receiver circuit indispensable for maintenance free pervasive sensing node. Chapter 4 proposes the DC magnetic field based 3D localization method which utilizes only single anchor node, which greatly contributes to reducing installation cost of the system. The proposed method achieves high accuracy both in the room-scale application and the tabeltop-scale application. Chapter 5 proposes the tiny motion tracker based on the techniques developed in Chapter 4 and introduces that AmI can enhance our QoL only with motion information of sensor nodes. Lastly, concluding remarks are given in Chapter 6.

Chapter 2

Dedicated antenna-free energy efficient wireless transmitter

The tiny sensor node used for pervasive sensing should communicate with communication host wirelessly not to limit the installation location. Implementing the wireless transmitter to the sensor node is difficult in terms of the energy consumption of the transmitter since the capacity of the battery or energy tank in the tiny sensor node is significantly limited as expressed in Section 1.3.1. To address this issue, this chapter proposes a compact VHF-band OOK transmitter that uses coils for radiation as well as oscillation, eliminating the need for an external antenna. In addition to proposing the transmitter structure, this section introduces the energy efficient baseband encoding method to reduce the energy consumption per bit to less than 100 pJ/b even with the energy consuming carrier wave based communication.

2.1 Introduction

As described above, the main challenge to accommodate the wireless transmitter into the small sensor node is the energy consumption of the transmitter. Inductive coupling based wireless communication method can achieve high energy efficiency such as several pJ/bit, however, the problem of the communication range and the installation angle limitation prevent the inductive coupling based method from being adopted by the tiny sensor node for pervasive sensing. Rather, the carrier wave based communication method is actively studied since the communicable distance is much longer than the inductive coupling based method. The carrier wave based wireless transmitter can provide the communication range of several meter, which is suitable for most pervasive sensing applications. As for carrier wave based wireless transmitter, quartz-crystal based frequency reference are originally used. However, the quartz-crystal takes large part of the transmitter, and hence other frequency reference are tend to be adopted for tiny sensor node. As the frequency reference of the tiny transmitter, LC-OSC, which consists of

inductor (L) and capacitor (C), is a promising method since LC-OSC achieves higher frequency stability compared to other OSCs as described in Section 1.3.1. However, the currently available LC-OSC based transmitters have to be equipped with the dedicated external antenna which usually has a size of a several cm^3. Consequently, the size of the transmitter is determined by the size of dedicated antenna while the size of the transmitter circuit is further smaller than the antenna. To solve this issue, this chapter proposes a dedicated antenna free transmitter which can achieve 205 pJ/bit even with the non-encoded bare baseband signal. With the proposed energy efficient baseband encoding technique, the energy consumption per bit is further reduced to 51.8 pJ/bit.

The rest of this chapter is organized as follows. Section 2.2 proposes the transmitter structure that does not require the dedicated antenna which take a large part of the transmitter. Section 2.3 conducts the hardware evaluation of the proposed transmitter. Section 2.4 discusses the energy efficient baseband encoding method to minimize the energy consumption per bit. Finally, the conclusion of this chapter is given in Section 2.5.

2.2 Proposed transmitter structure and its implementation

Fig. 2.1 shows the schematic of the proposed transmitter. The transmitter is based on a collector-grounded type Hartley oscillator circuit that includes two coils for LC oscillation. In the proposed transmitter radiates electromagnetic waves from these two coils instead of an external dedicated antenna. Here, this work adopts the Hartley oscillator as an example of the simple LC oscillator whose required number of components is small. As long as the circuit structure allows us to control the amount of current injected to inductors easily, other kind of LC oscillator can be adopted. The following explain the basic operation of the Hartley oscillator. Q1 in the schematic is a VHF/UHF band transistor and is used as a current amplifier. When a signal is applied to the base of Q1, a current-amplified same-phase signal appears at the emitter. By injecting the current-amplified signal into the tap of the coil, it composes a positive feedback and starts to oscillate. Also, the signals other than the resonance frequency are attenuated by the tuning circuit consisting of L1, L2, and C2, and then the output of this circuit becomes a sine wave at the resonance frequency.

OOK is enabled by powering on or turning off the oscillator as depicted in Fig. 2.1. A short time later after the power on, the oscillation, i.e. “1” radiation starts. This duration between the power on and the oscillation start is a wasteful time for OOK and this dead time limits the maximum communication throughput since the symbol time cannot be smaller than the dead time. To improve the throughput, this dead time should be minimized. In addition, the dead time minimization is also helpful to reduce the energy since the signal transmission finishes in a shorter time. Besides, the prototype

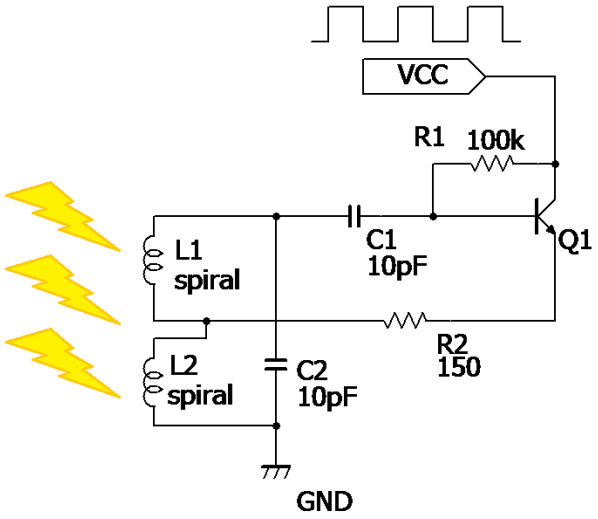

Figure 2.1: Proposed transmitter.

evaluation, which will be shown in the next section, shows that the dead time is 400 ns, which means the maximum throughput is limited to 2.5 Mbps.

This dead time depends on the inductance value of the coil. When the transmitter is powered on, the inductor generates counter electromotive force and then the coil cannot conduct current immediately after the power on. From another point of view, in the case that non-zero current is flowing in the coil beforehand, the generated counter electromotive force can be mitigated. Consequently, the current necessary for oscillation begins to flow earlier and the dead time becomes shorter. This non-zero current is provided by giving voltage V_{mid} as VCC during "0" transmission. Note that at V_{mid} the oscillator is not oscillating. This V_{mid} should be determined taking into account the trade-off between the dead time reduction and power consumption during "0" transmission.

Figs. 2.2 and 2.3 show the prototype of the proposed transmitter. 1.6 mm $\times$ 0.8 mm chip resistors and capacitors are used for the prototype. The size of the transistor Q1 is 1.6 mm $\times$ 1.6 mm. Fig. 2.4 shows a 3.6 mm-diameter four-turn spiral coil (for L1, L2), in which polyurethane copper wires of 0.15 mm are wound on both sides of a glass epoxy (FR-4) board. The inductance value estimated with network analyzer (Agilent Technologies, E5071C) is 100.13 nH.

Let us discuss the advantage and disadvantage of the proposed transmitter. The most significant advantage is that the proposed transmitter does not have a dedicated 50-Ω antenna and consequently the impedance matching circuitry is unnecessary. As a result, the transmitter can be composed of only five components except the coils, which is highly desirable for small volume implementation. In addition, the loss originating from impedance mismatch can be eliminated. On the other hand, there is a disadvantage. The primal disadvantage is the poor frequency stability, which is often a problem in LC oscillation circuits. Due to the poor frequency stability, each node needs wider

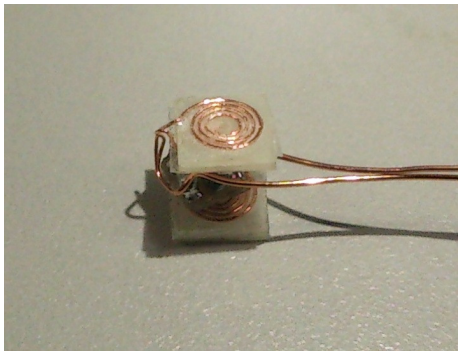

Figure 2.2: Prototype of proposed transmitter.

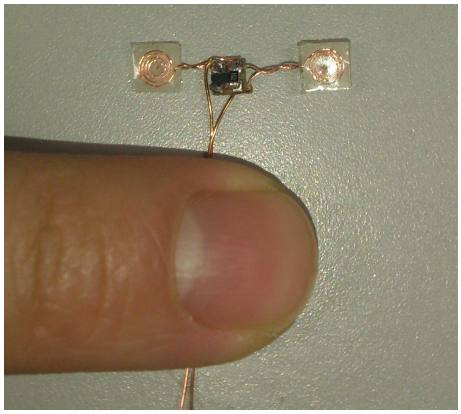

Figure 2.3: Expanded view of prototype.

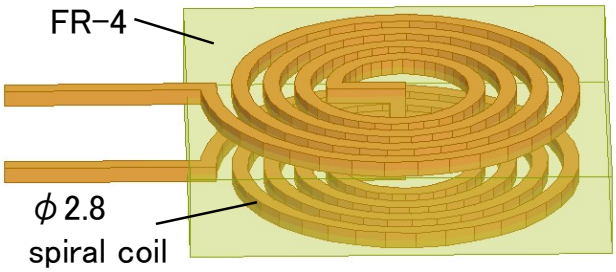

Figure 2.4: Spiral coil for tuning circuit.

frequency band for communication. This disadvantage is not a big issue in applications that many transmitter nodes share a single receiver that receives a wide range of frequency.

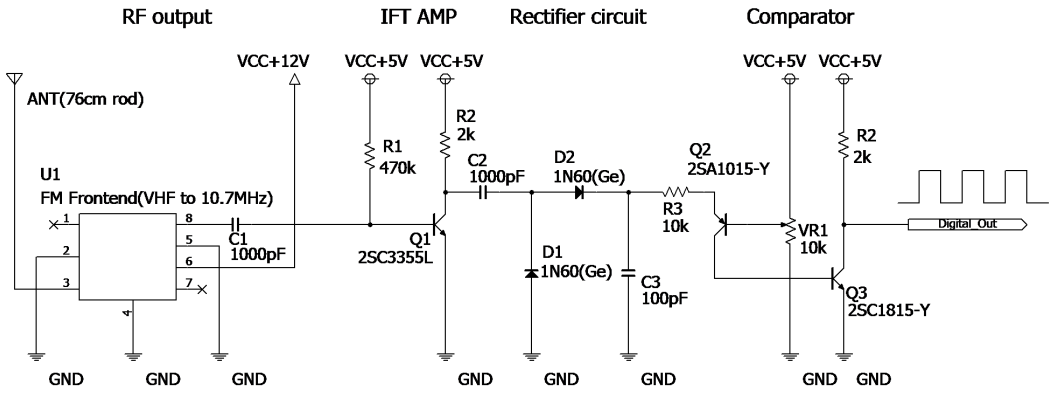

Figure 2.5: Schematic of receiver.

2.3 Evaluation

To confirm the effectiveness of the proposed transmitter, this section evaluates the performance of the transmitter. First, Section 2.3.1 introduces the circuit structure of the wireless receiver utilized for evaluation. Then Sections 2.3.2 and 2.3.3 explain the power consumption and baud rate of the proposed transmitter, respectively.

2.3.1 Receiver structure

The transmission power of the transmitter is weak and then we need to perform sufficient amplification on the receiving side. To facilitate the receiver design by minimizing the portion of the high frequency circuit, this work adopted a super heterodyne circuit as a receiver. An intermediate frequency of 10.7 MHz is generated by frequency conversion, and this intermediate frequency is amplified and processed. Here, to save the design time, a commercial FM frontend manufactured by Mitsumi is used for frequency conversion. The intermediate frequency is 10.7 MHz, and hence the maximum communication speed with this receiver is limited to several Mbps. Fig. 2.5 shows the schematic of the implemented receiver, and Fig. 2.6 shows a photo of the receiver. For the antenna of the receiver, a 76 cm rod antenna was used.

2.3.2 Power consumption

Fig. 2.7 shows the signal observed at the emitter of transistor Q1 with an oscilloscope when VCC is 3V. The proposed transmitter oscillated at 108MHz with 3.34 V magnitude, as designed.

Fig. 2.8 shows the current consumption of the transmitter when the power supply voltage is varied from 0.6 V to 3 V. The red vertical line in the figure corresponds to 0.66 V, which is the minimum voltage required to start oscillation. The proposed transmitter

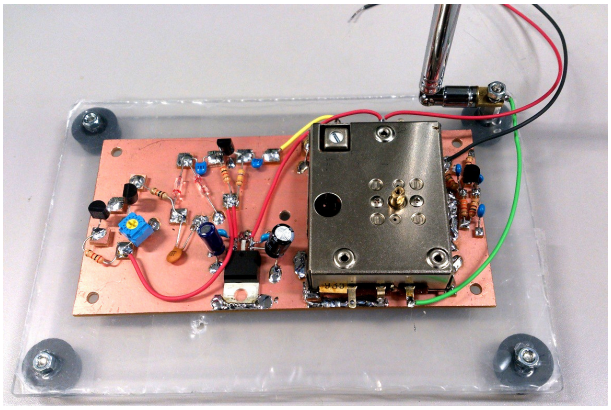

Figure 2.6: Photo of receiver.

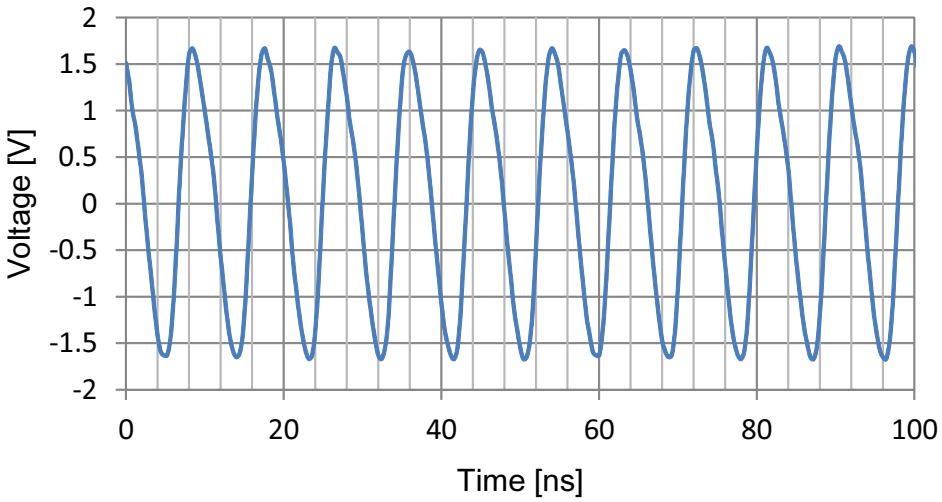

Figure 2.7: The signal appears at the emitter.

can operate at a wide range of supply voltage. Fig. 2.8 also shows that the current rapidly increases when the power supply voltage exceeds 0.65 V, where 0.65 V is the base-emitter saturation voltage of Q1. Beyond 0.7V, the current is proportional to the power supply voltage, which is due to the following reason. Transistor Q1 operates in forward active mode. In this case, the collector current is kept constant even with the collector potential variation as long as the base current is constant. On the other hand, the circuit in Fig. 2.1 is a fixed bias type circuit. The base current is proportional to the collector potential and the collector current is proportional to the base current. Therefore, the collector current becomes proportional to the collector potential, i.e. VCC.

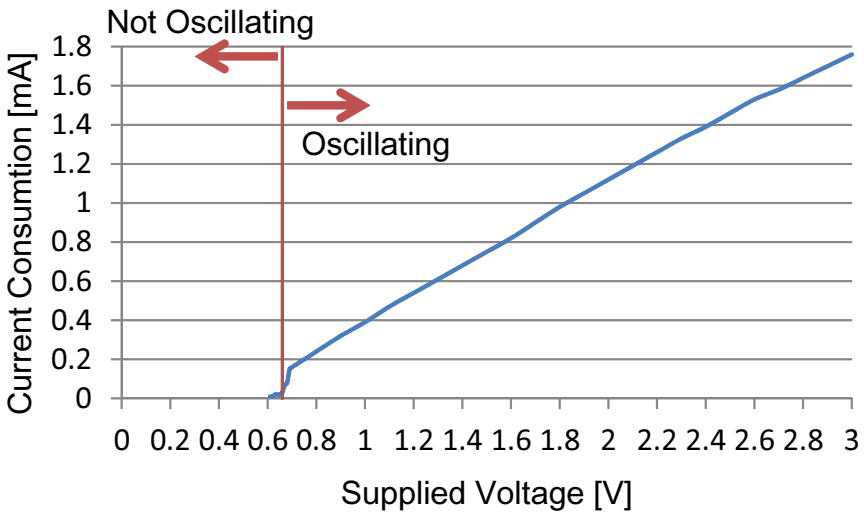

Figure 2.8: Current consumption versus supply voltage.

2.3.3 Baud rate

Fig. 2.9 shows the power supply voltage (red line) and the signal waveform at the emitter of Q1 (blue line) when the power supply voltage VCC is changed from 0 V to 3 V. When powering on the transmitter, the oscillation starts after a certain amount of dead time. In this case, 400 ns dead time is necessary. As discussed in Section 1.3.1., this dead time limits the throughput and hence Section 2.2 introduced V_{mid} for reducing the dead time. According to Fig. 2.8, V_{mid} is set to 0.65 V, where it is the maximum voltage that cannot start the oscillation, since the current at 0.65 V is 0.02 mA and it is negligible compared to the current during "1".

Fig. 2.10 shows the signal at the emitter when the power supply voltage is raised from V_{mid} = 0.65 V to 3 V. The dead time is reduced to 40 ns, which is 1 / 10 or less compared to 0 V to 3 V transition. This shorter dead time can contributes to the throughput improvement. Fig. 2.11 shows that 20 Mbps transmission is feasible at 3 V operation thanks to the shortened dead time.

Finally, the communication speed including both the transmitter and receiver was evaluated by observing the output of the FM front end circuit in Fig. 2.5 with an oscilloscope. A rectangular wave with 50% duty ratio was given from a function generator to the proposed transmitter as VCC and the maximum frequency at which the waveform could be reproduced on the oscilloscope was evaluated. Three supply voltages of 1, 2 and 3V and two distances of 1 m and 5m between the transmitter and receiver were tested. Results are listed in Table 2.1. This table also includes energy per bit under each condition. For 5 m communication, the supply voltages of 2 and 3V achieved 200 and 600 kbps throughputs. The output waveform of the FM front end in the receiver

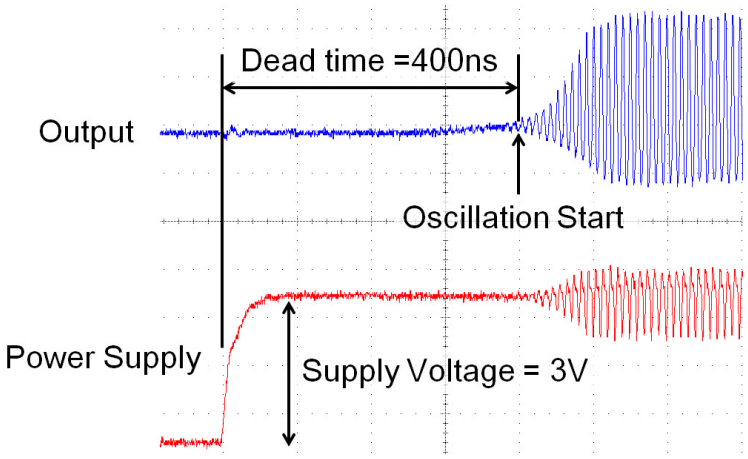

Figure 2.9: Dead-time at the start of oscillation.

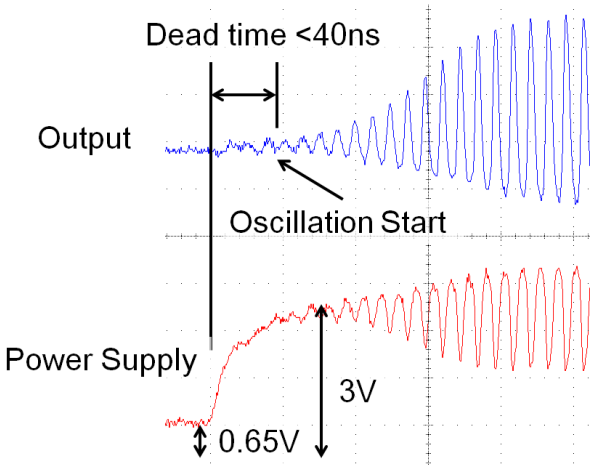

Figure 2.10: Shortened dead time.

is shown in Fig. 2.12. We can see the transmitted waveform of 600 kbps is well reproduced. As for 1 m, the supply voltages of 1 V achieved 1.0Mbps, and of 2, and 3V achieved 3.0 Mbps throughputs. The lowest energy per bit of 205 pJ/bit was attained at 1 V. Fig. 2.13 shows the waveform at the receiver when a 500 kHz, i.e, 1 Mbps signal was transmitted by the transmitter operating at 1 V with 1 m distance. We can see the intermediate frequency of 10 MHz is amplitude-modulated at 500kHz. In this case, the power consumption per bit is 205 pJ / bit. It should be noted that the throughput in each condition depends on the receiver performance and, with a more sophisticated receiver, the energy per bit could be further reduced, which is one of the future works.

The measurement results of the proposed structure are summarized in Table 2.2. Table 2.2 also shows comparisons with related studies on small transmitters. We can see

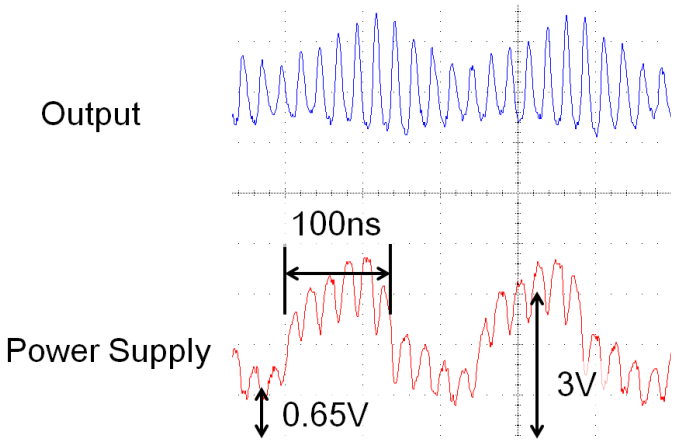

Figure 2.11: Transmitter output for 3 V, 20 Mbps communication.

Table 2.1: Transmission range vs communication speed.

	Communication Speed[Mbps] (Energy per bit)		
Range [m]	1V	2V	3V
1	1.0 (205pJ/b)	3.0 (380pJ/b)	3.0 (890pJ/b)
5	0.8 (256pJ/b)	1.4 (814pJ/b)	1.4 (1910pJ/b)

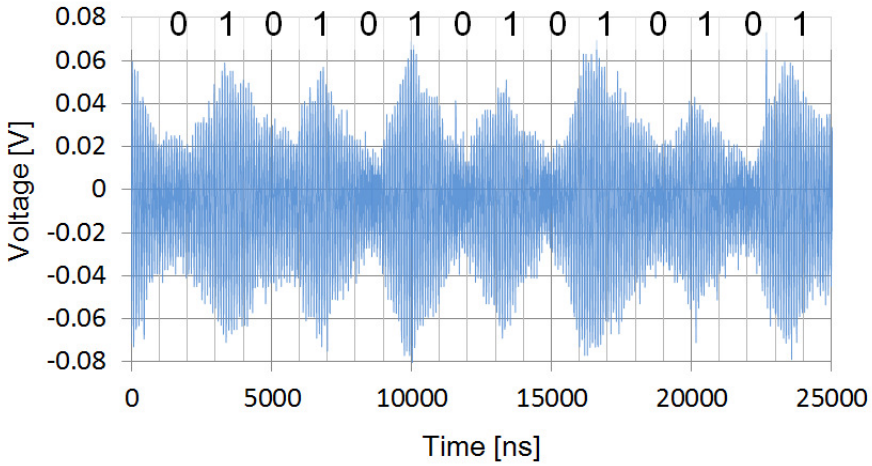

Figure 2.12: Received signal from transmitter, 5 m away from receiver.

that the proposed transmitter achieved better throughput and energy per bit than [114] and comparable performance to [115, 116] without any dedicated external antenna. This result indicates that the coils used for LC oscillation can be also utilized for electromagnetic wave radiation. The proposed transmitter needs no impedance matching and hence it is suitable for smaller volume implementation.

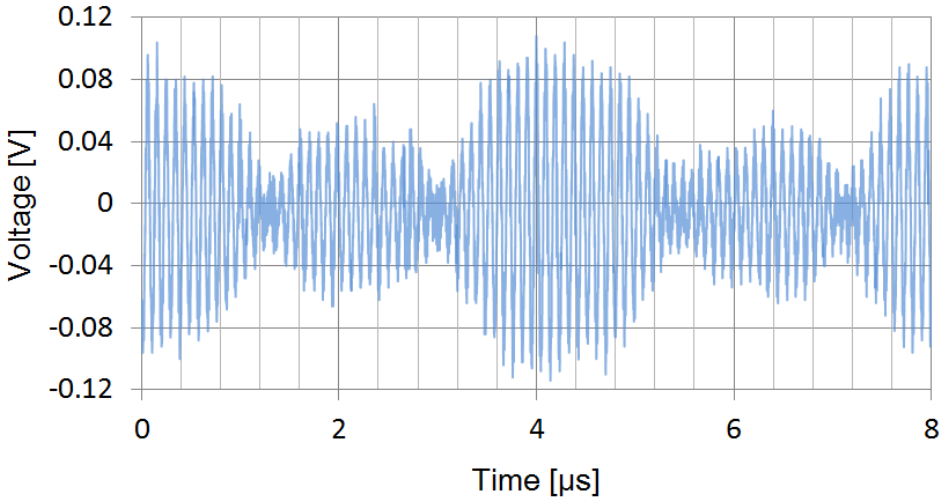

Figure 2.13: 1Mbps communication.

Table 2.2: Comparison with related work.

	[114]	[115]	[116]	This Work (1V)	This Work (2V)
Implementation	CMOS 130nm	CMOS 180nm	CMOS 130nm	discrete components	
Antenna	ext	ext	ext	int	
VDD [V]	1.5	0.7	1.2	1.0	2.0
Power (mW)	2.7	0.7	1.68	0.39	2.24
Modulation	2FSK	2FSK	2FSK	OOK	
Data rate	48kbps	5Mbps	4Mbps	1Mbps	3Mbps
Energy/bit(nJ/b)	56.25	0.14	0.42	0.205	0.38

2.4 Discussion on baseband encoding

The transmitter usually transmits the baseband signal encoded as packets to facilitate the data processing at the receiving side. Here, there are two packet encoding schemes; fixed-length packet and variable-length packet as shown in Fig. 2.14. The proposed transmitter consumes energy only when transmitting symbol “1”, and therefore energy per bit can be reduced by decreasing the number of symbols “1” contained in the encoded packet. The following discusses which packet scheme is more advantageous regarding communication speed and energy per bit.

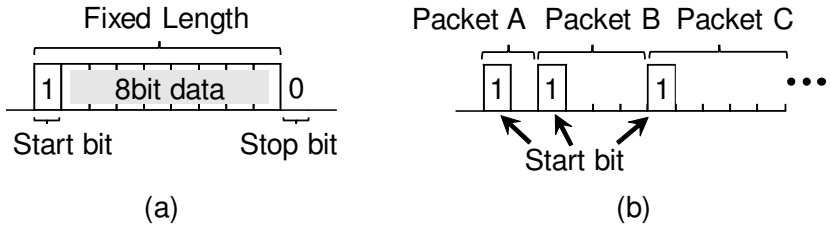

Figure 2.14: (a) Fixed-length packet and (b) variable-length packet.

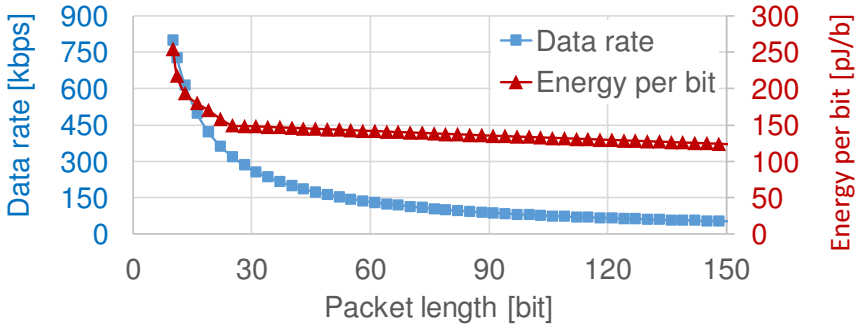

Figure 2.15: Performance of fixed-length packet.

2.4.1 Fixed-length packet

The fixed-length packet consists of a start bit, a stop bit and a data part. Fig. 2.14(a) shows an example of a fixed-length packet whose data part length is 8 bits. Here, we suppose that each packet includes 8-bit data. In this case, the minimum packet length is 10 bits. On the other hand, when we increase the packet length while keeping the data itself unchanged, we can use $n(n \geq 9)$ bits for expressing 8-bit data. In this case, we can map each 8-bit data representation to one of n-bit representations aiming to reduce the number of symbols "1" in the packet, which is expected to reduce the energy per bit.

To evaluate the minimum energy per bit of fixed-length packet, this section conducts simulation experiments on the premise that 256 8-bit data which express number 0 to 255 was communicated at a distance of 1 m. Then, the total data to be transmitted was $8[\text{bit}] \times 256 = 2048[\text{bit}]$. The maximum voltage applied to the transmitter was 1 V. Fig. 2.15 shows the data rate and the minimum energy per bit when the packet length including the start and stop bit is varied from 10 bits to 150 bits. Note that, among all the mapping combinations, the results achieving the minimum energy per bit are presented. Fig. 2.15 indicates that, when the packet size is small, the energy per bit can be greatly improved with a slight increase in the number of bits. On the other hand, beyond that, the reduction of the energy per bit gets smaller while it steadily degrades the data rate.

2.4.2 Variable-length packet

When we use the variable-length packet scheme illustrated in Fig. 2.14(b), the packet length varies depending on the data to be transmitted. Let us suppose the variable-length packet consists of a start bit and variable-length data part. In this variable-length packet scheme, the lowest energy per bit is attained in the case that the transmitter transmits only the start bits and the data itself is represented as the time intervals between the start bits. The transmitter informs the receiver of the end of communication by transmitting the symbol "1" as a stop bit. At the receiver side, when the symbol "1" does not appear in a certain period, the last received symbol "1" is recognized as a stop bit. This section proposes a baseband encoding in which the time interval between the start bits, i.e., successive "0" duration in the packet represents the original data. When the original data to be transmitted is m, the length of the data part is set to m clk, where clk represents a symbol time.

With this variable-length coding, the coding unit (CU) plays an important role, i.e., it determines the number of packets to be transmitted, data rate and energy per bit, where CU is the number of bits of the original data that is included in a single packet. Fig. 2.16 illustrates the code generation of the proposed encoding. Fig. 2.16(a) exemplifies a case when CU is set to 2 bits. In this case, the original 8-bit data is divided into four parts, and each part composes a packet. The four 2-bit data are "10," "11," "01," and "01," which means the numbers of symbols "0" are set to 2, 3, 1 and 1, respectively. From the above, the total time of the symbol "1", which consumes energy, is 4 clk and the time required to transmit the overall 8-bit data is 11 clk. Fig 2.16(b) shows a case when CU is set to 4 bit. In this case, the transmitting time of the symbol "1" is only 2 clk, and the energy consumption is halved compared with the case of (a). However, the time necessary to transmit the overall 8-bit data increases to 18 clk since the maximum number of successive symbols "0" becomes 15. Thus, CU affects the number of packets, the communication time, and the energy necessary to transmit the original 8-bit data, and then the data rate and energy per bit are in a trade-off relationship. Namely, when CU is large, the energy per bit improves while the data rate degrades. When CU is small, vice versa.

This section conducts simulation experiments on the variable-length packet encoding. Fig. 2.17 shows the relationship between the energy per bit and data rate when CU is varied from 2 to 8. From Fig. 2.17, we can say that increasing CU greatly degrades the data rate, but the energy per bit can be drastically reduced. The comparison between Fig. 2.15 and 2.17 indicates that the variable-length packet scheme is superior in terms of energy per bit when the transmitter communicates at the same data rate. For applications that do not require a high-speed communication, the proposed transmitter can reduce the energy consumption per bit to up to 51.8 pJ/b.

Finally, Fig. 2.18 shows a comparison with related works in literature. We can see that the transmitter with the proposed baseband encoding of CU=4 and 8 achieves smaller energy per bit than the system proposed in [115].

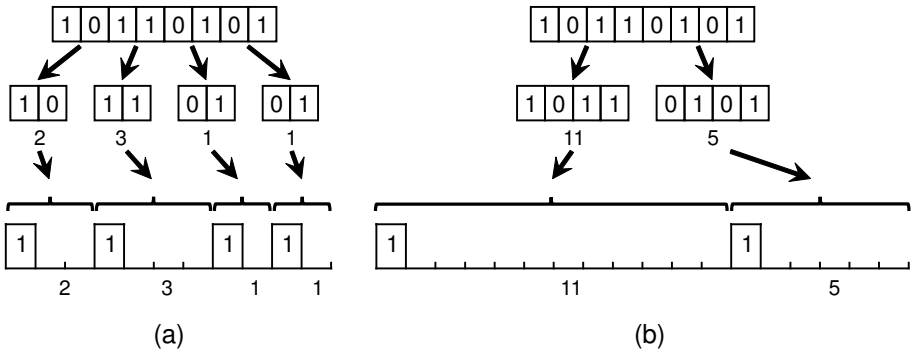

Figure 2.16: Baseband encoding to generate variable-length packets. (a) when the coding unit is 2 bits (b) when the coding unit is 4 bits.

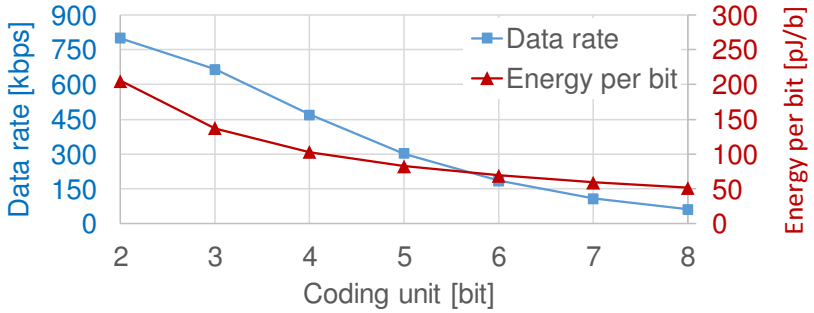

Figure 2.17: Performance of variable-length packet.

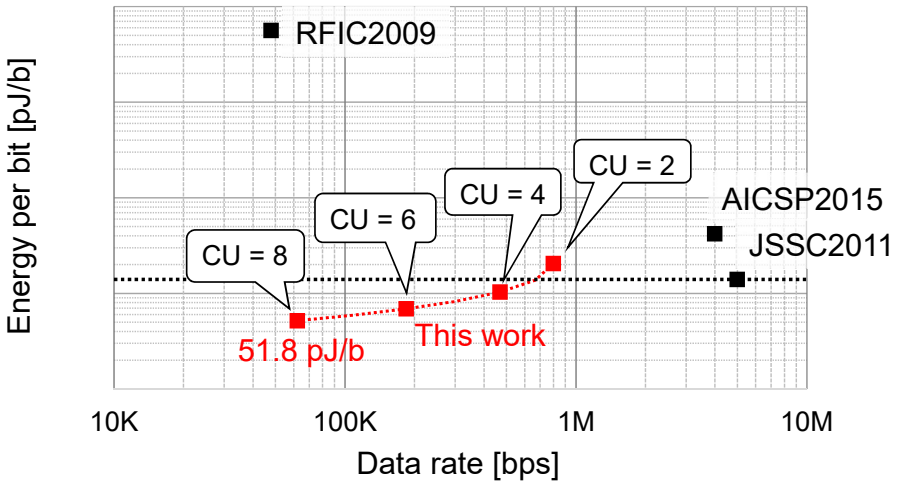

Figure 2.18: Comparison with related works in literature: RFIC2011 [114], AICSP2015 [116], and JSSC2011 [115].

2.5 Conclusion

This chapter proposed a dedicated antenna-free OOK transmitter that used two coils both for radiation and oscillation, which contributes to the reduction of the number of components and the consequent small implementation volume. To improve the throughput, this work developed a priori current injection technique that reduced the start-up dead time of the LC oscillation. The measurement results with the prototype whose size is 2.8 mm$\times$2.8 mm$\times$4.2 mm show that the dead time is reduced from 400 ns to 40 ns or less. This chapter also developed a baseband encoding technique that improved the energy per bit of the proposed OOK transmitter. The proposed encoding technique enables the communication speed and energy per bit to be adjustable. In energy-limited applications, the transmitter can reduce the energy per bit to 51.8 pJ/b by lowering the communication speed to 62.3 kbps. On the other hand, in speed-demanding applications, the transmitter can communicate at up to 3 Mbps at the energy per bit of 380 pJ/b.

With the current baseband encoding technique, the wireless communication is vulnerable to the interference with other communications. This problem originates from the feature that the bit width is always fixed and the encoding depends only on the bit position. To address this issue, developing the encoding method which is resistant to the interference is the primary future work. Fortunately, the spread-spectrum based encoding is proposed and already widely used in several commercial wireless transmitters such as Bluetooth Low Energy (BLE), and hence the future work can take advantage of the findings in the studies on this spread-spectrum based wireless communication.

Chapter 3

Theoretical analysis and appropriate circuit structure for 1-to-n WPT system

Most of the studies on wireless power transfer (WPT) systems focus on the enhancement of the power transmission efficiency and the robustness improvement of 1-to-1 WPT system. On the other hand, the WPT required for the tiny sensor nodes of pervasive sensing have to be suitable for 1-to-n power transmission, which means one power transmitter coil is responsible for numerous number of sensor nodes. Currently, 1-to-n WPT systems are not discussed actively and even the feasibility of the system is not sufficiently clarified while 1-to-1 WPT systems are already available on market. Therefore, this chapter discusses the feasibility of the 1-to-n WPT systems based on the analysis of both the circuit and the magnetic field. In addition, this chapter proposes and evaluates a suitable WPT circuit structure for the sensor node in pervasive sensing application.

3.1 Introduction

As described in Section 1.3.2, inductive power transfer (IPT) based WPT is a promising method of WPT for pervasive sensing in terms of its robustness and safety. The circuit structure of IPT system can be divided into two major types: series-series (S-S) type and series-parallel (S-P) type. Both S-S and S-P type structure are illustrated in Fig. 3.1. In the S-S type circuit structure, all components are connected in series both in power transmitter side and receiver side while all components in receiver side of the S-P type structure are connected in parallel. Both S-S and S-P types are actively studied in terms of those performance improvement and circuit optimization [117–121]. Here, the S-S type structure is much easier to analyze than S-P type structure since there is only one current loop on each of the transmitter side and receiver side. For this reason, this chapter focuses on S-S type circuit structure. First, this chapter derives appropriate circuit conditions from both perspectives of the power transmission efficiency and the amount of received power based on the circuit analysis. Unlike other WPT applications,

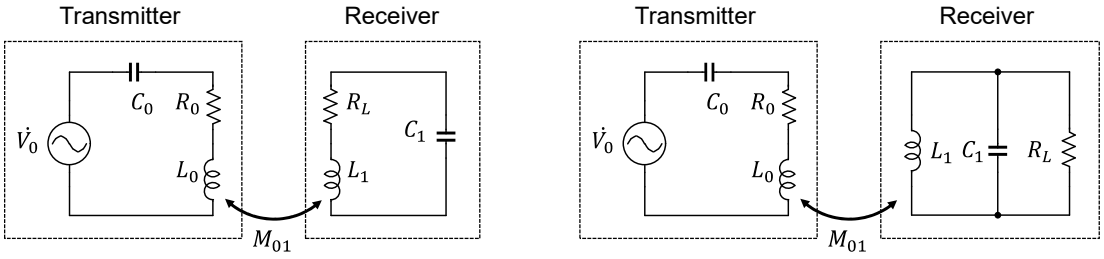

(a) S-S type WPT (b) S-P type WPT

Figure 3.1: Two general circuit structures of WPT systems. (a) S-S type WPT system, (b) S-P type WPT system.

the sensor node for the pervasive sensing applications should be automatically switched to WPT mode when the inner node energy is running out since the sensor node for the pervasive sensing should be maintenance free. To address this issue, this chapter proposes and evaluates the appropriate circuit structure for the 1-to-n WPT system which can automatically switch the circuit function between the WPT mode and wireless communication mode according to the situation while keeping the sensor volume to 1 cm^3.

The rest of this chapter is organized as follows. Section 3.2 analyzes the circuit of the WPT and shows the feasibility of the 1-to-n WPT system on the basis of the theoretical analysis. Section 3.3 proposes the appropriate circuit structure, which is equipped with the indispensable wireless communication function as well, for the 1-to-n WPT system. Section 3.4 evaluates both WPT and wireless communication functions provided by the proposed sensor node. Finally, the conclusion of this chapter is given in Section 3.5.

3.2 Problem formulation and analysis

This section analyzes the circuit of the S-S type WPT system based on both circuit theory and the magnetics. First, Section 3.2.1 analyzes the circuit of the 1-to1 WPT system and derives the most appropriate operating frequency and circuit constants in terms of the power transmission efficiency and the amount of the received power. Then, Section 3.2.2 extracts the circuit constants related to inductors (e.g. self inductance and mutual inductance) from the physical shape of the coil. Finally, the discussion on the feasibility of the 1-to-n WPT system is given in Section 3.2.3.

3.2.1 Analysis on 1-to-1 WPT system

Fig. 3.2 illustrates the general S-S type 1-to-1 WPT circuit structure. $\dot{V}_0$ is the power source connected to the power transmitter circuit. L_0 and L_1 are self inductance of the power transmitter coil and the receiver coil, respectively. M_{01} is the mutual inductance between L_0 and L_1. C_0 and C_1 are the capacitance which are utilized for tuning the

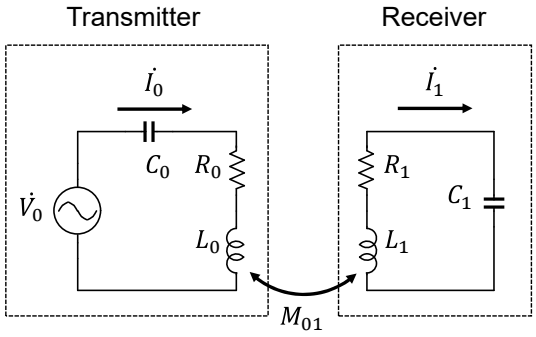

Figure 3.2: Schematic of general WPT system.

resonant frequency of the LC circuit. R_0 is the overall resistance in the power transmitter circuit which consists of the output impedance of the power source $\dot{V}_0$ and the parasitic resistance of C_0 and L_0. Similarly, R_1 denotes the resistance of the load connected in the receiver circuit and the parasitic resistance of C_1 and L_1.

KVL equation of the circuit depicted in Fig. 3.2 are given by Eqs. (3.1) and (3.2).

$$\begin{cases} \dot{V}_0 = \left\{ R_0 + j\left(\omega L_0 - \dfrac{1}{\omega C_0}\right)\right\}\dot{I}_0 + j\omega M_{01}\dot{I}_1, & (3.1) \\ 0 = \left\{ R_1 + j\left(\omega L_1 - \dfrac{1}{\omega C_1}\right)\right\}\dot{I}_1 + j\omega M_{01}\dot{I}_0, & (3.2) \end{cases}$$

where $\dot{I}_0$ and $\dot{I}_1$ are the current in the transmitter and receiver, respectively. Here, $\dot{I}_1$ is expressed with $\dot{I}_0, R_1, L_1, C_1$, and M_{01} by deforming Eq.(3.2) as shown in Eq. (3.3).

$$\dot{I}_1 = -\frac{j\omega M_{01}}{R_1 + j\left(\omega L_1 - \frac{1}{\omega C_1}\right)}\dot{I}_0. \tag{3.3}$$

The mutual inductance M_{01} is expressed with L_0, L_1, and the coupling coefficient k_{01} since the coupling coefficient is defined as Eq. (3.4).

$$k_{01} \stackrel{\text{def}}{=} \frac{M_{01}}{\sqrt{L_0 L_1}}. \tag{3.4}$$

From Eqs. (3.1), (3.3), and (3.4), $\dot{I}_0$ and $\dot{I}_1$ are both expressed only with circuit constants as introduced in Eqs. (3.5) and (3.6).

$$\begin{cases} \dot{I}_0 = \dfrac{\dot{V}_0}{R_0 + j\left(\omega L_0 - \frac{1}{\omega C_0}\right) + \frac{\omega^2 k_{01}^2 L_0 L_1}{R_1 + j\left(\omega L_1 - \frac{1}{\omega C_1}\right)}}, & (3.5) \\ \dot{I}_1 = \dfrac{-j\omega k_{01}\sqrt{L_0 L_1}\dot{V}_0}{\left\{R_0 + j\left(\omega L_0 - \frac{1}{\omega C_0}\right)\right\}\left\{R_1 + j\left(\omega L_1 - \frac{1}{\omega C_1}\right)\right\} + \omega^2 k_{01}^2 L_0 L_1}. & (3.6) \end{cases}$$

With derived $\dot{I}_0$ and $\dot{I}_1$, the power injected to the transmitter P_0 and the power received by the receiver P_1 are calculated. Here, the injected power is the work done by voltage source $\dot{V}_0$, and the received power is the power consumed in the load connected to the receiver circuit. The resistance of R_1 contains not only the resistance of the circuit load but also the parasitic resistance of components as described above. In the sensor node for the pervasive sensing, the value of the parasitic resistance of components is at most several ohm while the resistance of the load is more than several hundreds of ohm when the current consumption of the sensor node is less than several mA. Therefore, the circuit load connected to the receiver circuit predominantly determines the value of R_1. For this reason, the received power is almost as the same as the power consumed in the resistor R_1. Based on these assumptions, P_0 and P_1 are given with Eqs. (3.7) and (3.8).

$$\begin{aligned} P_0 &= \Re\left[V_0 I_0^*\right] \\ &= \frac{R_1\left(R_0R_1+\omega^2k_{01}^2L_0L_1\right)+R_0X_0X_1}{\left(R_0^2+X_0^2\right)\left(R_1^2+X_1^2\right)+\omega^2k_{01}^2L_0L_1\left(\omega^2k_{01}^2L_0L_1+2R_0R_1-2X_0X_1\right)}\dot{V_0}^2, \end{aligned} \tag{3.7}$$

$$\begin{aligned} P_1 &= \Re\left[R_1 I_1 I_1^*\right] \\ &= \frac{R_1\omega^2k_{01}^2L_0L_1}{\left(R_0^2+X_0^2\right)\left(R_1^2+X_1^2\right)+\omega^2k_{01}^2L_0L_1\left(\omega^2k_{01}^2L_0L_1+2R_0R_1-2X_0X_1\right)}\dot{V_0}^2, \end{aligned} \tag{3.8}$$

where the mark of * represents the conjugate of the complex number. X_0 and X_1 in Eqs. (3.7) and (3.8) are defined as follows:

$$X_0 \stackrel{\text{def}}{=} \omega L_0 - \frac{1}{\omega C_0}, \quad X_1 \stackrel{\text{def}}{=} \omega L_1 - \frac{1}{\omega C_1}. \tag{3.9}$$

The power transmission efficiency is calculated by Eq. (3.10).

$$\begin{aligned} \eta_{01} &= \frac{P_1}{P_0} \\ &= \frac{\omega^2k_{01}^2L_0L_1}{R_0R_1+\omega k_{01}^2L_0L_1+\frac{R_0}{R_1}X_0X_1}. \end{aligned} \tag{3.10}$$

To improve not only the power transmission efficiency but also the power efficiency of the entire circuit, the power factor of the circuit should be close to 1, which means the imaginary part of $\dot{I}_0$ should be 0. Eq. (3.5) suggests that if the operating frequency ω satisfies the following equation, the imaginary part of $\dot{I}_0$ becomes zero.

$$\omega = \frac{1}{\sqrt{L_0C_0}} = \frac{1}{\sqrt{L_1C_1}}. \tag{3.11}$$

When Eq. (3.11) is satisfied, P_0, P_1 and η_{01} become Eqs. (3.12), (3.13), and (3.14), respectively.

$$P_0 = \frac{R_1}{R_0R_1+\omega^2k_{01}^2L_0L_1}\dot{V_0}^2, \tag{3.12}$$

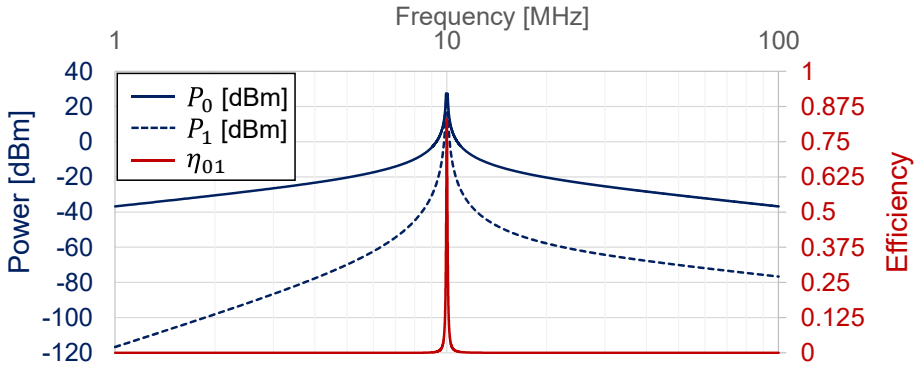

Figure 3.3: Simulated P_0, P_1 and η_{01} when $\dot{V}_0 = 1$ [V], $L_0 = L_1 = 3.500$ [μH], $C_0 = C_1 = 72.37$ [pF], $R_0 = R_1 = 1$ [Ω] and $k_{01} = 0.01$.

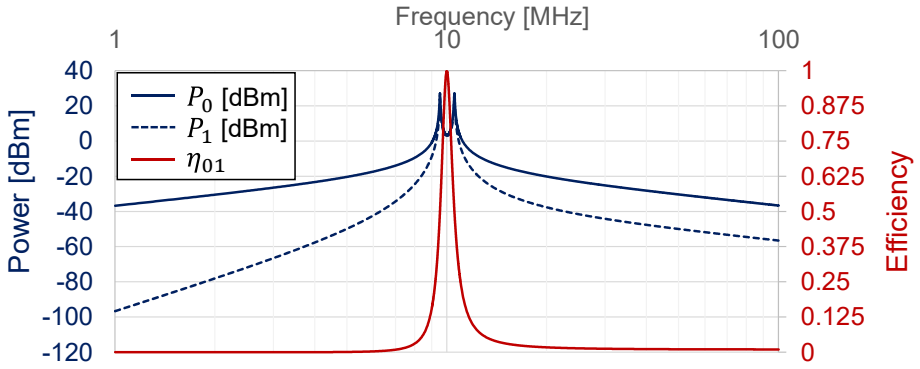

Figure 3.4: Simulated P_0, P_1 and η_{01} when $\dot{V}_0 = 1$ [V], $L_0 = L_1 = 3.500$ [μH], $C_0 = C_1 = 72.37$ [pF], $R_0 = R_1 = 1$ [Ω], and $k_{01} = 0.1$.

$$P_1 = \frac{R_1 \omega^2 k_{01}^2 L_0 L_1}{\left(R_0 R_1 + \omega^2 k_{01}^2 L_0 L_1\right)^2} \dot{V}_0{}^2, \tag{3.13}$$

$$\eta_{01} = \frac{\omega^2 k_{01}^2 L_0 L_1}{R_0 R_1 + \omega^2 k_{01}^2 L_0 L_1}. \tag{3.14}$$

As examples, Figs. 3.3, 3.4, and 3.5 show the simulation results when the circuit constants are set as follows: $\dot{V}_0 = 1$ [V], $L_0 = L_1 = 3.500$ [μH], $C_0 = C_1 = 72.37$ [pF], $R_0 = R_1 = 1$ [Ω], which means the circuit structures of the power transmission side and the reception side are symmetrical, and the resonance frequency is 10 MHz. The coupling coefficient k_{01} of each simulation shown in Figs. 3.3, 3.4, and 3.5 are set to $k = 0.01$, $k = 0.1$, and $k = 0.5$, respectively. Figs. 3.3, 3.4, and 3.5 indicate that the power transmission efficiency η_{01} always takes the maximum value when the operating frequency ω is matched to the resonant frequency. On the other hand, P_0 and P_1 may have two peaks when the coupling coefficient is larger than $k = 0.1$ as shown in Figs. 3.4, and 3.5. These results indicate that the frequency at which η_{01} is maximized and the

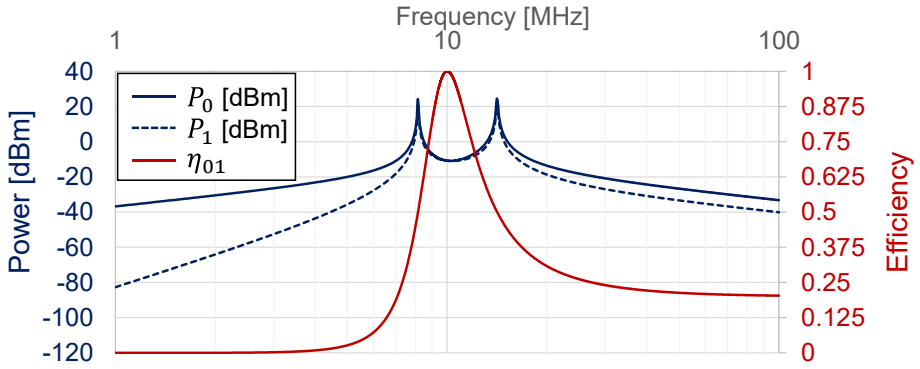

Figure 3.5: Simulated P_0, P_1 and η_{01} when $\dot{V}_0 = 1$ [V], $L_0 = L_1 = 3.500$ [μH], $C_0 = C_1 = 72.37$ [pF], $R_0 = R_1 = 1$ [Ω], and $k_{01} = 0.5$.

frequency at which P_0 and P_1 are maximized do not always match. Here, interestingly, even if η_{01} is large, the energy available in the receiver side is small since the transmitted power is small. Therefore, the peak frequencies of P_0, P_1, and η_{01} should match each other.

To clarify the operating conditions of the circuit where the peak frequencies of P_0, P_1, and η_{01} match, the following first investigates the relationship between k_{01} and the two frequency peaks of P_0 and P_1 assuming that $L_0C_0 = L_1C_1$ is satisfied, just like many of WPT applications. In Figs. 3.3, 3.4, and 3.5, given $\dot{V}_0$ is identical, and hence the difference of the value of P_0 and P_1 should be caused by the difference of the power factor. When the power factor is close to 1, the reactive power of the circuit should be zero. Figs. 3.6 and 3.7 show results of simulation on the reactive power Q_0 of the power transmission circuit under the same conditions as Figs. 3.4 and 3.5, respectively. Here, Q_0 is calculated by Eq. (3.15).

$$\begin{aligned} Q_0 &= \Im\left[V_0 I_0^*\right] \\ &= \frac{R_1^2 X_0 + X_1\left(X_0 - \omega^2 k_{01}^2 L_0 L_1\right)}{\left(R_0^2 + X_0^2\right)\left(R_1^2 + X_1^2\right) + \omega^2 k_{01}^2 L_0 L_1\left(\omega^2 k_{01}^2 L_0 L_1 + 2R_0R_1 - 2X_0X_1\right)} \dot{V}_0{}^2, \end{aligned} \tag{3.15}$$

Figs. 3.6 and 3.7 indicate that the reactive power Q_0 become zero at the peak frequency of P_0 as expected. On the other hand, deriving the value of ω that satisfies $Q_0 = 0$ results in finding the solution of the quintic equation and hence the analytical solution may not be obtained. Instead, Figs. 3.6 and 3.7 strongly imply that the frequency characteristic of Q_0 is highly related to that of the LC circuit. Therefore, we can come to know the number of frequency peaks of P_0 by solving the equation of $Q_0 = 0$ under the condition where $R_0 = R_1 = 0$ although we cannot derive the exact peak frequency. We can obtain Eq. (3.16) by substituting $R_0 = R_1 = 0$ in Eq. (3.15).

$$Q_0 = \frac{X_1\left(X_0 - \omega^2 k_{01}^2 L_0 L_1\right)}{\left(X_0 X_1 - \omega^2 k_{01}^2 L_0 L_1\right)^2} \dot{V}_0{}^2. \tag{3.16}$$

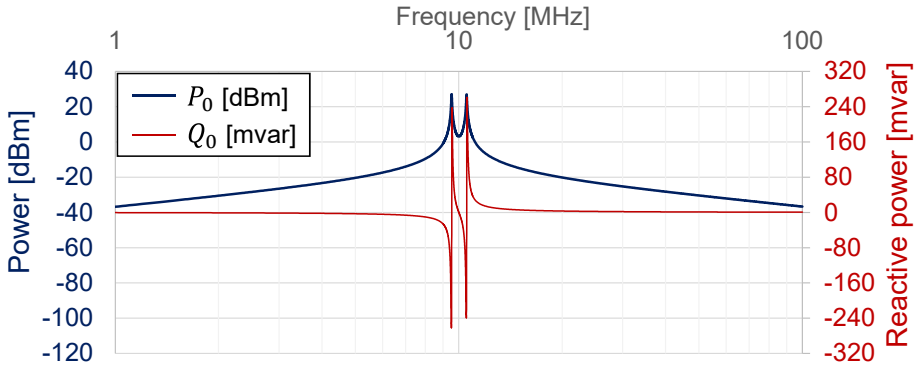

Figure 3.6: Simulated P_0 and Q_0 when $\dot{V}_0 = 1$ [V], $L_0 = L_1 = 3.500$ [μH], $C_0 = C_1 = 72.37$ [pF], $R_0 = R_1 = 1$ [Ω], and $k_{01} = 0.1$.

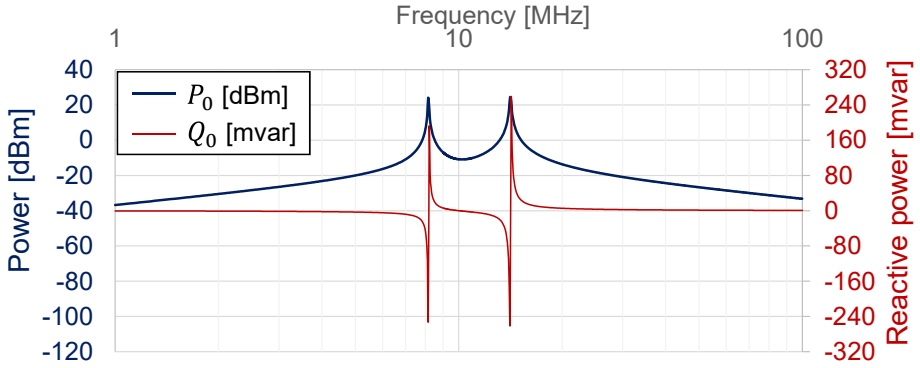

Figure 3.7: Simulated P_0 and Q_0 when $\dot{V}_0 = 1$ [V], $L_0 = L_1 = 3.500$ [μH], $C_0 = C_1 = 72.37$ [pF], $R_0 = R_1 = 1$ [Ω], and $k_{01} = 0.5$.

When we set $R_0 = R_1 = 0$, Q_0 should take the value of $\pm\infty$ at the resonant frequencies, whereas Q_0 becomes 0 when $R_0 \neq 0, R_1 \neq 0$. When Q_0 takes the value of $\pm\infty$, the denominator of Eq. (3.16) should be zero. Therefore, the number of the frequency peak of P_0 matches with the number of solutions of Eq. (3.17).

$$\left(\omega L_0 - \frac{1}{\omega C_0}\right)\left(\omega L_1 - \frac{1}{\omega C_1}\right) - \omega^2 k_{01}^2 L_0 L_1 = 0. \tag{3.17}$$

The solution of Eq. (3.17) under the condition of $\omega > 0$ is given by Eq. (3.18).

$$\omega = \sqrt{\frac{L_0C_0 + L_1C_1 \pm \sqrt{L_1^2C_1^2 + L_0^2C_0^2 - 2\left(1 - 2k_{01}^2\right)L_0C_0L_1C_1}}{2\left(1 - k_{01}^2\right)L_0C_0L_1C_1}} \tag{3.18}$$

Eq. (3.18) shows that the number of the peak frequencies of P_0 depends on the coupling coefficient k_{01} In the pervasive sensing application, one power transmission circuit is responsible for hundreds or even thousands of tiny sensor nodes. In this situation, the

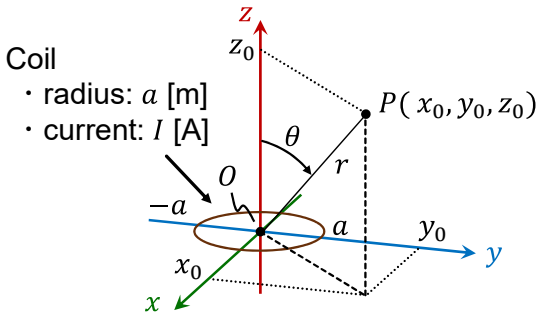

Figure 3.8: Coordinate setting and definition of variables.

size of the coil used for the power receiver is far smaller than that of the power transmitter coil, and hence the coupling coefficient k_{01} is close to zero. Here, the value of the coupling coefficient between the transmitter and receiver coil will be discussed in detail in Section 3.2.2. When $k_{01} \sim 0$, Eq. (3.18) is approximated by Eq. (3.19).

$$\omega = \frac{1}{\sqrt{L_0 C_0}}, \frac{1}{\sqrt{L_1 C_1}} \tag{3.19}$$

Eq. (3.19) indicates that the number of the frequency peak of P_0 is two at maximum and those frequencies depend on the values of L_0C_0 and L_1C_1. As described with Eq. (3.11), $L_0C_0 = L_1C_1$ should be satisfied to keep the power factor of the circuit be one. Under the condition of $L_0C_0 = L_1C_1$, Eq. (3.19) only takes single value of $\omega = 1/\sqrt{L_0C_0} = 1/\sqrt{L_1C_1}$. As described with Figs. 3.3, 3.4, and 3.5, the peak frequency of η_{01} is always at $\omega = 1/\sqrt{L_0C_0} = 1/\sqrt{L_1C_1}$ under the condition of $L_0C_0 = L_1C_1$. Hence, when we set the inductance and capacitance to satisfy $L_0L_1 = C_0C_1$ and the coupling coefficient k_{01} is close to zero, the single frequency peak of P_0 matches with the frequency peak of η_{01}. In other words, the power factor and the power transmission efficiency are both maximized at the frequency of $\omega = 1/\sqrt{L_0C_0} = 1/\sqrt{L_1C_1}$ when we build the loosely coupled WPT system. The 1-to-n WPT system for the pervasive sensing, which this dissertation is focusing on, almost always satisfies the condition that the coupling coefficient between the transmitter and the receiver coil is very small and close to nearly zero, which will be discussed in detail in the following section.

3.2.2 Circuit constants related to inductor

Self inductance of the coil

This section derives the self inductance of the coil L_0 whose winding number is one. Although a method for approximately deriving the self inductance of the single loop coil is reported decades ago [122], this section introduces a calculation method based on the magnetic flux density based on the definition of the inductance.

The self inductance of the coil strongly depends on the amount of the magnetic flux density generated by the coil itself. Then, the objective here is to obtain the equation which can derive the magnetic flux density generated by the coil. Fig. 3.8 shows the coordinate setting and definitions of the variables r, θ, x_0, y_0 and z_0. As shown in Fig. 3.8, the single loop coil is placed on xy-plane, and the center of the coil is set to the origin of the xyz-coordinate system. When we inject the current I [A] to the coil whose radius is a [m], the magnetic flux density $\mathbf{B}_P$ at the point P is obtained by calculating Eq. (3.20) [44].

$$\mathbf{B}_P(a, I, \mathbf{P}) = \frac{\mu_0 I a}{4\pi} \int_0^{2\pi} \frac{a\cos\theta \mathbf{e}_r + (r\sin\phi - a\sin\theta)\mathbf{e}_\theta}{(r^2 + a^2 - 2ra\sin\theta\sin\phi)^{3/2}} d\phi, \tag{3.20}$$

where μ_0 is the magnetic constant, ϕ is the integration variable, and $\mathbf{e}_r$ and $\mathbf{e}_\theta$ are unit vectors pointing r and θ direction, respectively. $\mathbf{P}$ denotes the position vector of the point P. Eq. (3.21) derives B_{Px}, B_{Py}, and B_{Pz}, which are x, y, and z component of the magnetic flux density B_P respectively:

$$\begin{aligned}
B_{Px} &= \frac{x_0 z_0}{\sqrt{x_0^2 + y_0^2}} \frac{\mu_0 I a}{4\pi} \int_0^{2\pi} \frac{\sin\phi}{\left(x_0^2 + y_0^2 + z_0^2 + a^2 - 2a\sin\phi\sqrt{x_0^2 + y_0^2}\right)^{3/2}} d\phi, \\
B_{Py} &= \frac{y_0 z_0}{\sqrt{x_0^2 + y_0^2}} \frac{\mu_0 I a}{4\pi} \int_0^{2\pi} \frac{\sin\phi}{\left(x_0^2 + y_0^2 + z_0^2 + a^2 - 2a\sin\phi\sqrt{x_0^2 + y_0^2}\right)^{3/2}} d\phi, \\
B_{Pz} &= \frac{\mu_0 I a}{4\pi} \int_0^{2\pi} \frac{a - \sin\phi\sqrt{x_0^2 + y^2}}{\left(x_0^2 + y_0^2 + z_0^2 + a^2 - 2a\sin\phi\sqrt{x_0^2 + y_0^2}\right)^{3/2}} d\phi.
\end{aligned} \tag{3.21}$$

Note that B_{Px}, B_{Py}, and B_{Pz} satisfy the following relationship:

$$\begin{aligned}
\mathbf{B}_P(a, I, \mathbf{P}) &= \begin{bmatrix} B_{Px} \\ B_{Py} \\ B_{Pz} \end{bmatrix} \\
&= B_{Px} \cdot \mathbf{e}_x + B_{Py} \cdot \mathbf{e}_y + B_{Pz} \cdot \mathbf{e}_z,
\end{aligned} \tag{3.22}$$

where $\mathbf{e}_x, \mathbf{e}_y$, and $\mathbf{e}_z$ denote unit vectors pointing x, y, and z direction respectively.

As described in the beginning of this section, the self inductance of the coil depends on the magnetic flux density generated by the coil. In particular, the self inductance of the coil is the amount of magnetic flux density that pass through the coil itself perpendicularly when the current of 1 A is applied to the coil. Therefore, the self inductance of the coil is obtained by integrating all magnetic flux density perpendicular to the coil in the area surrounded by the wire. This is expressed by Eq. (3.23).

$$\begin{aligned}
L_0 &= \int_S \mathbf{B}_P(a, 1, \mathbf{P}) \cdot \mathbf{e}_z \, dS \\
&= \int_S B_{Pz}(a, 1, \mathbf{P}) \, dS,
\end{aligned} \tag{3.23}$$

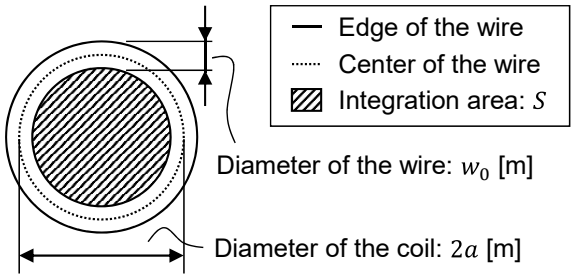

Figure 3.9: Integration area for deriving the self inductance of the sensing coil.

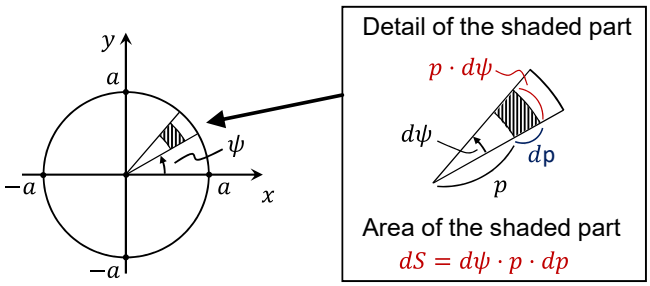

Figure 3.10: Area and position of minute part required for integration.

where $\mathbf{P}$ denotes all points in the integration area S. Eq. (3.23) calculates inner product between $\mathbf{B}_P$ and $\mathbf{e}_z$ to extract the magnetic flux density which is perpendicular to the coil. In addition, the current injected to the coil is set to 1 [A] by the definition of the self inductance. Fig. 3.9 shows the integration area. As illustrated in Fig. 3.9, the integration area S is not identical to the circle whose radius is a. Rather than that, the integration area is the circular area whose radius is $a - w_0/2$ [m]. Fig. 3.10 introduces two variables p and ψ to express dS. When the dp and $d\psi$ is infinitely small, dS is calculated by $dS = d\psi \cdot p \cdot dp$. By introducing these variables and the relationship, Eq. (3.23) becomes Eq.(3.24).

$$\begin{aligned} L_0 &= \int_0^{a-\frac{w_0}{2}} \int_0^{2\pi} \mathbf{B}_P \left(a, 1, \begin{bmatrix} p\cos\psi \\ p\sin\psi \\ 0 \end{bmatrix} \right) \cdot \mathbf{e}_z \, d\psi \cdot p \cdot dp \\ &= \int_0^{a-\frac{w_0}{2}} \int_0^{2\pi} B_{P_z} \left(a, 1, \begin{bmatrix} p\cos\psi \\ p\sin\psi \\ 0 \end{bmatrix} \right) \, d\psi \cdot p \cdot dp. \end{aligned} \tag{3.24}$$

By calculating Eq. (3.24), the self inductance of the coil L_0 can be obtained. However, Eq. (3.24) cannot be solved analytically, and hence we have to derive the inductance value by numerical integration instead. To conduct numerical integration, let us divide the integration range of p and ψ into a finite number of small parts. If we divide the integration range of p and ψ equally into n_p parts and n_ψ parts, respectively, dp and $d\psi$

are described as Eq. (3.25).

$$dp = \frac{a - w_0/2}{n_p}, \quad d\psi = \frac{2\pi}{n_\psi}. \tag{3.25}$$

When each part of dp and $d\psi$ are small enough, in other words, the values of n_p and n_ψ are sufficiently large, Eq. (3.26) approximates Eq. (3.24).

$$L_0 = \sum_{i=1}^{n_p} \sum_{j=1}^{n_\psi} B_{P_z} \left(a, 1, idp \begin{bmatrix} \cos jd\psi \\ \sin jd\psi \\ 0 \end{bmatrix} \right) \cdot \, d\psi \cdot i \cdot dp^2. \tag{3.26}$$

Here, p and ψ are expressed based on following relationship: $p = idp, \ \psi = jd\psi$. By calculating Eq. (3.26), the self inductance of the coil is derived.

Mutual inductance between two coils

The mutual inductance between two coils is the amount of the magnetic flux density which is generated by the primary coil and pass through the secondary coil perpendicularly. Therefore, the basic integration procedure is almost as same as the procedure for calculating the self inductance of the coil. The mutual inductance M_{0m} between the primary coil and the secondary coil is expressed by Eq. (3.27).

$$M_{0m} = \int_{S'} \mathbf{B}_P (a, 1, \mathbf{P}_m) \cdot \mathbf{e}_Z \, dS', \tag{3.27}$$

where $\mathbf{P}_m$ is the point surrounded by the wire of the secondary coil and $\mathbf{e}_Z$ is the unit vector perpendicular to the secondary coil. The integration introduced in Eq. (3.27) is conducted in the area surrounded by the wire of the secondary coil, and therefore we have to derive the coordinate of the point $\mathbf{P}_m$. To simplify the discussion, this section assumes that the secondary coil is placed parallel to the primary coil, which means $\mathbf{e}_z = \mathbf{e}_Z$ and the coordinate of the center of the primary coil is (x_m, y_m, z_m) as shown in Fig. 3.11. In this case, the coordinate of the point on the area surrounded by the wire of the secondary coil is expressed by Eq. (3.28).

$$\mathbf{P}_m = \begin{bmatrix} x_m + p_m \cdot \cos\psi \\ y_m + p_m \cdot \sin\psi \\ z_m \end{bmatrix}, \tag{3.28}$$

where p_m satisfies the following formula with the radius of the secondary coil r_m: $0 \leq p_m \leq r_m$. Based on the similar idea to Eq. (3.24), we can evaluate the mutual inductance between two coils with Eq. (3.29).

$$\begin{aligned} M_{0m} &= \int_0^{r_m - \frac{w_m}{2}} \int_0^{2\pi} \mathbf{B}_P (a, 1, \mathbf{P}_m) \cdot \mathbf{e}_Z \, d\psi \cdot p_m \cdot dp_m \\ &= \int_0^{r_m - \frac{w_m}{2}} \int_0^{2\pi} B_{P_z} (a, 1, \mathbf{P}_m) \ d\psi \cdot p_m \cdot dp_m, \end{aligned} \tag{3.29}$$

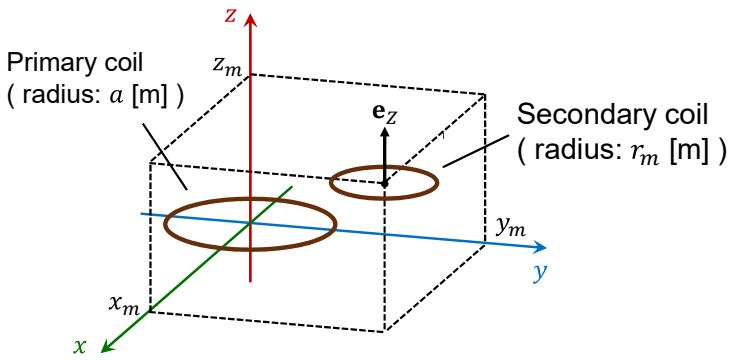

Figure 3.11: The positional relationship between the primary and the secondary coils.

where w_m is the diameter of the wire composing the secondary coil. Similar to Eq. (3.26), Eq. (3.29) can also be transformed into the equation with sigma operator as shown in Eq. (3.30) so that we can evaluate the value by numerical simulation.

$$M_{0m} = \sum_{i=1}^{n_{pm}} \sum_{j=1}^{n_\psi} B_{P_z}(a, 1, \mathbf{P}_m)\ d\psi \cdot i \cdot dp_m^2, \tag{3.30}$$

where n_{pm} and n_ψ denote the numbers of divisions regarding the integration area and each variable is defined as Eq. (3.31).

$$\begin{cases} dp_m = \frac{r_m - w_m/2}{n_{pm}}, \\ d\psi = \frac{2\pi}{n_\psi}, \\ p_m = i \cdot dp_m, \\ \psi = j \cdot d\psi. \end{cases} \tag{3.31}$$

Once the self inductances of coils and the mutual inductance between them are derived, we can calculate the coupling coefficient with Eq. (3.4).

Simulation of coupling coefficient

Section 3.2.1 revealed that if the coupling coefficient is negligibly small, the peak frequency of the power transmission efficiency and that of the amount of the received power match each other. In this case, we do not have to tune the operating frequency or the circuit constants according to the position of the sensor node, and hence the robustness of the system is ensured. Therefore, the important objective of this section is to show that the coupling coefficient between the transmitter coil and receiver coil is negligibly small. Addressing this point, this section conducts a simulation experiment and derive the inductances of the transmission and receiver coil and the coupling coefficient between transmission and receiver coil. To simplify the discussion, this section assumes

Table 3.1: Specifications of coils used for simulation.

	Transmitter coil	Receiver coil
Diameter of the coil	1.0 m	10 mm
Diameter of the wire	1 mm	0.1 mm

that the all inductors have a shape of single loop coil. Another discussion utilizing the coil which is not in the shape of single loop coil will be introduced in Section 3.2.3.

As a simulation model, this work assumes that the power transmitter coil whose diameter is 1 meter is responsible for thousands of power receiver coils whose diameter is 10 mm. Table 3.1 shows the detailed specifications of the coils. The self inductances of transmitter and receiver coils, which are calculated based on Eq. (3.26), are 3.657 μH and 28.83 nH, respectively. To confirm the location dependence of the coupling coefficient between the transmitter coil and the receiver coil, this section calculates the coupling coefficient between them supposing that the transmitter coil is fixed and only the receiver coil is moved. Fig. 3.12 introduces the heatmap of the coupling coefficient when the transmitter coil is placed on *xy*-plane and the center of the coil is set to the origin. The moving area of the receiver coil is -1.0 [m] $\leq y \leq$ 1.0 [m] and 0.01 [m] $\leq z \leq$ 2.0 [m]. The transmitter coil and the receiver coil are both placed parallel to *xy*-plane and facing each other. Fig. 3.12 indicates that the coupling coefficient between the transmitter and the receiver coil is 2.54×10^{-3} at maximum and negligible compared to 1. Consequently, in 1-to-n WPT system, which the diameter of the transmitter coil is 100 times larger than the diameter of the receiver coil, the coupling coefficient between them are negligibly small and both the power transmission efficiency and the received power are maximized at the same fixed frequency as long as the product of *LC* is set as $L_0C_0 = L_1C_1$.

3.2.3 Analysis on 1-to-n WPT system

Section 3.2.1 revealed that both the received power and the power transmission efficiency are maximized at the resonant frequency of the LC circuit when the coupling coefficient between the transmitter and the receiver coils is negligibly small. Section 3.2.2 experimentally proved that the coupling coefficient between the transmitter and the receiver coil is negligibly small compared to 1 when the diameters of coils are significantly different, and the operating frequency can be fixed to the resonant frequency of the LC circuit. Based on these findings, this section analyzes the power transmission efficiency when the number of node is larger than 1 while Section 3.2.1 analyzed only when the number of power receiver node is 1.

Fig 3.13 shows the circuit structure of 1-to-n WPT system under analysis. Fig 3.13 indicates that one transmitter coil is responsible for n receiver circuits. Not only the coupling between the transmitter and one receiver coil but also the coupling between

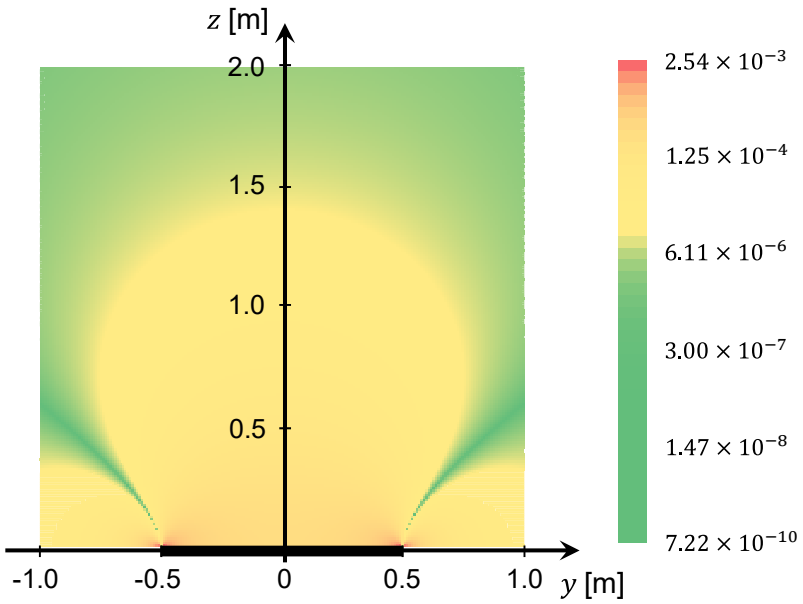

Figure 3.12: Heatmap of the coupling coefficient between the transmitter coil and the receiver coil. The transmitter coil is placed on *xy*-plane and the center of the coil is set to the origin. Diameter of the transmitter coil is 1 m and the diameter of the wire used for transmitter coil is 1 mm. Diameter of the receiver coil is 10 mm and the wire diameter is 0.1 mm. The moving area of the receiver coil is -1.0 [m] $\leq y \leq$ 1.0 [m], and 0.01 [m] $\leq z \leq$ 2.0 [m]. The transmitter coil and the receiver coil are both placed parallel to *xy*-plane and facing each other.

any pairs of two receiver coils, which is depicted as M_{ll+1} , are to be considered. Section 3.2.1 explained that the mutual inductance between two coils affects the circuit behavior and the mutual inductance is determined by the values of self inductances of two coils and the coupling coefficient as described with Eq. (3.4). Here, the self inductance of the receiver coil is far smaller than that of the transmitter coil as described in the previous section, where the inductance of the transmitter coil and the receiver coil is 3.657 µH and 28.83 nH, respectively. Hence, the effect of the mutual coupling between two receiver coils might be negligible. To confirm the effect of the mutual inductance between receiver coils, a simulation experiment is performed for the system that contains one transmitter coil and two receiver coils. Fig. 3.14 shows the simulation setup. The diameter of the transmitter coil and the receiver coil are 1 m and 1 cm, respectively, and the diameter of the wire used for the transmitter and the receiver coil are 1mm and 0.1 mm, respectively. The transmitter coil and one receiver coil are place on *xy*-plane and center of those coil is set to the origin of the coordinate while one receiver coil moves along z axis as shown in Fig. 3.14. As for transmitter coil, the resistance and the capacitance are set as $R_0 = 1$ [Ω], $C_0 = 69.27$ [pF]. The capacitance of the receiver coils is set as $C_l = 8.787$ [nF] so that the resonance frequency is tuned to 10 MHz. Chapter 2

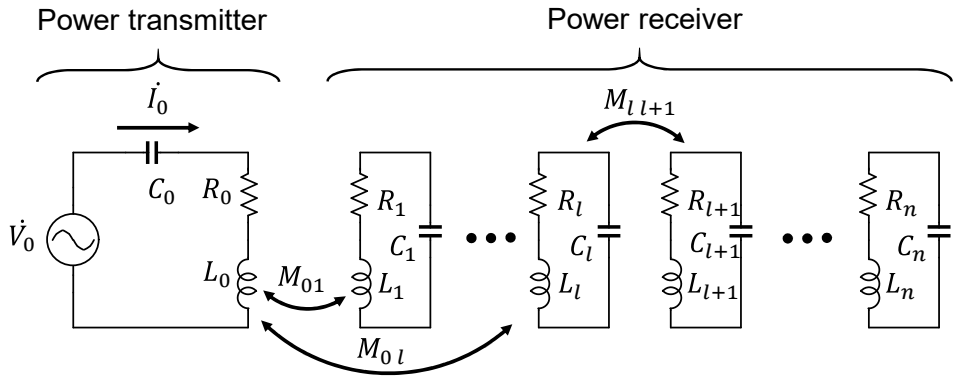

Figure 3.13: The circuit of the 1-to-n WPT system.

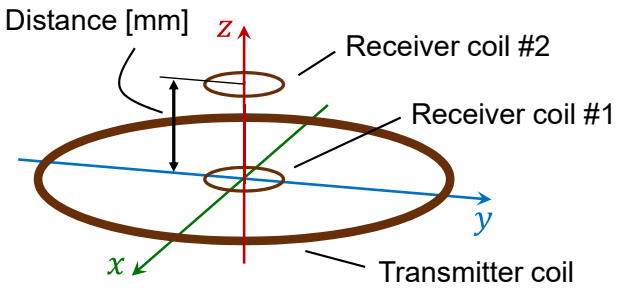

Figure 3.14: Simulation setup. The diameter of the transmitter coil and the receiver coil is 1 m and 1 cm, respectively. The diameter of the wire used for transmitter and receiver coil is 1mm and 0.1 mm, respectively.

revealed that the wireless communication circuit, which is the most energy consuming circuit in the tiny sensor node for pervasive sensing, consumes approximately 1 mA of current, and hence the resistance of the receiver coil is set to 1 kΩ. The coupling coefficient for any pair of two coils out of three coils is derived based on Eqs. (3.30) and (3.4), and the power consumed at the resistor of receiver coil #1 is evaluated with HSPICE circuit simulator. Fig. 3.15 shows two results: P_1 and P_1'. P_1 denotes the power consumed in the resistor of receiver coil #1 when the mutual coupling between two receiver coils is considered while P_1' do not consider the coupling between two receiver coils. Fig. 3.15 indicates that the difference between P_1 and P_1' is very small and the error between them is only 3.29×10^{-4} % even when the coupling coefficient between two receiver coils is 1, which means two receiver coils are overlapped completely. This result insists that we can ignore the effect of the coupling between receiver coils and can perform the theoretical analysis based on this assumption.

Based on the observation introduced above, this section derives the theoretical equation focusing on the power transmission efficiency. Here, the power transmission efficiency η_{all} is calculated with the total power received by all the receiver nodes and the

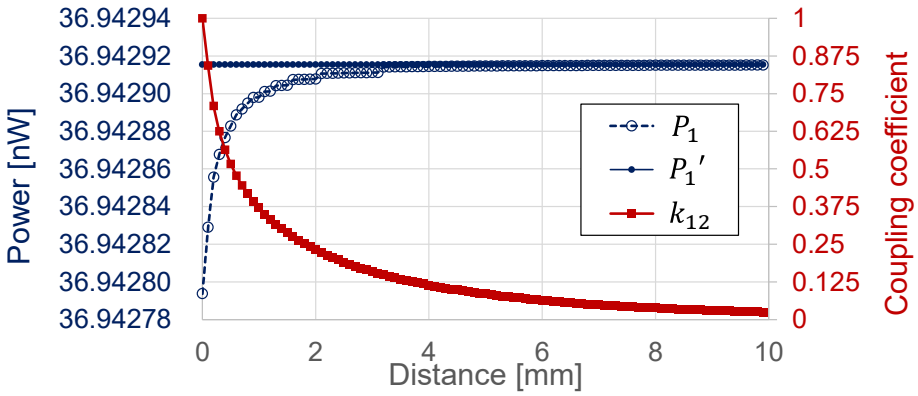

Figure 3.15: HSPICE simulation result.

power injected to the transmitter coil, which is expressed with Eq. (3.32).

$$\eta_{all} = \frac{\sum_{l=1}^{n} P_l}{P_0} \tag{3.32}$$

To derive P_0 and P_l, let us build KVL equations on the transmitter coil and the receiver coil # l as explained with Eqs. (3.33) and (3.34).

$$\begin{cases} \dot{V}_0 = R_0 + j\omega \sum_{l=1}^{n} M_{0l}\dot{I}_l, & (3.33) \\ 0 = R_1 + j\omega M_{0l}\dot{I}_0. & (3.34) \end{cases}$$

In Eqs. (3.33) and (3.34), we assume that the operating frequency ω is set to the resonant frequency of the LC circuit, and hence terms on L_0, L_1, C_0 and C_1 are not included. $\dot{I}_0$ and $\dot{I}_l$ are derived as Eqs. (3.35) and (3.36) by solving Eqs. (3.33) and (3.34).

$$\begin{cases} \dot{I}_0 = \dfrac{\dot{V}_0}{R_0 + \omega^2 \sum_{l=1}^{n} \frac{M_{0l}^2}{R_l}}, & (3.35) \\ \dot{I}_l = \dfrac{j\omega M_{0l}\dot{V}_0}{R_l \left(R_0 + \omega^2 \sum_{l=1}^{n} \frac{M_{0l}^2}{R_l} \right)}. & (3.36) \end{cases}$$

With Eqs. (3.35) and (3.36), P_0, P_l and η_{all} are derived as Eqs. (3.37), (3.38) and (3.39).

$$\begin{cases} P_0 = \Re\left[\dot{V}_0 \dot{I}_0^*\right] = \dfrac{\dot{V}_0{}^2}{R_0 + \omega^2 \sum_{l=1}^{n} \frac{M_{0l}^2}{R_l}}, & (3.37) \\ P_l = \Re\left[R_l \dot{I}_l \dot{I}_l^*\right] = \dfrac{\omega^2 M_{0l}^2 \dot{V}_0{}^2}{R_l \left(R_0 + \omega^2 \sum_{l=1}^{n} \frac{M_{0l}^2}{R_l}\right)^2}, & (3.38) \\ \eta_{all} = \dfrac{\sum_{l=1}^{n} P_l}{P_0} = \left(\dfrac{\omega^2}{R_0 + \omega^2 \sum_{l=1}^{n} \frac{M_{0l}^2}{R_l}}\right) \sum_{l=1}^{n} \dfrac{M_{0l}^2}{R_l}. & (3.39) \end{cases}$$

Here, if all receiver coils have the same circuit constants, which means $R_1 = R_2 = \cdots = R_n$ and $L_1 = L_2 = \cdots = L_n$ are satisfied, Eq. (3.39) becomes Eq. (3.40).

$$\eta_{all} = \left(\frac{\omega^2}{R_0 + \omega^2 \sum_{l=1}^{n} \frac{k_{0l}^2 L_0 L_l}{R_l}}\right) \sum_{l=1}^{n} \frac{k_{0l}^2 L_0 L_l}{R_l} = \frac{\omega^2 L_0 L_1 \sum_{l=1}^{n} k_{0l}^2}{R_0 R_1 + \omega^2 L_0 L_1 \sum_{l=1}^{n} k_{0l}^2}. \quad (3.40)$$

To asses the value range of k_{0l}^2, this section conducts a Monte Carlo simulation scattering a large number of receiver coils to the limited area. In the simulation, 500 receiver coils whose diameters are 1 cm are scattered in the area of -1.0 [m] $\leq x \leq$ -1.0 [m], -1.0 [m] $\leq y \leq$ -1.0 [m], 0.0 [m] $\leq z \leq$ 2.0 [m], and the transmitter coil whose diameter is 1 m is installed on xy plane setting the center of the coil to the origin of the coordinate. 100 times Monte Carlo simulation was performed. The average of the obtained k_{0l}^2 is 1.7978×10^{-8} and the standard deviation of k_{0l}^2 is 3.8349×10^{-8}. Here, although the standard deviation is large compared to the value of the average, let us focus on the average of k_{0l}^2 since evaluating average performance of the system helps clarify feasibility. Therefore, the following theory-based discussion supposes $\sum_{l=1}^{n} k_{0l}^2$ by Eq. (3.41).

$$\sum_{l=1}^{n} k_{0l}^2 \approx 1.7978n \times 10^{-8}. \quad (3.41)$$

To confirm the validity of Eqs. (3.40) and (3.41), this section carries out Monte Carlo simulations changing the number of nodes to be scattered. The simulation setup is the same as the previous Monte Carlo simulation and the resistance of the transmitter and receiver coil are set as $R_0 = 1$ [Ω] and $R_1 = 1$ [kΩ], which are also same value used above. The power transmission efficiency of the circuit is evaluated by HSPICE and the coupling coefficients between receiver nodes are considered in HSPICE simulation while the theoretical equation ignores those. Fig, 3.16 shows the comparison result between HSPICE simulation and the theory based on Eq. (3.40). Error bar of the HSPICE simulation result represents its standard deviation. Fig. 3.16 indicates that the average

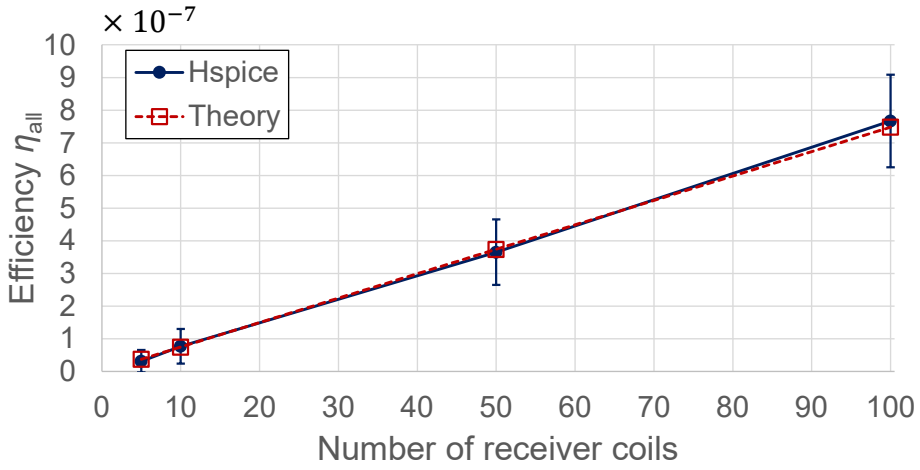

Figure 3.16: Comparison between HSPICE simulation result and the theory based on Eq. (3.40).

of the HSPICE simulation result matches well with the theoretical equation. The error between the HSPICE result and Eq. (3.40) is smaller than 2.93 % when the number of receiver coils is larger than 10 and the error gets further smaller as the number of nodes increases. Hence, we can say that Eq. (3.40) can simulate the behavior of 1-to-n WPT systems with high accuracy. Fig. 3.16 also indicates that the power transmission efficiency is smaller than 7.669×10^{-8} even when 100 receiver coils are scattered in the system, and hence the following discusses the efficiency enhancement of 1-to-n WPT system.

Eq. (3.40) indicates that increasing ω, L_0, L_1, and k_{0l} and decreasing R_0 and R_l contribute to the improvement of the power transmission efficiency. The operation frequency of the circuit is to be the LC resonant frequency, and hence should not be changed. To increase the inductances of L_0 and L_1, we have to increase the diameter of the coil or the number of turns. As long as the volume of the node is limited, the diameter of the coil cannot be increased but the winding number can be increased relatively easier. Here, the self inductance of the coil is proportional to the square of the number of turns if there is no magnetic leakage in the coil. Therefore, if the winding number of transmitter and receiver coil are k and m respectively, the self inductance of transmitter coil L_0' and the receiver coil L_1' become as follows:

$$L_0' = k^2 L_0, \quad L_1' = m^2 L_1. \tag{3.42}$$

The mutual inductance between coils are defined as the amount of the magnetic flux density passing through the coil, and hence the mutual inductance is proportional to the winding number of transmitter and receiver coils. Therefore, the mutual inductance M_{01}' between L_0' and L_1' is expressed as follows utilizing original mutual inductance M_{01}:

$$M_{01}' = kmM_{01} \tag{3.43}$$

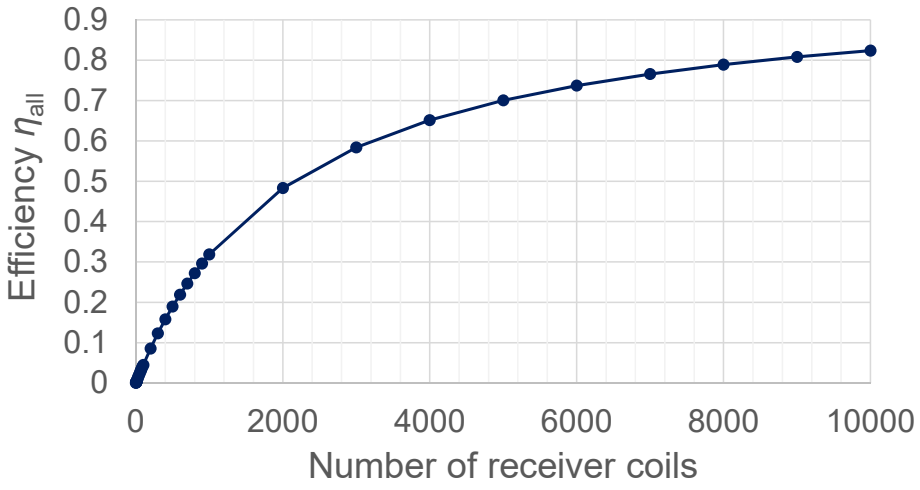

Figure 3.17: Result of the theoretical simulation based on Eq. (3.40) when the number of turns of both the transmitter and the receiver coil is set to 5 and R_0 is reduced to 10 Ω.

Eq. (3.43) leads to a fact that the coupling coefficient between the transmitter and the receiver coil is not increased even when the number of turns of coils are increased since the coupling coefficient k'_{01} is determined as Eq. (3.44).

$$k'_{01} = \frac{M'_{01}}{\sqrt{L'_0 L'_1}} = \frac{mkM_{01}}{\sqrt{m^2 L_0 k^2 L_1}} = \frac{M_{01}}{\sqrt{L_0 L_1}} = k_{01}. \tag{3.44}$$

Decreasing R_0 is difficult since the dominant factor determining R_0 is the wire resistance of the transmitter coil, while R_1 can be reduced by the circuit design since R_1 depends on the energy charging circuit in the receiver node. For instance, if the sensor node utilizes the capacitor for the energy tank, the series resistance of the circuit is determined mostly by the switch resistance of the MOSFET and hence can be reduced to several Ohms. Based on these discussion, the power efficiency of the 1-to-n WPT system is recalculated with Eq. (3.40) supposing the winding number of both the transmitter and receiver coil is increased to 5 and R_0 is reduced from 1 kΩ to 10 Ω. Fig. 3.17 shows the calculation result. Fig. 3.17 indicates that the power transmission efficiency can be enhanced to more than 80 % if the number of receiver coils is sufficiently large. In addition, Fig. 3.17 also indicates that the system can achieve the power transmission efficiency of more than 10 % even when the number of node is less than 400. From this result, we can say that the efficient 1-to-n WPT system is feasible and the power transmission efficiency of the system is significantly improved when the circuit constants are tuned appropriately.

3.3 Proposed WPT circuit structure for pervasive sensing

The previous section discussed the feasibility of the 1-to-n WPT system based on the circuit analysis. In addition to the feasibility focusing on circuit analysis, we need to discuss the circuit structure of the sensor nodes that can actually be used for pervasive sensing. Unlike other WPT applications, the sensor node for the pervasive sensing applications should be automatically switched to WPT mode when the inner node energy is running out since the sensor node for the pervasive sensing should be maintenance free. To address this issue, this section proposes the WPT sensor structure for maintenance free node for pervasive sensing. Fig. 3.18 shows the schematic of the proposed sensor node, and Figs. 3.19 and 3.20 show the prototype of the proposed sensor node. The prototype sensor node is implemented with discrete components, and the volume of the node is exactly 10mm $\times$ 10mm $\times$ 10mm. The sensor node is composed of two spiral coils and a circuit board as shown in Fig. 3.20. These two spiral coils correspond to L1 and L2 in Fig. 3.18, and they are shared by the functions of WPT and wireless communication. The function switching is enabled by the switch (SW) and Q2, which will be explained below.

3.3.1 WPT Mode

In WPT mode, Q2 is in ON state, and then L1 and L2 compose series-connected power receiving coils. Also, the bottom switch SW is OFF. In this case, the equivalent circuit of WPT mode becomes Fig. 3.21. When an alternating magnetic field is given to the coils, the electromagnetic induction phenomenon occurs, and energy can be obtained from “Signal A” and “Signal B” terminals in Fig. 3.18.

The sensor node for pervasive sensing operates using the stored energy obtained through WPT. Therefore, the node should be in WPT mode when there is no energy left in the node. Besides, MOSFETs are often used as a switch of, for example, Q2. However, MOSFET is a normally-off switching element that becomes on when a voltage is applied to the gate terminal, and hence the switch cannot be on when the inner node energy is running out. To solve this issue, the proposed circuit uses a normally-on JFET as Q2 in Fig. 3.18. The JFET has a feature that the channel between drain and source conducts when the applied voltage to the gate is 0V. When the node is out of energy, the voltage applied to Q2 vanishes and Q2 becomes ON state, and therefore the two coils L1 and L2 are connected to each other, and the node enters the WPT mode.

3.3.2 Wireless communication mode

When SW is closed in Fig. 3.18 and digital baseband voltage is applied to “BasebandSignal” terminal, the sensor node enters the wireless communication mode.

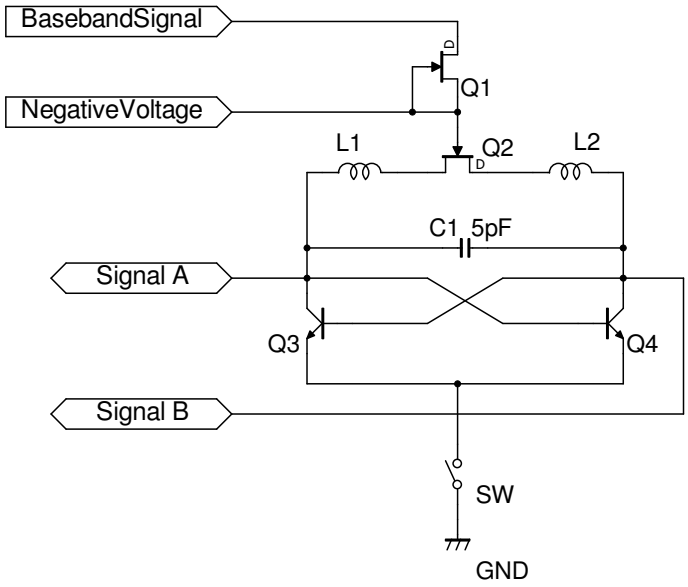

Figure 3.18: Proposed sensor node.

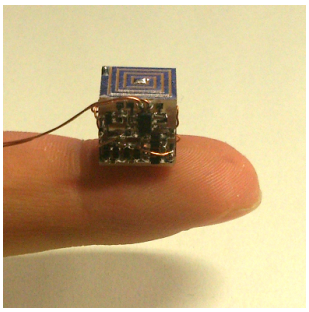

Figure 3.19: Prototype sensor node.

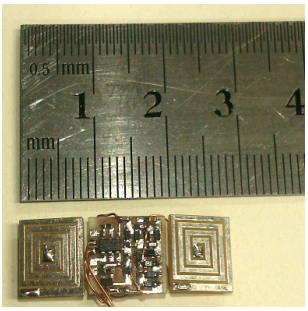

Figure 3.20: Expanded view of sensor node.

Fig. 3.22 shows an equivalent circuit in the communication mode. L1 and L2 are used as the coil of the LC oscillation circuit. Q1 in Fig. 3.22 acts as a constant current source

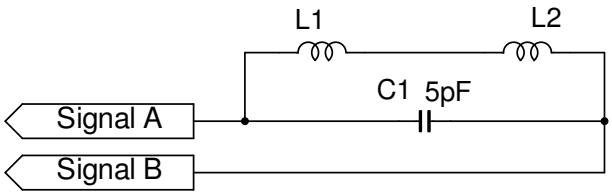

Figure 3.21: Equivalent circuit of WPT mode.

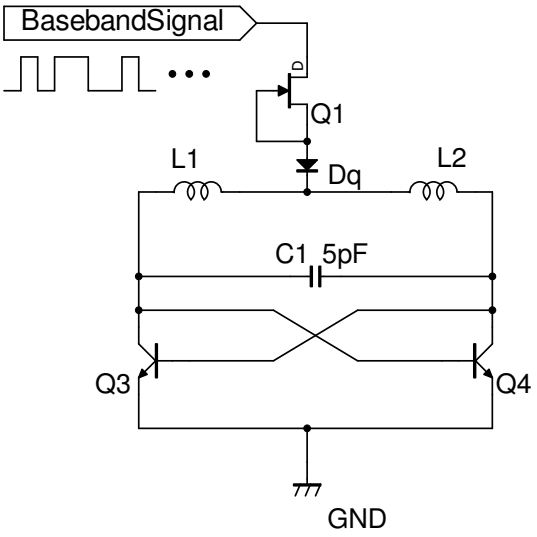

Figure 3.22: Equivalent circuit of communication mode.

and Q3 and Q4 behave as negative resistance elements. Therefore, Fig. 3.22 operates as a cross coupled LC oscillator, and the oscillation frequency is determined by L1, L2, C1 and the drain-source parasitic capacitance of Q2.

The proposed circuit uses the coils for radiation as well as oscillation as described in Chapter 2. The coils are exposed to the outside of the node as shown in Fig. 3.19, and hence the coil can emit electromagnetic waves in the wireless communication mode.

3.4 Evaluation

To validate the proposed structure, this section evaluates the performance of the sensor node in Figs. 3.19 and 3.20 prototyped with discrete components.

3.4.1 WPT mode

As described before, the sensor node should switch to WPT mode automatically when there is no energy left in the node. Therefore, it is necessary to confirm that the sen-

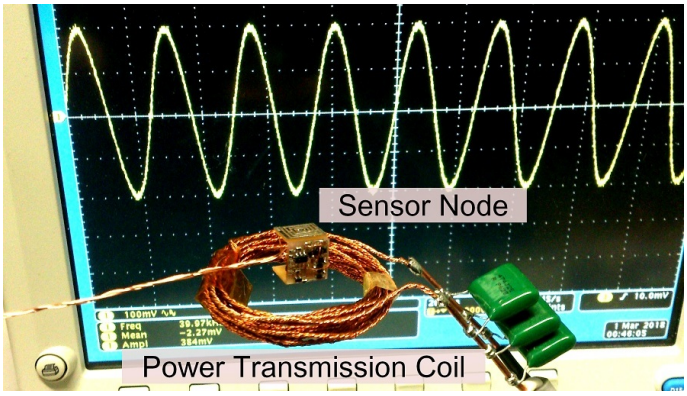

Figure 3.23: Experiment of wireless power supply.

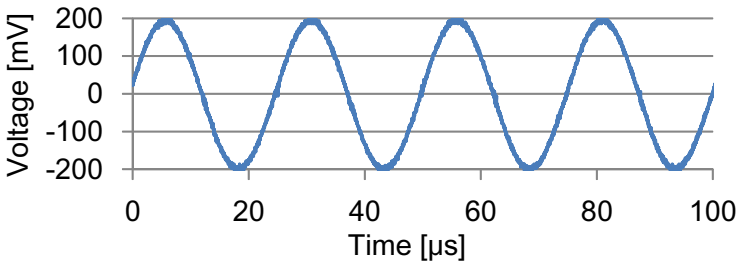

Figure 3.24: Output signal of sensor node.

sor node to which no voltages are given from the outside can correctly receive energy wirelessly.

Fig. 3.23 shows the positional relationship between the power transmitter coil and the sensor node. Here, the distance between the power transmitter coil and the center of the sensor node was fixed to 20 mm and the voltage between “Signal A” and “Signal B” terminals in Fig. 3.18 was evaluated with an oscilloscope whose input impedance was 1 MΩ. Fig. 3.24 shows the output voltage of the sensor node when a 60 Vp-p 40 kHz signal is applied to the power transmitter coil. We can see that the sensor node outputs a 400 mVp-p sine wave. This result confirms that Q2 in Fig. 3.18 automatically becomes on and the sensor node enters the wireless power supply mode when there is no power supply. The power consumed by the power transmitter coil was 6.5 W while the received power was 80 nW. Here, the observed power supply efficiency is very low. However, as described in previous sections, the power transmission efficiency of 1-to-n WPT system should be evaluated with the total power received by all the nodes. The hardware evaluation of 1-to-n WPT system is one of the future work.

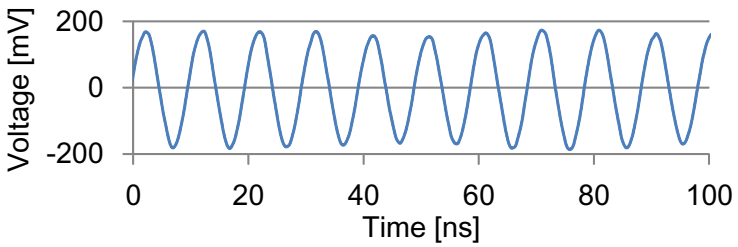

Figure 3.25: Measured output of wireless communication mode.

3.4.2 Wireless communication mode

To confirm that the sensor node can generate a carrier wave for wireless communication, SW in Fig.3.18 is closed and 3 V constant signal is applied to the "BasebandSignal" terminal. For minimizing the influence of measurement on the oscillation, a loop coil was located near the sensor node, and the oscillation signal was evaluated by measuring the voltage induced at the loop coil. The measured waveform in Fig. 3.25 indicates that the sensor node can generate a carrier wave with a frequency of 102 MHz. The structure of Fig. 3.18 can perform On-Off-Keying (OOK) modulation by inputting the baseband signal to the "BasebandSignal" terminal. A demodulation experiment was carried out as follows. A super heterodyne type receiver of Fig. 3.26 was installed 10cm away from the sensor node and a baseband signal with a communication speed of 1kbps was input to the sensor node.

The receiver performs frequency conversion, intermediate frequency amplification, and then demodulates the signal using a rectifier circuit and a comparator circuit. The measurement results in Fig. 3.27 show that the symbol string consisting of 1 and 0 can be correctly demodulated, which clarifies the capability of wireless communication. Besides, when the node is communicating at 1 kbps, the energy consumption per bit is 2.1 μJ/b. This large energy consumption is due to the low communication speed and energy loss at Q1 and Q2. Even when a voltage of 3V is applied to the sensor node, the potential at the drain and source of Q2 is only 500 mV. A voltage drop of 2.5 V arises in Q1 and Q2, and consequently, 5/6 of the energy is lost. Minimizing the energy loss at these components is one of the future work.

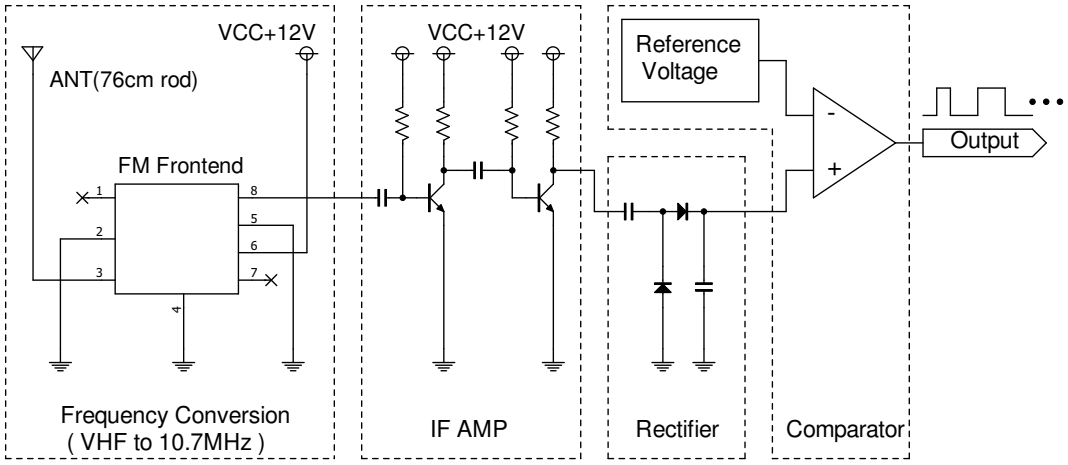

Figure 3.26: Schematic of receiver.

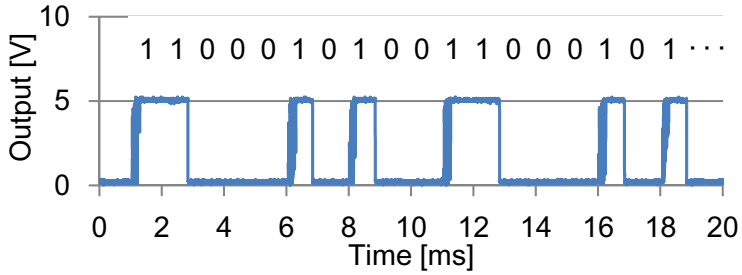

Figure 3.27: Waveform at receiver in case of 1kbps communication.

3.5 Conclusion

This chapter analyzed the S-S type WPT circuit and the magnetic field based on the theory of circuit and magnetics, and showed that the 1-to-n WPT system with tiny sensor nodes is feasible. The theoretical analysis revealed that the sensor nodes of pervasive sensing application can receive sufficient power although the coupling coefficient is very low and close to 0. Based on the circuit analysis, this chapter introduced that the frequency where the power transmission efficiency and the received power are maximized is fixed to the resonant frequency of the LC circuit and does not depend on the positional relationship between the power transmitter coil and sensor nodes. For this reason, we do not have to tune the circuit constants depending on sensor nodes, which greatly facilitates building the sensor node for pervasive sensing.

In addition, this chapter proposed a sensor node structure in which the functions of WPT and wireless communication shared two coils through switching the coil connection. Adopting JFET as the switching element enables to connect two coils even when the node is out of energy, realizing a structure that automatically switches to the WPT mode. These coils can be also used as an oscillation coil and radiation antenna

during wireless communication mode. The prototype measurement shows that 1 kbps communication is possible at a distance of 10 cm.

The primary future work on 1-to-n WPT system is to verify the correlation between the simulation result in this chapter and hardware measurement with the numerous number of prototyped sensor nodes. This chapter confirmed the feasibility of the 1-to-n WPT system based on the simulation, on the other hand, the experiment with the prototyped sensor node is currently limited to 1-to-1 WPT. Therefore, the experiment with the large number of sensor nodes should be conducted. Also, analyzing and evaluating the S-P type WPT circuit and comparing the result with the S-S type WPT are important future work.

Chapter 4

DC magnetic field based 3D localization with single anchor coil

In pervasive sensing applications, the value of information elevates significantly when it is associated with the location information. For this reason, the pervasive sensing system should be able to localize the tiny sensor nodes. This chapter proposes and evaluates a DC magnetic field based localization method only requiring single anchor coil. The proposed localization method aims to be applicable both for tabletop-scale, which require less than cm-class accuracy, and room-scale, which require the localizable distance of several meters.

4.1 Introduction

As explained in Section 1.3.3, there are two mainstreams in the research context of the localization: outdoor localization and indoor localization. For outdoor localization, required localizable distance is several dozens of meters to even several kilometers while required localization accuracy is around 1 to several meters. Currently, GPS-based positioning system is promising method for outdoor localization since it can provide the localization anywhere on the earth with the accuracy of less than several meters. On the other hand, indoor localization has the difficulty since the required localization accuracy is less than 1 meter or even cm-class unlike outdoor localization. In addition to this, the installation cost of the indoor localization system should be minimized since the available area is highly limited compared to outdoor localization. Although conventional camera-based localization methods can achieve high accuracy, they suffer from occlusion and privacy problems. To address these issue, magnetic field based localization is actively studied. However, currently available magnetic field based localization methods are weak to the non-ferrous metallic material, which is generally contained in our daily object, and have installation cost problem since they require multiple anchor coils. To solve these issue, this chapter proposes a DC magnetic field based 3D local-

ization method with single anchor coil. The proposed localization method can achieve less than 15 cm localization error in room scale and can achieve even less than 1 cm accuracy on the tabletop.

The rest of this section is organized as follows. First, Section 4.2 analyzes the characteristic of the DC magnetic field generated by the coil. Then based on the findings reported in Section 4.2, Section 4.3 proposes the localization method with single anchor coil. Section 4.4 evaluates the proposed localization method and shows the method can achieve high accuracy with single anchor coil and can tolerate non-ferrous metallic material. Section 4.5 discusses the detail about the proposed method including the coverage expansion with the multiple anchor coil. Finally, the conclusion of this chapter is given in Section 4.6.

4.2 Analysis of DC magnetic field

This section analyzes artificially generated DC magnetic field with a numerical integration simulator. Section 4.2.1 analyzes a single loop coil and Section 4.2.2 analyzes a general solenoid whose number of turns is more than one. The objective of this section is to illustrate the existence of a relationship between the position of the sensor node and magnetic field, which will be exploited by the proposed localization method in the next section.

4.2.1 Analysis of a single loop coil

First, this section analyzes the single loop coil placed on the *xy* plane in Fig. 4.1. In this figure, magnetic flux density vector $\mathbf{B}(r,\theta,\phi)$ generated at point $P(r,\theta,\phi)$ is given by the following equation [44]:

$$\mathbf{B} = \nabla \times \mathbf{e}_\phi \frac{\mu_0 I b}{2\pi} \int_{-\frac{\pi}{2}}^{\frac{\pi}{2}} \frac{\sin\phi'}{\sqrt{r^2+b^2-2br\sin\theta\sin\phi'}} d\phi', \tag{4.1}$$

where $\mathbf{e}_\phi$ is a unit vector of the ϕ direction, ϕ' is an integral parameter, and μ_0 is a magnetic constant. We can obtain the intensity and direction of the magnetic field by solving Eq. (4.1) with a numerical integration simulator. Here, the direction of the magnetic field is represented by ξ, and it is defined in Fig. 4.2.

Figs. 4.3 and 4.4 show the magnitude and direction of the magnetic field at each point on the *yz* plane, respectively, where these results are obtained by numerically integrating Eq. (4.1) with $b = 1$ [mm] and $I = 1$ [A]. Note that when ϕ is $\pi/2$ and point P is distant enough from the coil, *x*-direction component of the magnetic field is zero [44]. In Fig. 4.3, the intensity of the magnetic field at the points near the coil, which correspond to the white rectangle, is not plotted since it is too strong and it deteriorates the visibility of the heat map.

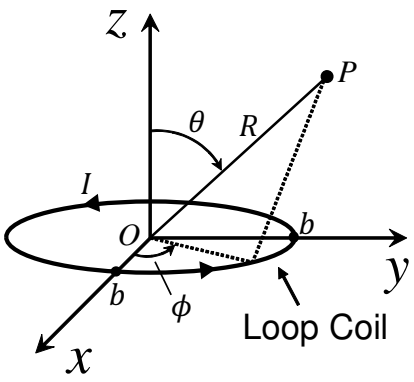

Figure 4.1: Coordinate setting.

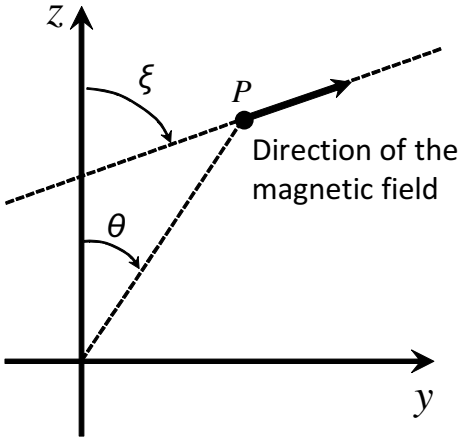

Figure 4.2: Definition of ξ.

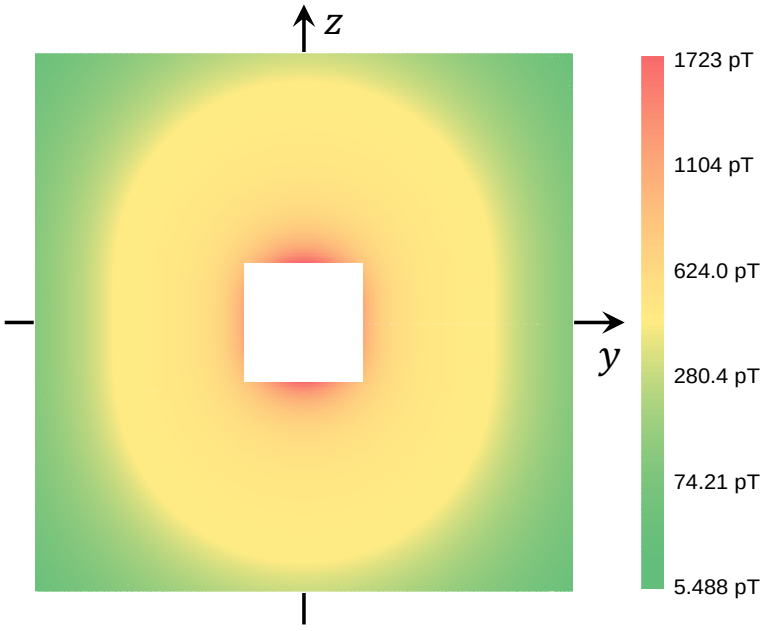

Figure 4.3: Obtained heatmap of the magnitude of magnetic field ($b = 1$[mm] and $I = 1$[A]). The intensity inside the white rectangle is omitted due to visibility reason.

Fig. 4.3 suggests a simple geometric relationship between the position of point P and the magnitude of the magnetic field at P. Fig. 4.4 shows that the values of ξ on the radial line, i.e. at the points having the same θ, are almost the same. This relation will be derived in detail and exploited for localization in Section 4.3.

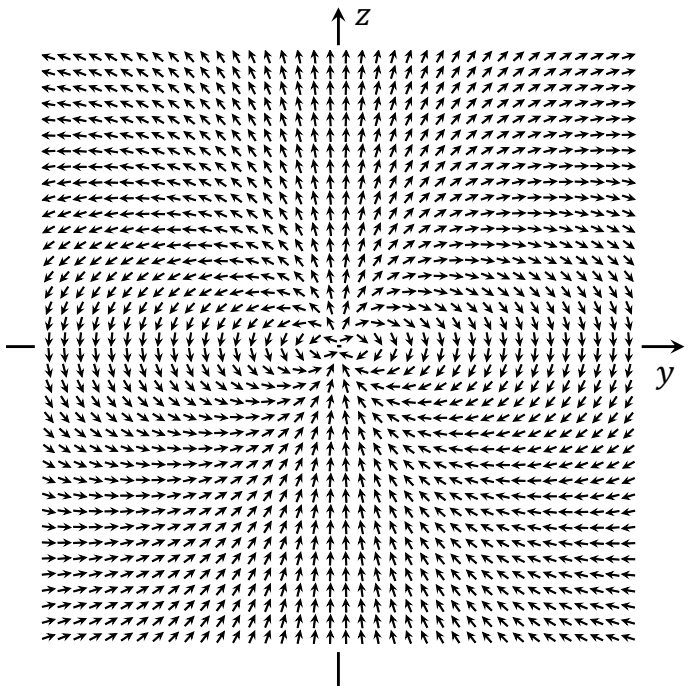

Figure 4.4: Direction of magnetic field ($b = 1$[mm] and $I = 1$[A]).

4.2.2 Analysis of a solenoid

Next, this section analyzes the magnetic field generated by a normal solenoid whose number of turns is more than one. Basically, magnetic field generated by a solenoid can be calculated by superposing the analysis results for a single loop coil. The coil to be analyzed has almost the same specification as the coil which will be used in the experiment, and its size is $\phi 42$ mm $\times$ 30 mm and the number of turns is 240. Figs. 4.3 and 4.4 show the results of the numerical simulation supposing 1A current was injected to the coil, and they indicate that the magnetic field generated by the solenoid has the same tendency as the field generated by the single loop coil.

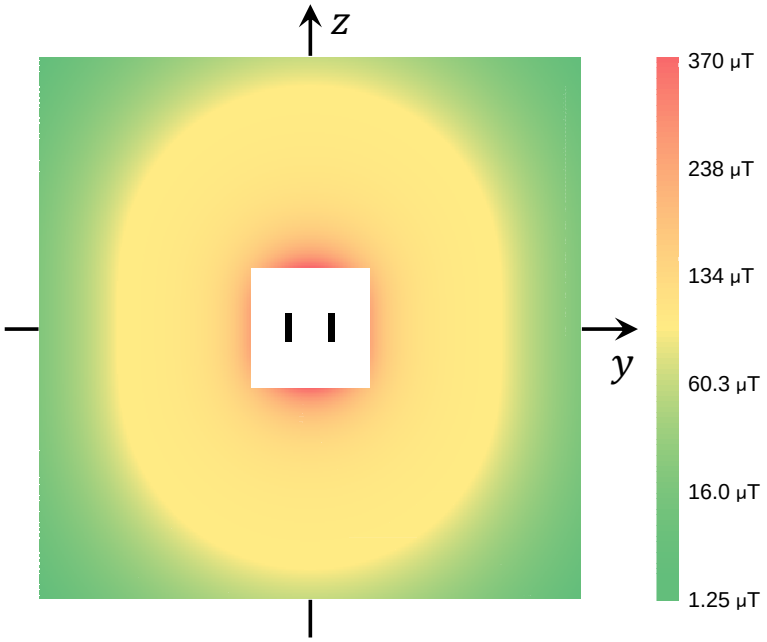

Figure 4.5: Obtained heatmap of the magnitude of magnetic field generated by the solenoid ($I = 1$[A]). The intensity inside the white rectangle is omitted due to visibility reason.

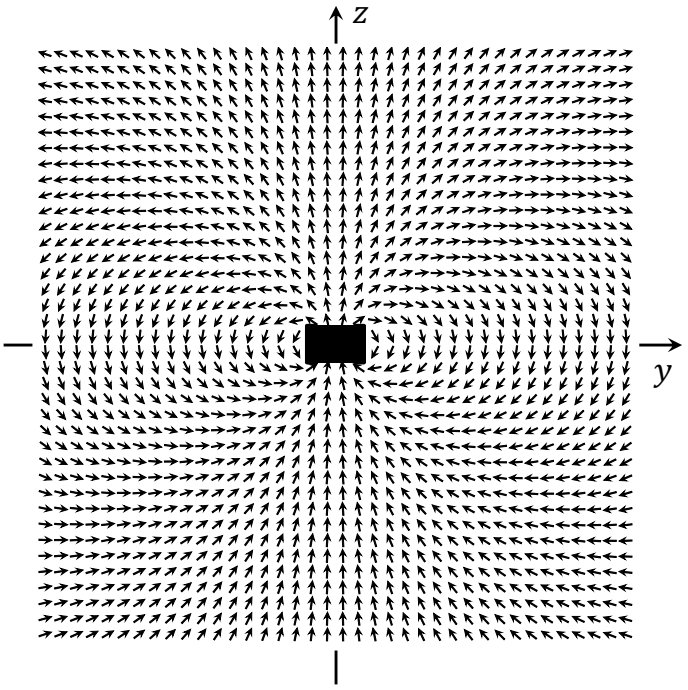

Figure 4.6: The plot of the direction of the magnetic field generated by the solenoid ($I = 1$[A]).

4.3 Proposed localization method

This section proposes a 3D localization method that can estimate the sensor position utilizing a single anchor coil. Figs. 4.7 and 4.8 show the structure of the sensor node and the anchor node supposed in the proposed method, respectively. Both the sensor node and the anchor node are equipped with a geomagnetic sensor that can sense weak DC magnetic field. The anchor node also includes a constant current source and anchor coil.

Figs. 4.9 and 4.10 show the coordinate setting and definition of $s, t, u, t', \lambda (\pi/2 \leq \lambda \leq \pi/2)$, and $\theta (0 \leq \theta \leq \pi/2)$. In Fig. 4.9, yz plane is parallel to the ground and x axis represents the height of the system. The anchor node is installed at the origin $O(0,0,0)$ and the sensor node locates at point $P(s,t,u)$. Fig. 4.9 shows y' axis in addition to the xyz coordinate system. $y'z$ plane includes a sensor node P, and λ denotes the angle between y' and y axis. $P'(0,t',u)$ is a point on the yz plane, and it is obtained by rotating the point P by λ [rad] around the z axis. Supposing t' is the y'-axis value of the point P, the following relationship is satisfied:

$$\overrightarrow{OP} = s\mathbf{e}_x + t\mathbf{e}_y + u\mathbf{e}_z = t'\mathbf{e}'_y + u\mathbf{e}_z, \tag{4.2}$$

where $\mathbf{e}_x, \mathbf{e}_y, \mathbf{e}_z$ and $\mathbf{e}'_y$ are unit vectors of x, y, z, and y' axis directions, respectively. θ in Fig. 4.10 represents the angle between line OP and y' axis, and it is equal to the angle between line OP' and y axis. The coordinates of points U and H are $U(0,0,u)$ and $H(0,t,u)$, respectively.

Section 4.3.1 briefly explains the overview of the proposed localization method, and following sections from 4.3.2 to 4.3.5 focus on the detail of each localization step.

4.3.1 Overview

The proposed localization method estimates the three-dimensional position of sensor node P with the following four steps: posture estimation, altitude estimation, distance estimation, and angle estimation. This section, first, explains each step briefly before going into the details.

Fig. 4.11 illustrates two important coordinate systems utilized in the localization system. The sensor node is equipped with the tiny geomagnetic sensor and its coordinate system is depicted as $x''y''z''$ coordinate system. xyz coordinate system is the absolute coordinate system that is directly used for localization, i.e., the location in this coordinate system must be returned, and hence the data obtained by the sensor node should be based on this coordinate system. However, the magnetic field data observed by the sensor node are based on $x''y''z''$ coordinate system. Therefore, we have to perform coordinate transformation, and for this reason, we need to know the posture of the sensor node. In the posture estimation step, the sensor node estimates its facing direction by observing the geomagnetism and carries out the coordinate transformation of the measured data.

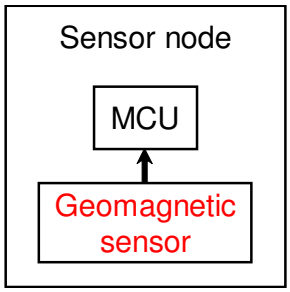

Figure 4.7: Structure of the sensor node.

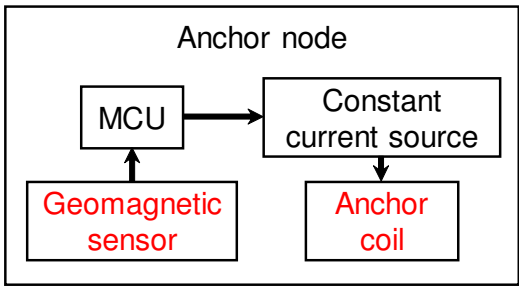

Figure 4.8: Structure of the anchor node.

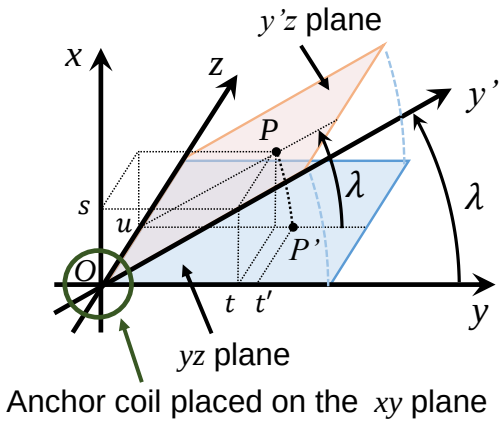

Figure 4.9: Coordinate setting and definition of s, t, u, t' and λ.

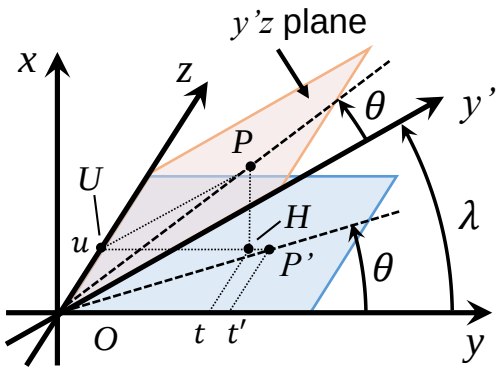

Figure 4.10: Definition of θ.

The position of P can be obtained by rotating P' by λ in Fig. 4.11 once λ and P' are obtained. Therefore, the remaining steps calculate λ and P'. The second altitude estimation step derives the value of λ. As discussed in Section 4.2, the $x-$direction component of the magnetic field is zero. In addition to this, the magnetic field generated by the anchor coil is axially symmetrical to the z axis as shown in Fig. 4.11. By utilizing these two features, the system can derive the value of λ. Finally, the following two steps localize P'. The third distance estimation step estimates the distance between the anchor coil and point P' and calculates a contour line shown in Fig. 4.12. The final angle estimation step estimates the anchor-to-P' angle, and calculates an anchor-to-P' line as shown in Fig. 4.12. Using the anchor-to-P' distance and anchor-to-P' angle, P' is localized.

After the four steps, λ and the position of P' are available, and consequently P can be obtained. Following sections from 4.3.2 to 4.3.5 detail each step.

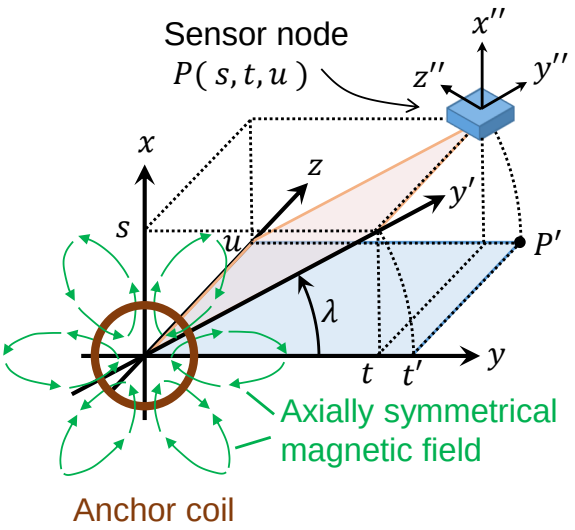

Figure 4.11: xyz coordinate system is the absolute coordinate system and $xy'z$ coordinate system is utilized to calculate λ. The anchor coil placed on the origin is axially symmetric and hence the generated magnetic field is also axially symmetric. Therefore, we can estimate the magnetic field at the point P' from the magnetic field at point P.

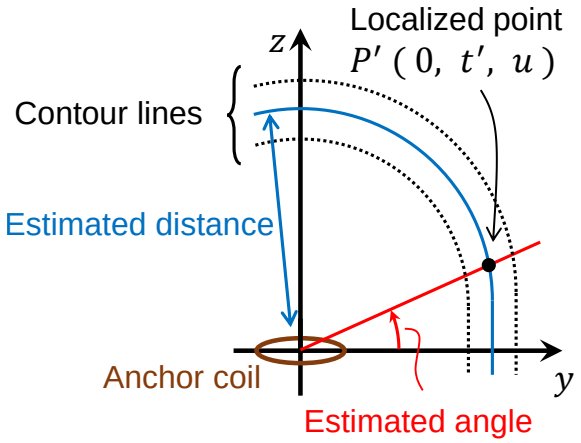

Figure 4.12: Distance estimation and angle estimation step estimate the position of the point P' rather than the sensor node. These steps are conducted on yz plane. Each step draws the contour line and angle line according to the intensity and the direction of the magnetic field respectively, and then derive the position of P' by calculating the intercept point of those.

4.3.2 Posture estimation

First, the proposed localization system estimates the posture of the sensor node P before starting position estimation. The posture of the sensor node P is estimated by the

geomagnetism, which is the most common uniform magnetic field.

The posture of the sensor node is determined by the tilt angle and the horizontal rotation angle of the sensor node. In some indoor applications, the tilt angle is fixed since the objects with the sensor node are not placed arbitrarily. If it is not fixed, we measure the direction of the gravity with an acceleration sensor and estimate the tilt angle. The horizontal rotation angle is estimated with the direction of the geomagnetism. The following explains the estimation of the horizontal rotation angle.

Fig. 4.13 shows the definition of ψ, which corresponds to horizontal rotation angle. Fig. 4.13 also includes the coordinate system of the geomagnetic sensor embedded in the sensor node P, and it is defined by x'', y'', and z''. We regard as $y''z''$ plane is parallel to yz plane since the tilt angle of the sensor node is known and supposed to be already compensated. With this feature, as shown in Fig. 4.13, the coordinate system of the sensor node, i.e. $x''y''z''$ coordinate system, is rotated by ψ[rad] around the x axis from the coordinate system of the anchor node, i.e. xyz coordinate system. Letting $\mathbf{B}_g$ denote the geomagnetism vector, the output of the geomagnetic sensor ($\mathbf{B}_{Pg} = (B_{Pgx''}, B_{Pgy''}, B_{Pgz''})$) in sensor node P satisfies the following equation.

$$\mathbf{B}_g = B_{Pgx''}\mathbf{e}''_x + B_{Pgy''}\mathbf{e}''_y + B_{Pgz''}\mathbf{e}''_z \tag{4.3}$$

where $\mathbf{e}''_x, \mathbf{e}''_y$, and $\mathbf{e}''_z$ are the unit vectors of x'', y'', and z'' axis directions, respectively. The geomagnetic vector is constant regardless of the observation location. Therefore, $\mathbf{B}_g$ can be also expressed as Eq.(4.4) using the output of the geomagnetic sensor ($\mathbf{B}_{Og} = (B_{Ogx}, B_{Ogy}, B_{Ogz})$) in the anchor node O.

$$\mathbf{B}_g = B_{Ogx}\mathbf{e}_x + B_{Ogy}\mathbf{e}_y + B_{Ogz}\mathbf{e}_z \tag{4.4}$$

Here, to simplify the discussion, let us assume that y direction component of the geomagnetism is zero, which means B_{Ogy} is zero. Note that, on the other hand, this assumption is introduced only for simplifying the discussion, and the other situations can be discussed similarly. If we rotate vector $\mathbf{B}_{Pg}$ by $-\psi$[rad], it should match with vector $\mathbf{B}_{Og}$ since the geomagnetism can be regarded as almost equal at the locations of the anchor node and the sensor node. Therefore, we can obtain Eq.(4.5).

$$\begin{aligned}
\begin{bmatrix} B_{Ogx} \\ 0 \\ B_{Ogz} \end{bmatrix} &= \begin{bmatrix} 1 & 0 & 0 \\ 0 & \cos -\psi & -\sin -\psi \\ 0 & \sin -\psi & \cos -\psi \end{bmatrix} \mathbf{B}_{Pg} \\
&= \begin{bmatrix} B_{Pgx''} \\ B_{Pgy''}\cos\psi + B_{Sz}\sin\psi \\ -B_{Pgy''}\sin\psi + B_{Sz}\cos\psi \end{bmatrix}
\end{aligned} \tag{4.5}$$

From Eq. (4.5), we can obtain the relationship between ψ and $\mathbf{B}_{Pg}$ below.

$$\tan\psi = -\frac{B_{Pgz''}}{B_{Pgy''}} \tag{4.6}$$

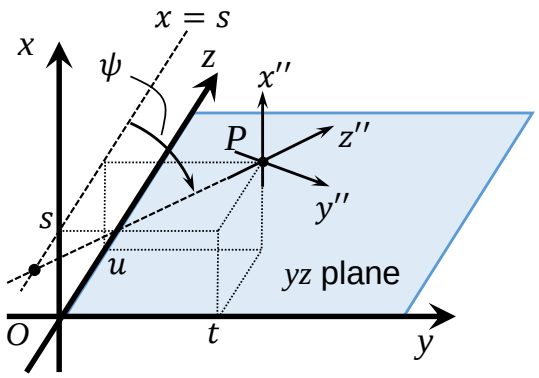

Figure 4.13: The posture of the sensor node P.

Taking into account the range of $\tan^{-1}\left(-\frac{B_{Pgz''}}{B_{Pgy''}}\right)$ being limited to $-\pi/2 \leq \tan^{-1}\left(-\frac{B_{Pgz''}}{B_{Pgy''}}\right)\psi \leq \pi/2$, ψ is calculated as follows.

$$\psi = \begin{cases} \tan^{-1}\left(-\frac{B_{Pgz''}}{B_{Pgy''}}\right) & \text{if } B_{Pgz''} \geq 0, \\ \pi + \tan^{-1}\left(-\frac{B_{Pgz''}}{B_{Pgy''}}\right) & \text{otherwise.} \end{cases} \tag{4.7}$$

4.3.3 Altitude estimation

This step first estimates λ to calculate s, which is the altitude of the sensor node P. Estimating λ requires the artificially generated magnetic field, and therefore the system gives a constant current to the anchor coil. Here, we assume the output of the geomagnetic sensor mounted in the sensor node P is $\mathbf{B}_{P''e} = (B_{Pex''}, B_{Pey''}, B_{Pez''})$. To obtain the magnetic field vector generated by the anchor coil $\mathbf{B}_{P''}$, we subtract the geomagnetism $\mathbf{B}_{Pg}$ from $\mathbf{B}_{P''e}$ since $\mathbf{B}_{P''e}$ contains not only artificially generated magnetic field but also the geomagnetism.

$$\mathbf{B}_{P''} = \mathbf{B}_{P''e} - \mathbf{B}_{Pg} \tag{4.8}$$

We perform coordinate transformation using the obtained ψ and the rotation matrix since the coordinate system of $\mathbf{B}_{P''} = (B_{Px''}, B_{Py''}, B_{Pz''})$ is based on $x''y''z''$ coordinate system. $\mathbf{B}_P = (B_{Px}, B_{Py}, B_{Pz})$, which is based on xyz coordinate system after the transformation, can be expressed by Eq. (4.9).

$$\mathbf{B}_P = \begin{bmatrix} 1 & 0 & 0 \\ 0 & \cos -\psi & -\sin -\psi \\ 0 & \sin -\psi & \cos -\psi \end{bmatrix} \mathbf{B}_{P''} \tag{4.9}$$

The magnetic field generated by the anchor coil is axially symmetric around z axis since the anchor coil is placed at the origin on the xy plane and the central axis of the coil

exactly accords with the z axis as illustrated in Fig. 4.11. Therefore, when we observe the magnetic field at the point P', $\mathbf{B}_{P'} = B_{P'x}\mathbf{e}_x + B_{P'y}\mathbf{e}_y + B_{P'z}\mathbf{e}_z$, $\mathbf{B}_{P'}$ can be calculated by rotating $\mathbf{B}_P$ by λ [rad].

$$\mathbf{B}_{P'} = \begin{bmatrix} \cos\lambda & -\sin\lambda & 0 \\ \sin\lambda & \cos\lambda & 0 \\ 0 & 0 & 1 \end{bmatrix} \mathbf{B}_P \tag{4.10}$$

As we discussed in the previous section, the x component of $\mathbf{B}_{P'}$ is zero since the point P' is on the yz plane.

$$\mathbf{B}_{P'} = \begin{bmatrix} 0 \\ B_{P'y} \\ B_{P'z} \end{bmatrix} \tag{4.11}$$

From Eqs. (4.10) and (4.11), Eq. (4.12) holds.

$$\begin{bmatrix} 0 \\ B_{P'y} \\ B_{P'z} \end{bmatrix} = \begin{bmatrix} B_{Px}\cos\lambda - B_{Py}\sin\lambda \\ B_{Px}\sin\lambda + B_{Py}\cos\lambda \\ B_{Pz} \end{bmatrix} \tag{4.12}$$

Then, we can derive λ from Eq. (4.12) as follows.

$$\lambda = \tan^{-1}\left(\frac{B_{Px}}{B_{Py}}\right) \tag{4.13}$$

Next, we calculate the altitude of the sensor node P, s, using λ. Focusing on $\triangle PUH$ in Fig. 4.10, the following relationship between s and λ is satisfied.

$$\sin\lambda = \frac{PH}{PU} = \frac{PH}{P'U} = \frac{s}{t'} \tag{4.14}$$

By arranging Eq. (4.14), we finally obtain s.

$$s = t'\sin\lambda \tag{4.15}$$

On the other hand, variable t' included in Eq. (4.15) is still unknown, and it will be calculated in the following steps.

4.3.4 Distance estimation

We can estimate the position of the sensor node P by estimating the coordinate of point P' since the position of sensor node P can be obtained by rotating point P' by $-\lambda$ [rad] around the z axis. Therefore, the objective of the remaining two steps is to find the coordinate of point P'. In this step, we estimate the anchor-sensor distance from the magnitude of magnetic field generated by the anchor coil.

We can calculate the magnitude of the magnetic field using Eq. (4.16) since the generated magnetic field is axially symmetric around the z axis as shown in Fig. 4.11, and the magnitude at the point P' should be the same as that of at the sensor node P.

$$|\mathbf{B}_{P'}| = |\mathbf{B}_P| = \sqrt{{B_{Px}}^2 + {B_{Py}}^2 + {B_{Pz}}^2} \tag{4.16}$$

Fig. 4.5, which was introduced in Section 4.2, shows the relationship between the position of the sensor node and the magnitude of the artificially generated magnetic field. Fig. 4.14 shows the corresponding contour map, where the contour lines go through $(0,0,25)$, $(0,0,50)$, $(0,0,100)$, $(0,0,150)$, $(0,0,200)$ or $(0,0,250)$. We can see that the contour line l that goes through point $(y,z) = (r_0,0)$, where $r_0 > 0$, always passes the vicinity of point $(y,z) = (0,5r_0/4)$ if r_0 is larger than 20 mm. Fig. 4.14 also indicates that the contour line l can be regarded as a straight line in the range of $0 \leq z \leq r_0/4$ and it can be approximated by the equation of a circle in the range of $z > r_0/4$. Therefore, this work approximates contour line l with Eq. (4.17).

$$l : \begin{cases} y = r_0 & 0 \leq z \leq \frac{r_0}{4} \\ y^2 + \left(z - \frac{1}{4}r_0\right)^2 = r_0^2 & z > \frac{r_0}{4} \end{cases} \tag{4.17}$$

The error introduced by this approximation will be discussed in Section 4.5.1. Eq. (4.17) shows that, for any point on yz plane, we can find the point on y axis where the magnitude of the magnetic field is the same. Hence, if we have the relationship between the r_0, which is the y coordinate of the point Y on y axis, and the magnitude of the magnetic field at the point Y, we can estimate the magnitude at any point on yz plane.

Fig. 4.15 shows the relationship between r_0 and the magnitude, which is obtained by numerical simulation. Fig. 4.15 indicates that the magnitude of the magnetic field is proportional to r_0^{-3}. The inverse function of the equation in Fig. 4.15 is

$$r_0 = 261.3439338\ |\mathbf{B}_{P'}|^{-0.332140362}. \tag{4.18}$$

Let me summarize this step. Now, given $\mathbf{B}_{P'}$, we can obtain the equation of contour line l that goes through point $P'(0,t',u)$ with Eqs. (4.16), (4.17), and (4.18), and consequently anchor-sensor distance estimation is done. The next final step identifies the location on the contour line.

4.3.5 Angle estimation

This step estimates the anchor-node angle θ and find the exact position of P' on contour line l. We can express the magnetic field ($\mathbf{B}_{P'}$) at the point P' with $\mathbf{B}_P$ using Eq. (4.12).

$$\mathbf{B}_{P'} = \begin{bmatrix} 0 \\ B_{Px}\sin\lambda + B_{Py}\cos\lambda \\ B_{Pz} \end{bmatrix} \tag{4.19}$$

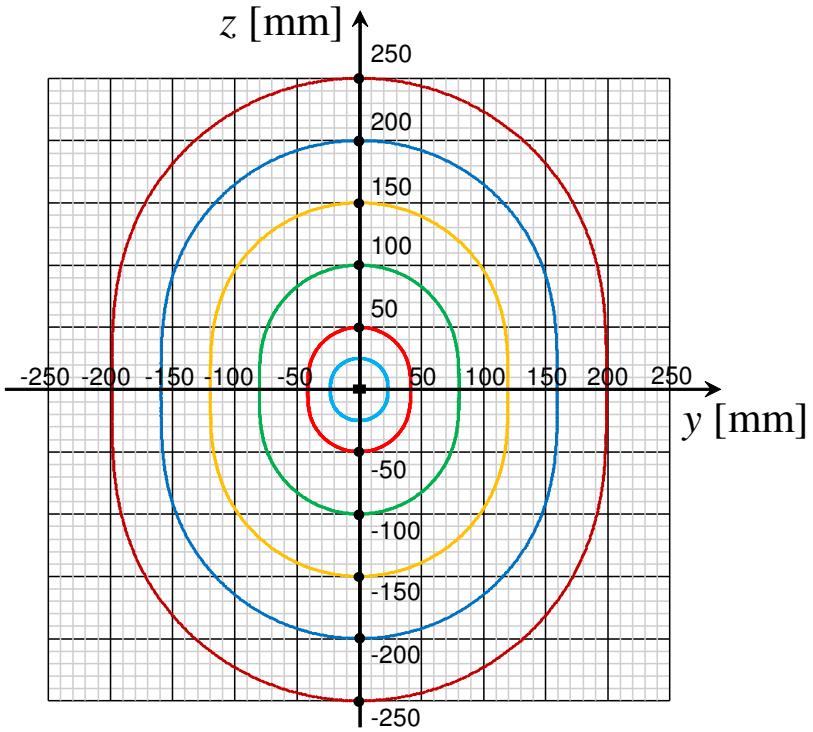

Figure 4.14: Contour lines of the magnitude of magnetic field on yz plane.

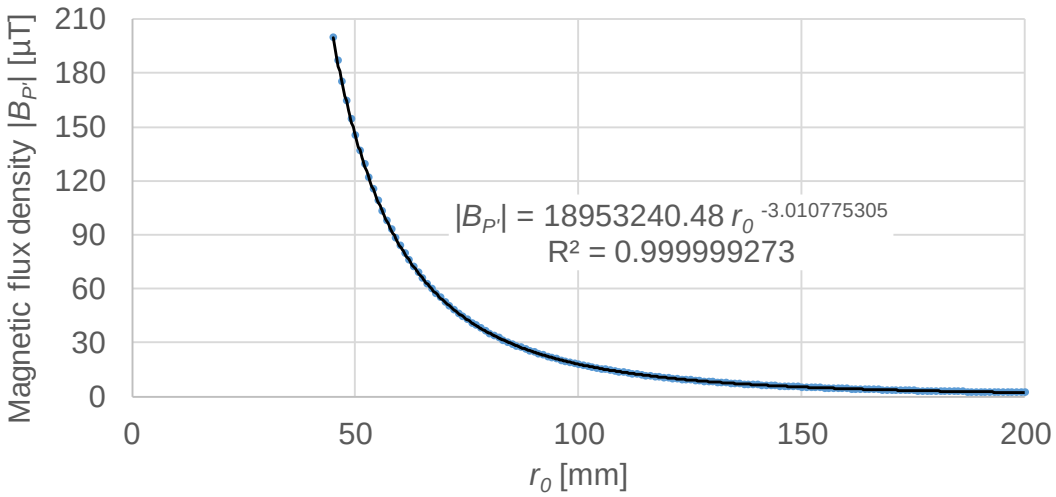

Figure 4.15: Relationship between $|\mathbf{B}_{P'}|$ and r_0.

We want to know ξ in Fig. 4.2 for the localization, and it is expressed by

$$\begin{aligned}\xi &= \frac{\pi}{2} - \tan^{-1}\frac{B_{P'z}}{B_{P'y}} \\ &= \frac{\pi}{2} - \tan^{-1}\left(\frac{B_{Pz}}{B_{Px}\sin\lambda + B_{Py}\cos\lambda}\right).\end{aligned} \tag{4.20}$$

Fig. 4.6 suggests the existence of the simple equation between ξ and θ. Fig. 4.16, which is calculated with numerical simulation, shows the relationship between θ and ξ indicating that ξ can be approximated by a cubic polynomial expression of θ. The inverse function of the equation in Fig. 4.16 becomes

$$\theta = -0.0008861\xi^3 - 0.06755\xi^2 + 0.7200\xi - 0.007633. \tag{4.21}$$

We can estimate the anchor-sensor angle θ using Eqs. (4.20) and (4.21). We can also obtain the equation of the straight line m that contains point P' with the obtained θ.

$$m: \ z = \tan\left(\frac{\pi}{2} - \theta\right) y \tag{4.22}$$

Both contour line l and straight line m should contain point P', and hence we can derive the coordinate of point $P'(0,t',u)$ just by calculating the intersection of the two lines as depicted in Fig. 4.12. The obtained u is z coordinate of not only the point P' but also the sensor node P. The obtained t' is used to estimate t, which is the y coordinate of the sensor node P, in the following procedure. We obtain the relationship among t, t' and λ focusing on $\triangle PUH$ in Fig. 4.10.

$$\cos\lambda = \frac{UH}{PU} = \frac{UH}{P'U} = \frac{t}{t'} \tag{4.23}$$

We obtain the relationship between t and t' by transforming Eq. (4.23) and can estimate the y coordinate of sensor node P.

$$t = t'\cos\lambda \tag{4.24}$$

Now, we successfully estimate the position of the sensor node $P(s,t,u)$ through the four steps: posture estimation, altitude estimation, distance estimation, and angle estimation. Here, we need to set a constraint on the localizable angle since the directions of magnetic field at two points which are located point-symmetric to the center of the coil are identical and hence they cannot be distinguished. This work calls this unlocalizable area as dead-zone where the angle estimation step cannot work correctly. However, this dead-zone is not a serious problem in terms of the localization since we can minimize the effect of this dead-zone by choosing the anchor position carefully. The localizable angle can be any consecutive 180 degree in the range of 360 degree around the anchor coil. In other words, users can choose the localizable angle as they want, which contributes to a high degree of freedom in the installation direction of the anchor node and mitigates the effect of the dead-zone. Even when the situation that the coverage area is too small due to this dead-zone, we can expand the coverage area by introducing multiple anchor coils as will be discussed in Section 4.5.4.

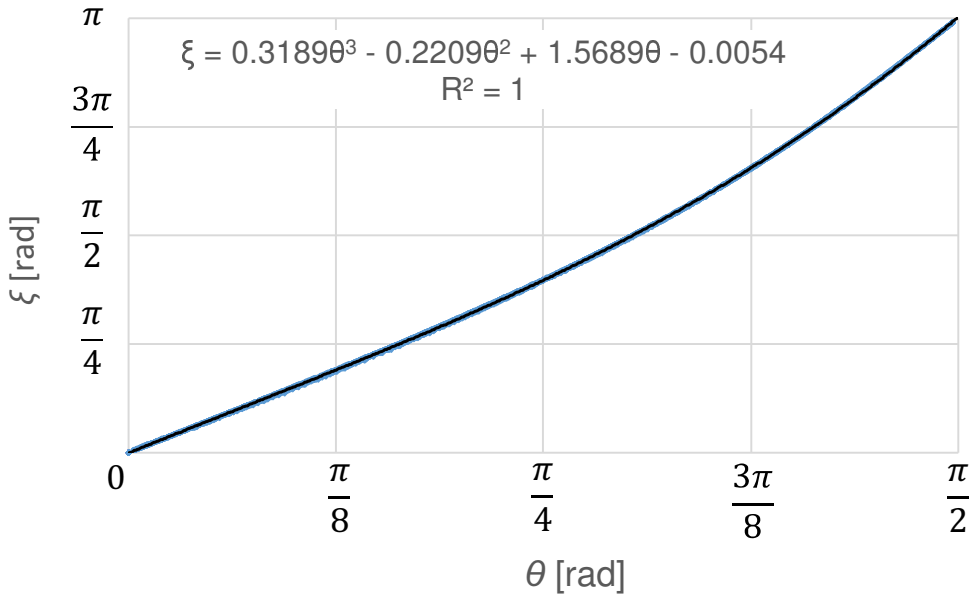

Figure 4.16: Relationship between θ and ξ.

4.4 Evaluation

This section presents measurement results obtained with a prototyped system to validate the proposed localization method. Section 4.4.1 introduces experimental conditions and environment. Section 4.4.2 measures the geomagnetism with a geomagnetic sensor and show the performance of the direction estimation based on the geomagnetism only. Next, Section 4.4.3 evaluates the artificially generated DC magnetic field with the geomagnetic sensor and verify the correlation between simulation and measurement results. Section 4.4.4 shows 3D localization results with the proposed localization method using prototyped sensor and anchor nodes, and Section 4.4.5 experimentally demonstrates the proposed method is not sensitive to non-ferrous metal.

4.4.1 Setup

Fig. 4.17 explains the experimental environment, and Fig. 4.18 shows the photo of the actual environment. An anchor coil is fixed at the origin of the coordinate system as shown in Fig. 4.17. The size of the anchor coil is ϕ42 mm$\times$30 mm and the number of turns is 243. The outputs of a geomagnetic sensor (LIS3MDL), which is fixed to a 2D plotter in Fig. 4.18, is evaluated. The installed 2D plotter is responsible for positioning the geomagnetic sensor. The position of the geomagnetic sensor can be configured in the yz plane in Fig. 4.9 by sending specific commands to the 2D plotter.

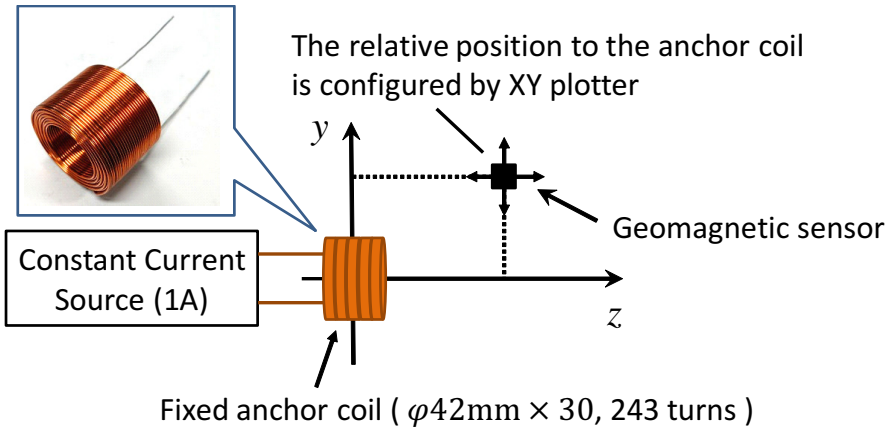

Figure 4.17: Positional relationship between the anchor coil and the sensor node.

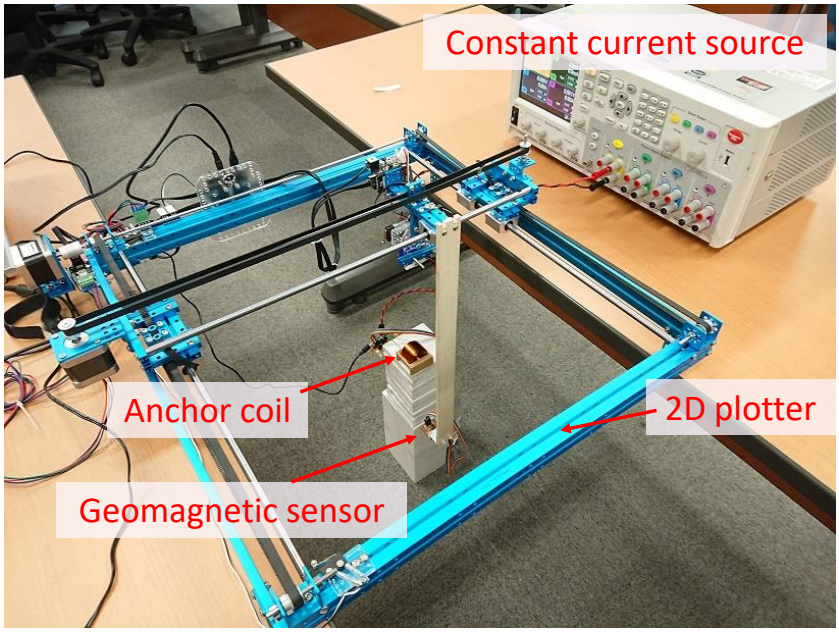

Figure 4.18: Photo of the measurement environment.

4.4.2 Geomagnetism based posture estimation

This section first estimates the posture of the geomagnetic sensor using the geomagnetism only. Here, the posture of the sensor node ψ is defined by the angle difference between the anchor coil and the geomagnetic sensor. This posture estimation procedure is performed with Eq. (4.7) and outputs of the geomagnetic sensor according to the discussion in Section 4.3.2.

Fig. 4.19 shows the result of the posture estimation when the angle difference be-

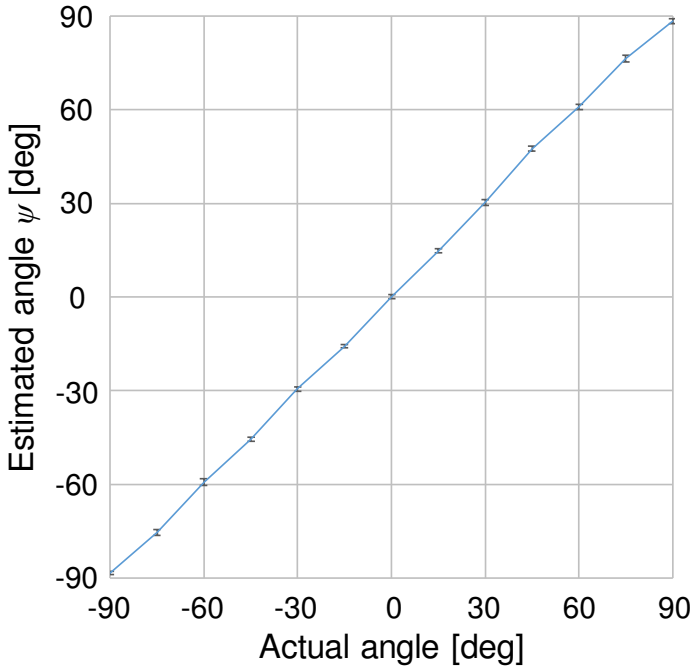

Figure 4.19: Evaluation result of posture estimation.

tween the geomagnetic sensor and the anchor node is varied from -90 to 90 degree. Here, each posture estimation is performed using 10 samples of the sensor output. Error bars in Fig. 4.19 denote the standard deviation that was obtained by 100 experiments each. The mean angle error is 0.88 degree and the maximum estimation error is 2.43 degree, which indicates that the geomagnetic sensor has sufficient accuracy and the system can estimate the posture of the sensor node precisely. With this posture information, we can convert the coordinate system of the sensor node into the anchor node's one using Eq. (4.9) even when the geomagnetic sensor and the anchor coil do not face in the same direction.

4.4.3 Artificially generated magnetic field

Next, this section measures the DC magnetic field generated by the anchor coil to which 1A current is given. The sensor position on yz plane is swept in the range of 400 mm $\times$ 400 mm with 1 mm interval using the 2D plotter, and measure the magnetic field vector 100 times at each point. Fig. 4.20 shows the magnitude and direction of the magnetic field at each point. Fig. 4.20 agrees well with Figs. 4.5 and 4.6, which are obtained by simulation.

Fig. 4.21 shows the relationship between r_0, which is defined in Section 4.3.4, and the magnitude of the measured magnetic field. Fig. 4.21 indicates that the magnitude

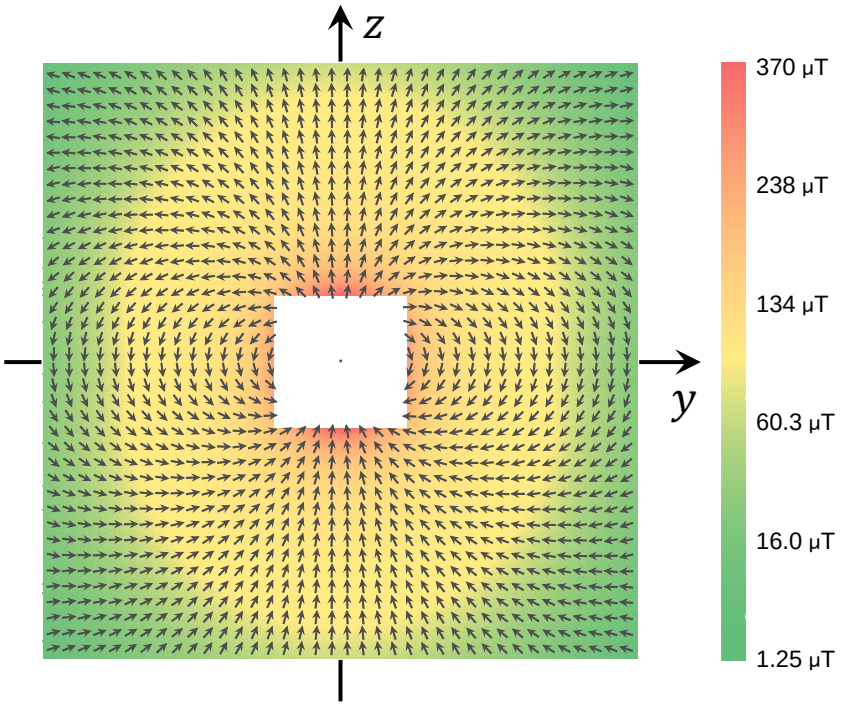

Figure 4.20: Measured magnitude and direction of the magnetic field.

of the magnetic field is proportional to r_0^{-3}, which is already observed in Fig. 4.15 with the numerical simulation. Fig. 4.22 shows the relationship between θ and ξ and also indicates that ξ can be approximated by a cubic polynomial expression of θ. This relationship between θ and ξ also agrees well with the simulation result in Fig. 4.16.

These measurement results in this section support the proposed localization method established by simulation in Section 4.3. Also, Section 4.4.2 confirms that we can estimate the posture accurately. In addition to these, the altitude estimation is also possible since the anchor coil used in the experiment is axially symmetrical and generated magnetic field must be axially symmetrical to z axis. Consequently, we can perform 3D localization with the actual sensor node and equations in Section 4.3.

4.4.4 Localization result

This section performs 3D localization in the range of 150 mm $\times$ 150 mm $\times$ 150 mm with a step of 50 mm. To mitigate the effect of the geomagnetic sensor noise, each localization utilizes the average of 10 samples. In this case, the system can estimate the sensor position two times per second including the latency of the power switching of the anchor coil. Fig. 4.23 shows the 3D localization result, where the average of 100 localization results is plotted at each point. Fig. 4.23 indicates that the proposed single anchor coil based localization method can achieve high localization accuracy with a

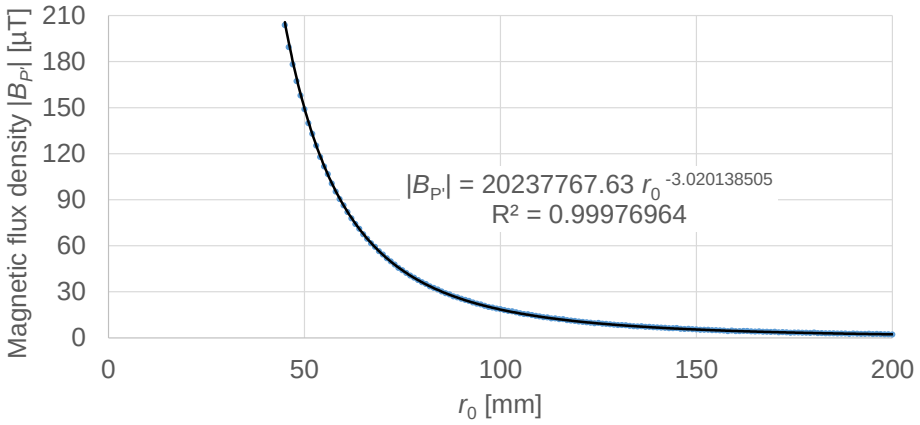

Figure 4.21: Relationship between the measured magnitude of magnetic field and the value of r_0.

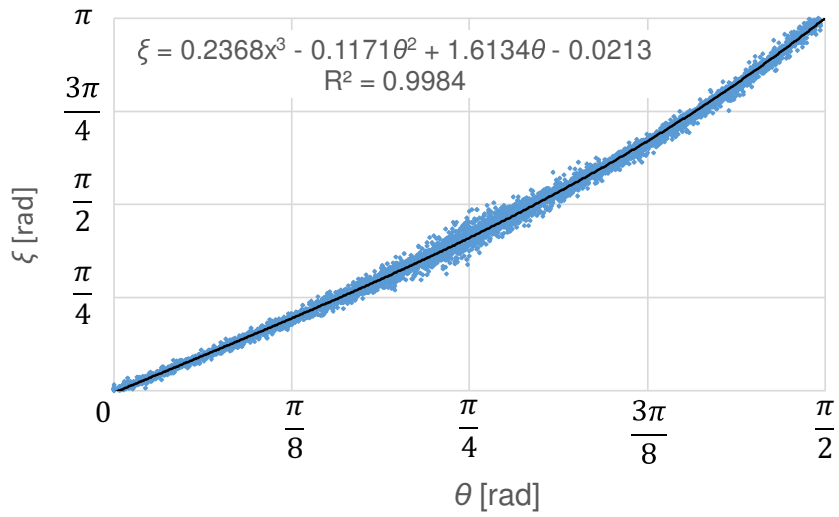

Figure 4.22: Relationship between the measured ξ and θ .

maximum error of 6.5 mm.

The proposed method aims at 3D localization, but when it is applied to 2D localization, even higher accuracy can be attained. The reason of this accuracy improvement will be discussed in Section 4.5.2 and hence this section only focuses on the localization result itself. Fig. 4.24 shows the 2D localization result on the yz plane. Each circle denotes the standard deviation of the localization result at the corresponding position. We can see that the localization error and standard deviation become larger when the anchor-sensor distance becomes longer. Fig. 4.25 shows the relationship between the localization distance and localization error for 2D and 3D cases. The proposed method estimates 2D position with the maximum error of 1mm in the range of 125 mm and the

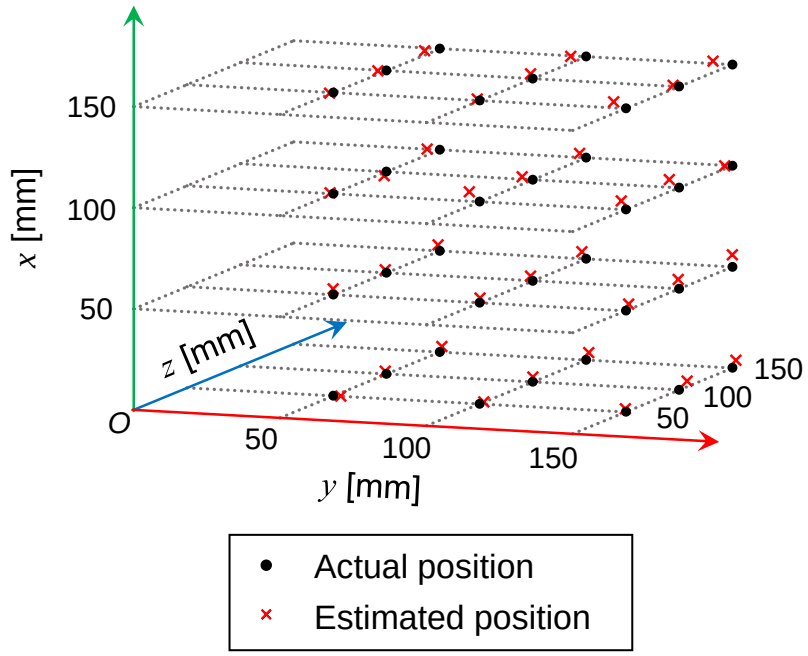

Figure 4.23: 3D localization result.

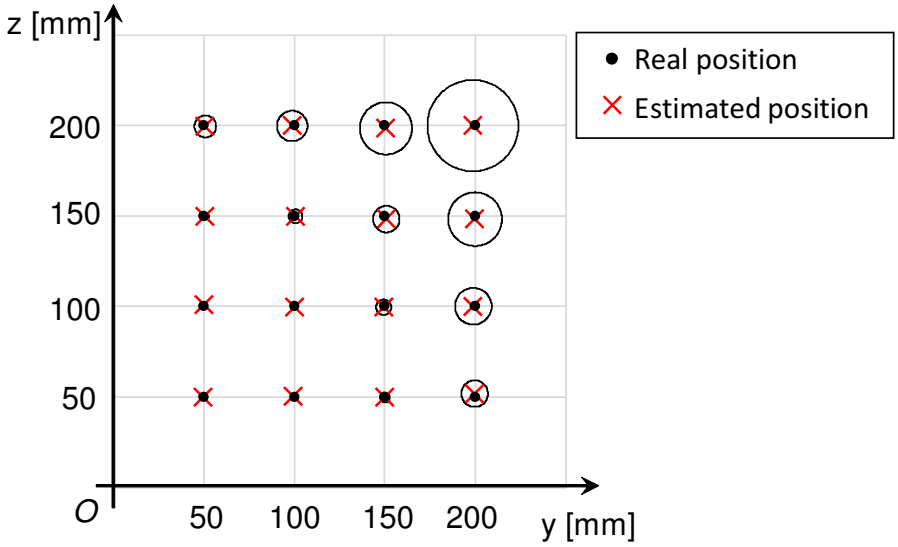

Figure 4.24: 2D localization result. Each circle shows the standard deviation of the localization result at each position.

maximum error of 3mm in the range of 250 mm, whereas in 3D case the maximum error is 3.5 mm in the range of 125 mm and 6.5 mm in the range of 250 mm, respectively. The accuracy improvement in 2D localization will be further discussed in Section 4.5.2.

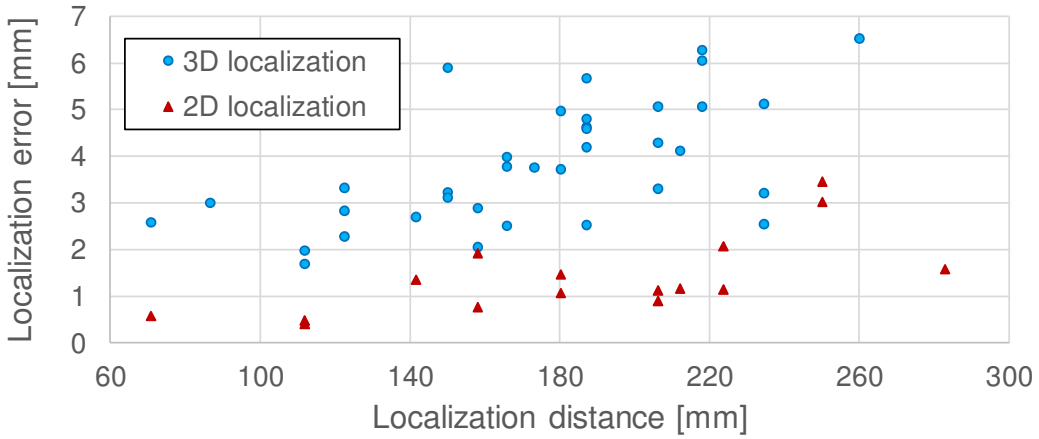

Figure 4.25: Relationship between localization distance and error.

4.4.5 Localization with non-ferrous metallic obstacle

Conventional AC magnetic field based localization methods, as explained in Section 1.3.3, suffer from the interference from metallic obstacles seriously. The proposed DC magnetic field based method, on the other hand, can work in the environment that contains almost all kinds of metallic obstacles except ferrous material since DC magnetic field can penetrate non-ferrous metallic obstacles. This section evaluates the performance of the proposed localization method in the environment with a non-ferrous metallic plate.

The experimental environment is depicted in Fig. 4.26. An aluminum plate whose thickness is 4 mm is installed in parallel to the *xz* plane and the origin-to-plate distance is set to 25 mm. Fig. 4.27 shows the 2D localization result, and it is almost identical with Fig. 4.24 while the existence of metallic plate is different. It is confirmed that non-ferrous metallic obstacle does not disturb the proposed localization method.

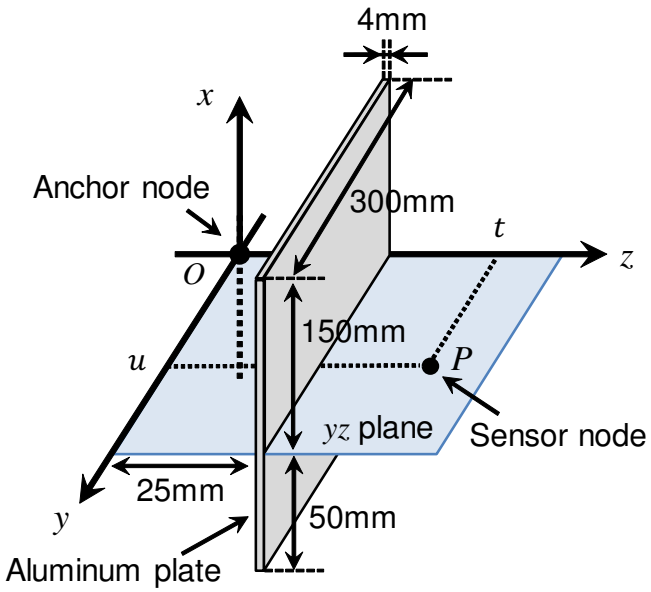

Figure 4.26: Localization experimentation with an aluminum plate.

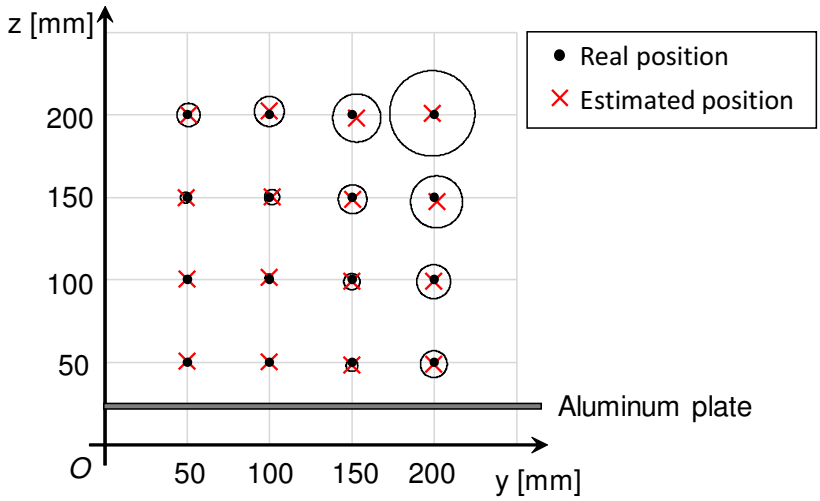

Figure 4.27: 2D localization result with an aluminum plate. Each circle shows the standard deviation of the localization result at each position.

4.5 Discussion

In this section, let us discuss further details about the performance of the proposed localization method. Section 4.5.1 discusses the error caused by Eq. (4.17) that approximates the contour line. Section 4.5.2 explains the reason for the difference of localization er-

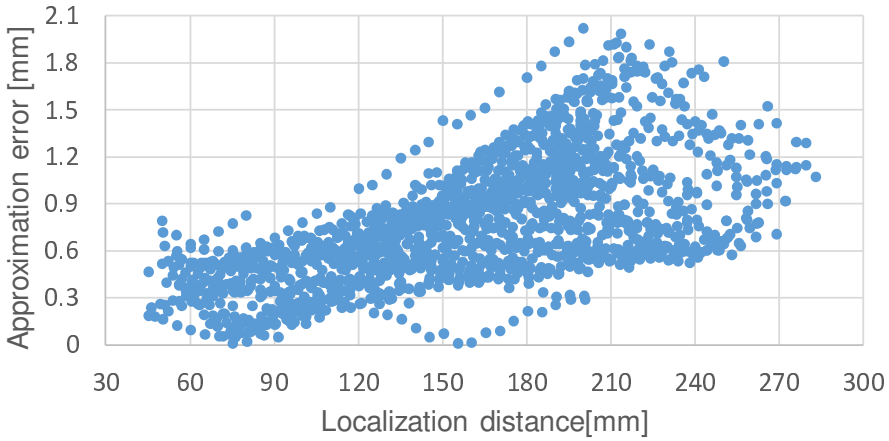

Figure 4.28: Error induced by contour line approximation of Eq. (4.17).

ror between 2D and 3D localization in Fig. 4.25. Section 4.5.3 discusses factors that determine the coverage area of the localization method and introduces two methods to expand the coverage area. Section 4.5.4 experimentally performs coverage area expansion with multiple anchor coil. Section 4.5.5 shows a comparison with related works.

4.5.1 Approximation error of contour lines

As we discussed in Section 4.3, the proposed localization method consists of four steps: posture estimation, altitude estimation, distance estimation, and angle estimation. In the distance estimation step, Section 4.3.4 introduced approximation equation Eq. (4.17) to simplify the calculation. Here in this section, we discuss the error induced by this approximation.

Fig. 4.28 shows the relationship between the localization distance and approximation error in the region of 0 [mm]$\leq y \leq$ 200 [mm], 0 [mm] $\leq z \leq$ 200 [mm] on yz plane. Fig. 4.28 indicates that the approximation error is less than 2.1 mm at the maximum, and therefore it would not be a serious problem. Even when the approximation error observed in Fig. 4.28 is not acceptable in particular applications, the error can be eliminated by using LUT instead of Eq. (4.17).

The approximate equation of Eq. (4.17) requires that the sensor position should be distant enough from the anchor coil. When the sensor is located in the vicinity of the anchor coil, the approximation accuracy degrades. However, LUT-based method can handle such a vicinity region. Note that proposed localization method generates LUT with numerical simulation based on Eq. (4.1), and hence the system does not require any site survey even when utilizing LUT.

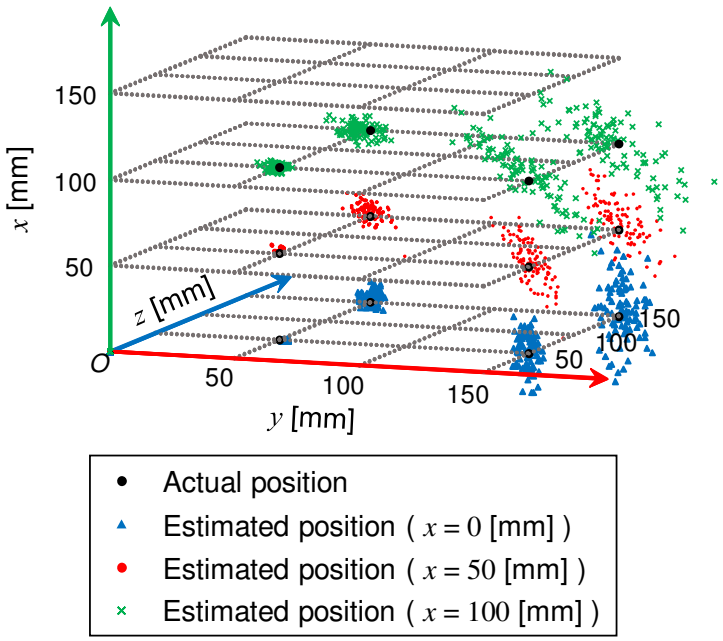

Figure 4.29: Distributions of localized points.

4.5.2 Analysis of localization error

This section analyzes the localization error and discusses the difference of the localization error between 2D and 3D localization observed in Section 4.4.4. Fig. 4.29 shows the spatial distribution of several localized point. Fig. 4.29 indicates that the localization errors tend to spread in λ-direction. This section explains the reason why this phenomenon occurs.

As we discussed in Section 4.2, x-direction component of the generated magnetic field in yz plane is always zero. Therefore, λ-direction component of magnetic field must be zero at any point since the anchor coil has the axially symmetrical structure to z axis. The altitude estimation step, which is explained in Section 4.3.3, is based on the assumption that λ-direction component of magnetic field is zero. Hence, the accuracy of the altitude estimation is severely degraded when the λ-direction component of the measured magnetic field is non-zero because of the noise of the geomagnetic sensor. In 2D localization, we do not have to perform altitude estimation since the altitude of the sensor node is already known, and that is why 2D localization can achieve higher accuracy than 3D localization that requires altitude estimation.

4.5.3 Relationship between coil parameters and coverage area

This section explains factors that determine the size of coverage area and then examines two approaches for coverage area expansion. The localizable distance depends on the magnitude of the magnetic field generated by the anchor coil. Let us discuss the dependence of magnitude of the magnetic field on coil parameters. For simplifying the discussion, this work approximates Eq. (4.1) with Eq. (4.25) supposing r and b satisfy the relationship of $r^2 >> b^2$ [44].

$$\mathbf{B} = \frac{\mu_0 I b^2}{4r^3} \left(\mathbf{e}_r 2\cos\theta + \mathbf{e}_\theta \sin\theta \right). \tag{4.25}$$

Eq. (4.25) tells that I and b, which denote the amount of current injected to the anchor coil and the radius of the anchor coil, respectively, are key factors determining the magnitude of the generated magnetic field. This section investigates which factor is more influential and then more important in the localization system design.

First, we focus on an increase in the amount of current. Eq. (4.25) shows that the localizable distance r is proportional to $I^{1/3}$ when $|B|$ is fixed. Therefore, increasing the current is not so efficient since we have to increase the current eight times for doubling the localizable distance.

Second, we investigate the diameter of the coil. Eq. (4.25) indicates that r is proportional to $b^{2/3}$, which is better than $I^{1/3}$. Also, we can easily increase the winding number of the coil when we enlarge the diameter of the coil. The winding number of the coil N significantly affects the magnitude of the magnetic field and localizable area since $|B| \propto N$. Hence, the strategy of enlarging the diameter and increasing the winding number of the coil should be considered first when the localizable distance expansion is demanded.

4.5.4 Coverage area expansion with multiple anchor coils

Section 4.4 has confirmed that the proposed method is usable for table-top applications. This section expands the coverage area aiming at room-scale applications using two approaches; enlarging the anchor coil and increasing the number of anchor coils.

Conventional multi-anchor based localization techniques require that the positions of all anchor nodes be measured beforehand, and consequently the installation cost is high. However, the proposed method does not require pre-measurement for the second and later anchor nodes since each anchor node can estimate its own position due to the following reason. As explained with Fig. 4.8 in Section 4.3, each anchor node is equipped with not only the localization coil but also the geomagnetic sensor. Therefore, each anchor node can sense the magnetic field generated by the previously installed anchor coil in the system, and then it can localize itself.

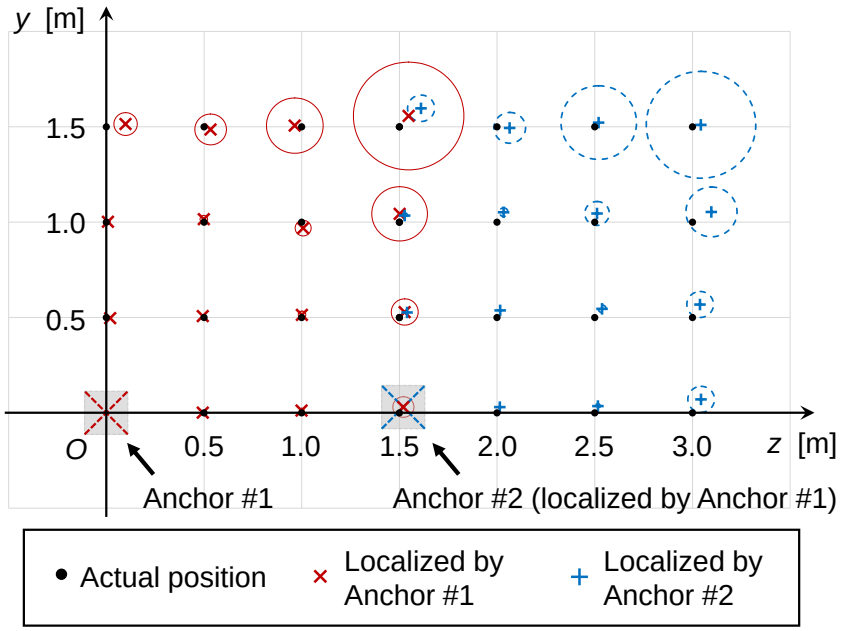

Figure 4.30: Room-scale localization result with multiple anchor coils.

For evaluating the performance of the multi-anchor based localization, the relatively large anchor coil whose size is ϕ135 mm $\times$140 mm is installed. Thanks to the size increase, the coverage area for a single anchor coil expands into 1.5 m $\times$ 1.5 m. First, only Anchor #1 is installed at the origin of the system as shown in Fig. 4.30. Then, Anchor #2 is installed at the position of $y = 0.03000$ [m] and $z = 1.520$ [m]. In this case, the self-localization function estimated the location of $y = 0.0$ [m] and $z = 1.5$ [m]. Anchor #1 and Anchor #2 generate magnetic field in time-division manner to avoid the superposition of the magnetic field. Fig. 4.30 shows the measurement result with these two anchor coils and circles drawn around the localized point shows the standard deviation. The localization with Anchor #1 achieves the maximum error of 9.93 cm in the range of 2.1 m. Beyond this area, Anchor #2 is responsible for the localization, and the system estimates the position with the maximum error of 14.7 cm. In this way, the coverage area is extended by Anchor #2. Here, the localization with Anchor #2 involves larger localization error than that with Anchor #1, because Anchor #2 localizes itself with the magnetic field generated by Anchor #1, and hence the position of the Anchor #2 already includes localization error of 3.62 cm.

Finally, this work investigates the scalability of the time-division based method. As Eq. (4.25) shows, the magnitude of the DC magnetic field generated by the anchor coil is inversely proportional to the cube of the distance. Therefore, the magnetic field generated by the anchor coil decays quickly and the two anchor coils which are installed apart each other can share the radiating time. Hence, the time slot for each anchor node will not be too small and the scalability of the proposed system is sustained.

Table 4.1: Comparison with related work.

	[16]	[105]	[96]	This work
Method	Wifi	AC mag. field	DC mag. field	DC mag. field
Coverage area	Dozens of m	Dozens of cm	Dozens of m	Coil diameter $\times$ 10
Single anchor	–	Yes	No	Yes
Site survey	Necessary	Unnecessary	Necessary	Unnecessary
Sensor volume	below 1 cm^3	over 10 cm^3	below 1 cm^3	below 1 cm^3
Non-ferrous metal	Tolerable	Intolerable	Tolerable	Tolerable
Localization error [cm]	150	0.11	100	0.65@25cm, 14.7@330cm

4.5.5 Comparison with related works

Table 4.1 shows the comparison with related works indicating that the method proposed in [105] also achieves the localization with a single anchor coil. On the other hand, the method proposed in [105] is affected by the non-ferrous metal material since it uses AC magnetic field. Also, the sensor volume is relatively large, which is not suitable for portable application.

Sensor nodes used in localization methods proposed in [16] and [96] are both small and suitable for compact application. However, the method proposed in [16] requires the site survey of Wifi singal, and hence the installation cost is relatively high. The method proposed in [96] does not require the site survey for small area localization, but it requires multiple anchor nodes and the installation cost is still high. Also for expanding the localizible area, the system in [96] requires the site survey, and hence the installation cost becomes much higher according to the localizable area expansion.

From Table 4.1, we can see that the proposed method is scalable and robust to non-ferrous material even with the single anchor coil while achieving high accuracy compared to other related works. For the applications that necessitate small-volume sensor and could have non-ferrous material nearby, the proposed localization method is the sole solution.

4.6 Conclusion

This chapter proposed a DC magnetic field based robust and scalable localization method with single anchor coil. The proposed localization system can reduce the installation cost significantly since the proposed method does not require any site survey or multiple anchor nodes. Also this chapter evaluated the feasibility and the performance with both numerical simulation and hardware measurement. For the tabletop-scale small area localization, the measurement result showed that the proposed localization method could achieve the maximum localization error of 3.5mm in the range of 125 mm from the anchor coil, and the maximum error of 6.5 mm in the range of 250 mm, respectively. When multiple large coils are installed for room-scale localization, the system could es-

timate the sensor position with the maximum error of 14.7 cm in the range of 3.3 m from the anchor coil even when the second anchor coil localizes its own position. The measurement result also indicated that the proposed localization method could work in the environment with non-ferrous metallic material since DC magnetic field can penetrate almost all kind of metallic material unlike the conventional AC magnetic field based method.

With the current calculations described in this chapter, the proposed system cannot tolerate ferrous metallic materials such as steel like other conventional works while some environment may contain ferrous metallic materials or even magnets. S. LaScalza et al. report that characterizing the magnetic field distorted by the ferrous metal is very difficult [123]. However, they also suggest that the accuracy of the DC magnetic field-based method could be improved by tuning the sampling rate according to the collected information about the magnetic permeability of the obstacle. If we scatter a relatively large number of sensor nodes and combine the information from those sensor nodes, the magnetic permeability of the adjacent object could be estimated. Establishing a method which can tolerate the ferrous metallic material is a primary future work.

Chapter 5

An instant magnetic tracking system with coil-free tiny trackers

Chapters 2, 3, and 4 introduced three element technologies, wireless communication, WPT, and localization, required for the sensor node utilized in pervasive sensing application. Sensor nodes in pervasive sensing are generally equipped with the sensing circuit, which is responsible for information collection, in addition to three functions described above. Here, the information of the location and movement of the sensor node is an important information itself as described in Section 1.3.4, and hence can be utilized for AmI since AmI takes advantage of all information surrounding us as mentioned in Section 1.1. Therefore, AmI shall enhance our QoL with the motion information. This chapter proposes a tiny motion tracker based on the technology introduced in Chapter 4 and shows the potential AmI application based on information gathered by multiple trackers.

5.1 Introduction

As described in Section 1.3.4, AmI shall enhance our QoL with the motion information of the sensor node scattered in our daily environment. On the other hand, currently available motion tracking method requires the installation of dedicated equipment and the environment for a specific purpose, which cannot be diverted to other systems. To address this issue, the objective of this chapter is set to developing a small volume motion tracker that can start to trace the movements of objects and people immediately after the attachment without disturbing persons' natural activities.

Fig. 5.1 defines six variables $s, t, u, \phi_{roll}, \phi_{pitch}$, and ϕ_{yaw} that determine the posture and position of an object. Fig. 5.1 indicates that both of posture and position information have 3-DoF (Degrees of Freedom). Hence, the motion tracking system that requires both posture and position estimation has to perform the 6-DoF estimation while the localization method introduced in Section 4 provide only 4-DoF estimation. This chapter,

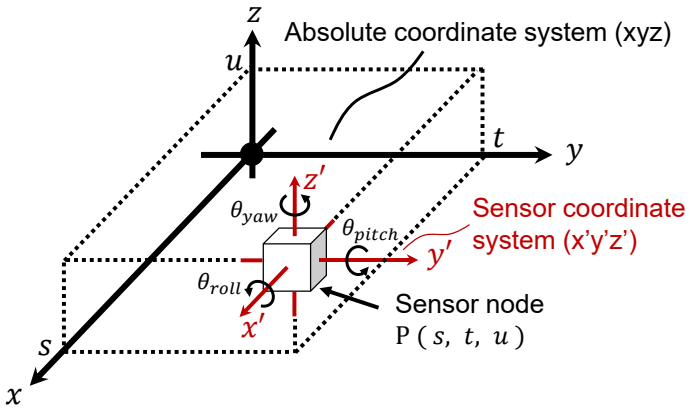

Figure 5.1: Motion tracking requires both position and posture estimation with 6-DoF.

to solve this issue, compensates missing 2-DoF with the information of the gravitational acceleration and enables instant 6-DoF motion tracking.

The rest of this chapter is organized as follows. Section 5.2 introduces the proposed 6 Degrees of Freedom (DoF) motion tracker with DC magnetic filed based localization described in Chapter 4. Section 5.3 evaluates the proposed motion tracker in terms of the tracking accuracy and precision. Section 5.4 discusses the details and the practicability of the proposed system. Finally, the conclusion of this chapter is given in Section 5.5.

5.2 Proposed motion tracking method

This section proposes a DC magnetic field-based motion tracking method with a single reference coil. The localization method proposed in Chapter 4 is promising in terms of robustness, instantness, and accuracy. However, this localization method is limited to 4-DoF estimation, and the other 2-DoF is missing. Therefore, this section explains a method that supplements 2-DoF with an accelerometer. Section 5.2.1 describes the outline of the proposed 6-DoF motion tracking method. Then, Sections 5.2.3 and 5.2.4 explain the details of the posture and position estimation methods, respectively.

5.2.1 Overview

Fig. 5.2 shows an overview of the proposed motion tracking system. The host PC performs wireless communication with the sensor and reference nodes and estimates the posture and position of those with the gravitational acceleration and geomagnetism sensed by those nodes, where one sensor node corresponds to one tracker. In Fig. 5.2, reference node #1 provides an absolute coordinate system, which is depicted as *xyz*-coordinate system, and all the reference and sensor nodes should be localized in this absolute coordinate system. Each sensor and reference node senses the DC magnetic

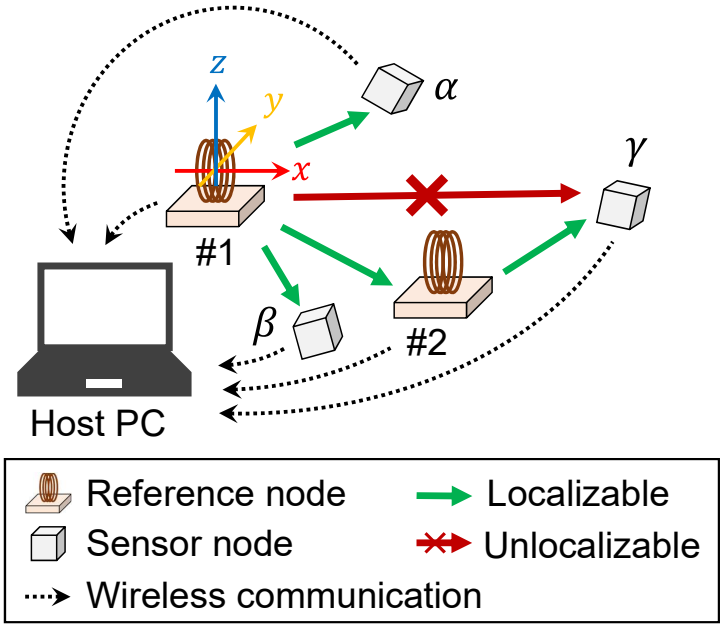

Figure 5.2: Overview of the proposed motion tracking method.

field generated by the reference nodes and sends the measurement results to the host PC via wireless communication. Then, the host PC calculates and estimates the positions of all the sensor and reference nodes from the obtained information.

The reference node has a constant current circuit and a reference coil in addition to the circuit installed in the sensor node. The reason why the reference node includes the sensor circuit is to ensure the system scalability. Let me explain with an example. In Fig. 5.2, sensor node γ and reference node #1 are too distant, and reference node #1 cannot localize sensor γ because of the attenuated magnetic field. Reference node #2 can localize sensor node γ on behalf of reference node #1. However, to localize sensor node γ according to the *xyz*-coordinate system, reference node #2 must know its own position and posture in the *xyz*-coordinate system. Therefore, reference node #2 localizes itself by sensing the DC magnetic field generated by reference node #1 with the sensor circuit mounted on itself. In this way, the proposed method can extend the coverage area by simply adding the reference nodes, and hence the scalability is ensured. Here, Chapter 4 has already reported experimental results showing that the coverage area expansion with multiple reference nodes is feasible. This section focuses on examining the feasibility of tracking with the tiny trackers, which can be attached to anything, for ambient intelligence. Therefore, the following sections will discuss only the tracking ability and the performance with a single reference node.

Figs. 5.3 and 5.4 show the configurations of the reference and sensor nodes implemented in this work, respectively. The external 5V voltage sources shown in Figs. 5.3 and 5.4 are required only for charging the internal battery, and hence all the nodes can

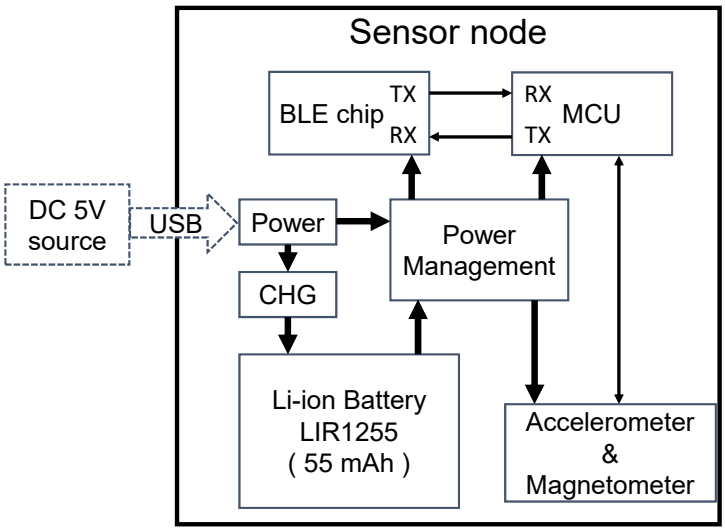

Figure 5.3: Structure of the sensor node.

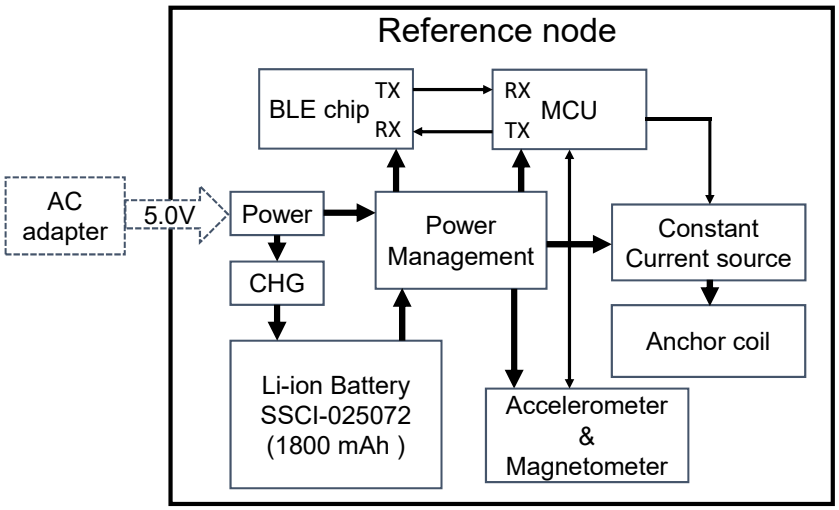

Figure 5.4: Structure of the reference node.

work wirelessly during the motion tracking. The sensor node consists of a power management circuit, an MCU (Micro Controller Unit), a 6-axis sensor (magnetometer and accelerometer), and a BLE (Bluetooth Low Energy) chip for wireless communication. As a 6-axis sensor, this work adopt LSM9DS1 that includes not only an accelerometer and a magnetometer but also a gyroscope. Besides, the power consumption of the gyroscope is significantly larger than those of the other two sensors, and then the gyroscope is disabled in this work.

The proposed method can provide a tracking service simply by installing a single reference node. The coverage area of a single reference node is determined by the

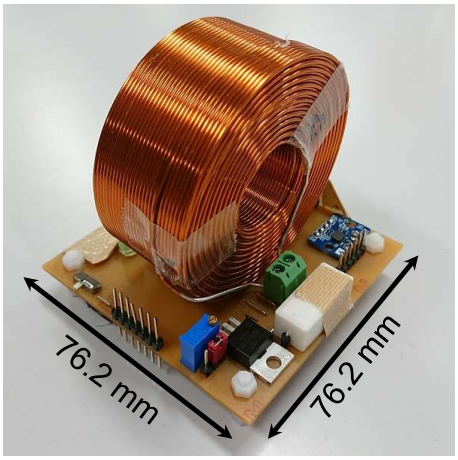

Figure 5.5: Prototyped reference node.

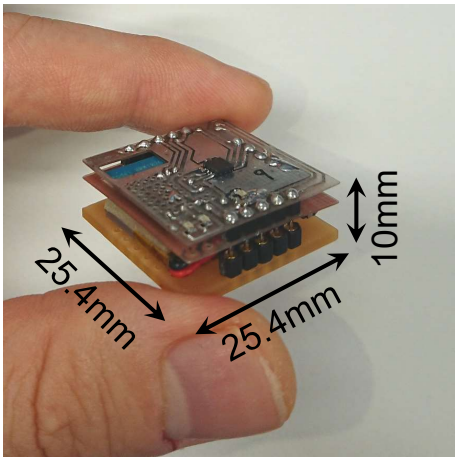

Figure 5.6: Prototyped thin sensor node used as a tracker.

amount of the power given to the reference coil and the coil size. Fig. 5.5 exemplifies the reference node for tabletop applications, and it supports a tracking service within a range of several dozens of centimeters. The volume of this reference node for tabletop applications is 76.2mm $\times$ 76.2mm $\times$ 76.2mm. Please note that this work also implemented a large reference node for the room-scale tracking and conducted the experiment with it, which will be explained later in Section 5.4.

This chapter aims to realize a small tracker that can be attached to everything around us. Therefore, the sensor node used as a tracker should be implemented not only in a small volume but also with thin thickness so that the attachment flexibility is much improved. Fig. 5.6 shows the appearance of the prototyped sensor node to be used as a tracker. This thin sensor node is implemented in a volume of 25.4mm $\times$ 25.4mm $\times$ 10mm. Users can instantly and immediately make any object or person trackable by attaching the tracker with double-sided tape.

The sensor node, of course, can be in any shape as long as it includes the circuits described above. Thus, this work prototyped another type of cube-shaped sensor node shown in Fig. 5.7, which could be suitable for other applications (e.g., 3D modeling, game control). The function of the cube-shaped sensor node in Fig. 5.7 is identical to the thin sensor node in Fig. 5.6. Fig. 5.8 shows the disassembled cube-shaped sensor node. We can see that the volume of the 6-axis sensor mounted on the sensor board is tiny as it is 3mm $\times$ 3mm $\times$ 1mm. Therefore, we can implement the circuit for motion tracking even in a volume of mm^3 class by putting more effort into custom chip fabrication.

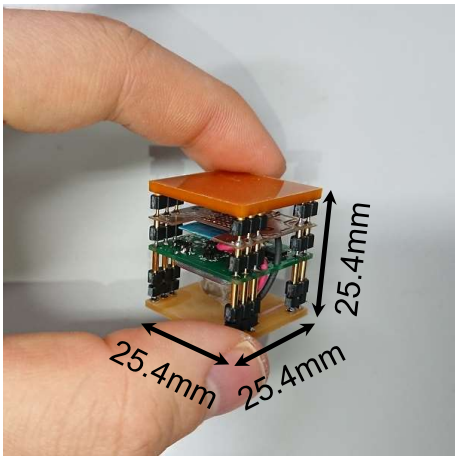

Figure 5.7: Prototyped cubic sensor node.

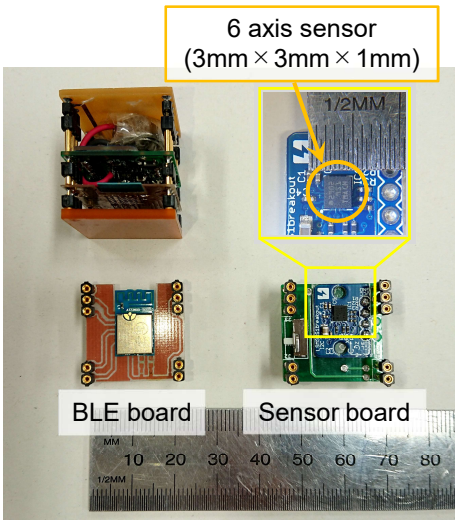

Figure 5.8: Disassembled cubic sensor node.

5.2.2 Motion tracking procedure

This section explains the procedure of posture and position estimation performed in the system. The posture estimation uses gravitational acceleration and geomagnetism, which will be detailed in Section. 5.2.3. Therefore, the system needs to order all the reference nodes to disable the reference coil. The system then commands all the reference and sensor nodes to measure geomagnetism and gravitational acceleration.

After all the reference and sensor nodes have completed the measurement, the system chooses one reference node and commands it to enable the reference coil in it. Then, all the sensor nodes and reference nodes except the selected reference node measure the DC magnetic field generated by the selected reference node. When all the nodes have completed the measurement of the artificially generated magnetic field, the system orders the same reference node to disable the coil and orders another reference node to enable the reference coil. Please note that no more than one reference node in the system enables the coil at the same time since all the reference nodes follow the single time division scheme controlled by the system.

After all the reference nodes have completed the coil activation and deactivation, the system now has the information on the gravitational acceleration, geomagnetism, and the magnetic field vector generated by the reference nodes at each sensor location. The system estimates the posture and position of all the reference and sensor nodes based on this information, which will be explained in the successive subsections.

5.2.3 Posture estimation

The position estimation method proposed in Chapter 4 supports posture estimation in addition to 3-DoF localization. However, this posture estimation is limited to 1-DoF. Therefore, 2-DoF is missing and must be compensated. In the proposed method, the host PC estimates the posture of the sensor node with the 6-axis sensor. The sensor position and posture are represented by six variables $s, t, u, \phi_{roll}, \phi_{pitch}, \phi_{yaw}$, as we discussed with Fig. 5.1. The posture estimation step estimates three variables $\phi_{roll}, \phi_{pitch}, \phi_{yaw}$ out of the six variables.

Two important signals in the posture estimation step, which are gravitational acceleration and geomagnetism, are measured by a magnetometer and accelerometer, respectively. Here, as mentioned in Section 5.2.1, all the posture and position estimation results should be based on the absolute *xyz*-coordinate system defined by reference node #1. On the other hand, the accelerometer and magnetometer installed in the sensor node output the information according to the $x'y'z'$-coordinate system, which is the original coordinate system of the sensor node. When there is no artificial magnetic field, which is caused by magnetic materials or coils, in the environment, the geomagnetic vector and the gravitational acceleration vector must be identical at an arbitrary point. Therefore, the posture difference between the reference and sensor nodes can be estimated by comparing the output differences of the magnetometer and accelerometer between the reference and sensor nodes [124]. Here, four variables are defined as follows:

$$\begin{aligned} \mathbf{A}_R &= \begin{bmatrix} a_{Rx} \\ a_{Ry} \\ a_{Rz} \end{bmatrix}, \quad \mathbf{B}_{Rd} = \begin{bmatrix} a_{Rxd} \\ a_{Ryd} \\ a_{Rzd} \end{bmatrix}, \\ \mathbf{A}_S &= \begin{bmatrix} b_{Sx'} \\ b_{Sy'} \\ b_{Sz'} \end{bmatrix}, \quad \mathbf{B}_{Sd} = \begin{bmatrix} b_{Sx'd} \\ b_{Sy'd} \\ b_{Sz'd} \end{bmatrix}, \end{aligned} \tag{5.1}$$

where $\mathbf{A}_R$ and $\mathbf{B}_{Rd}$ are the accelerometer and magnetometer outputs of the reference node, respectively, and $\mathbf{A}_S$ and $\mathbf{B}_{Sd}$ are the outputs of the sensor node. These variables satisfy Eq. (5.2) below.

$$\begin{aligned} \mathbf{A}_R &= \mathbf{R}_z(\phi_{yaw})\, \mathbf{R}_y(\phi_{pitch})\, \mathbf{R}_x(\phi_{roll})\, \mathbf{A}_S. \\ \mathbf{B}_{Rd} &= \mathbf{R}_z(\phi_{yaw})\, \mathbf{R}_y(\phi_{pitch})\, \mathbf{R}_x(\phi_{roll})\, \mathbf{B}_{Sd}. \end{aligned} \tag{5.2}$$

Matrices $\mathbf{R}_x(\phi)$, $\mathbf{R}_y(\phi)$ and $\mathbf{R}_z(\phi)$ in Eq. (5.2) are the rotation matrices around *x*-axis,

y-axis, and z-axis, respectively, and they are defined as Eq (5.3).

$$\begin{aligned}
\mathbf{R}_x(\phi) &= \begin{bmatrix} 1 & 0 & 0 \\ 0 & \cos\phi & -\sin\phi \\ 0 & \sin\phi & \cos\phi \end{bmatrix}. \\
\mathbf{R}_y(\phi) &= \begin{bmatrix} \cos\phi & 0 & \sin\phi \\ 0 & 1 & 0 \\ -\sin\phi & 0 & \cos\phi \end{bmatrix}. \\
\mathbf{R}_z(\phi) &= \begin{bmatrix} \cos\phi & -\sin\phi & 0 \\ \sin\phi & \cos\phi & 0 \\ 0 & 0 & 1 \end{bmatrix}.
\end{aligned} \tag{5.3}$$

To simplify the discussion, we assume $a_{Rx} = a_{Ry} = 0$, which means the gravitational acceleration vector is parallel to the z-axis and is a realistic assumption for most systems. In this case, the sensor posture $\phi_{roll}, \phi_{pitch}, \phi_{yaw}$ can be obtained as Eq. (5.4). Here, it should be noted that even if this assumption does not hold, that is, if the reference node is installed in an inclined plane, the tilt angle of the z-axis can be calculated with the first two equations in Eq. (5.4) by using $\mathbf{A}_R$ instead of $\mathbf{A}_S$. Thus, the posture difference between the reference node and the sensor node can be obtained.

$$\begin{aligned}
\phi_{roll} &= \operatorname{atan2}\left(a_{Sy'}, a_{Sz'}\right). \\
\phi_{pitch} &= \operatorname{atan2}\left(-a_{Sx'}, \sqrt{a_{Sy'}^2 + a_{Sz'}^2}\right). \\
\phi_{yaw} &= \operatorname{atan2}\left(-\cos\phi_{roll} b_{Sy'd} + \sin\phi_{roll} b_{Sz'd}\right., \\
&\quad \cos\phi_{pitch} b_{Sx'd} + \sin\phi_{pitch}\sin\phi_{roll} b_{Sy'd} \\
&\quad \left. + \sin\phi_{pitch}\cos\phi_{roll} b_{Sz'd}\right) \\
&\quad - \operatorname{atan2}\left(-b_{Ryd}, b_{Rxd}\right).
\end{aligned} \tag{5.4}$$

Here, $\operatorname{atan2}(y,x)$ included in Eq. (5.4) is a function defined by Eq. (5.5), which extends the range of the arctangent function from $-\pi/2 < \phi < \pi/2$ to $-\pi \le \phi \le \pi$.

$$\operatorname{atan2}(y,x) = \begin{cases} \tan^{-1}(y/x) & \text{if } x > 0, \\ \tan^{-1}(y/x) + \pi & \text{if } x < 0 \text{ and } y \ge 0, \\ \tan^{-1}(y/x) - \pi & \text{if } x < 0 \text{ and } y < 0, \\ \pi/2 & \text{if } x = 0 \text{ and } y > 0, \\ -\pi/2 & \text{if } x = 0 \text{ and } y < 0, \\ \text{undefined} & \text{if } x = 0 \text{ and } y = 0. \end{cases} \tag{5.5}$$

This section explained the posture estimation based on the outputs from the accelerometer and the magnetometer. On the other hand, we need to pay attention to the fact that the output of the magnetometer usually contains some offset error, and it

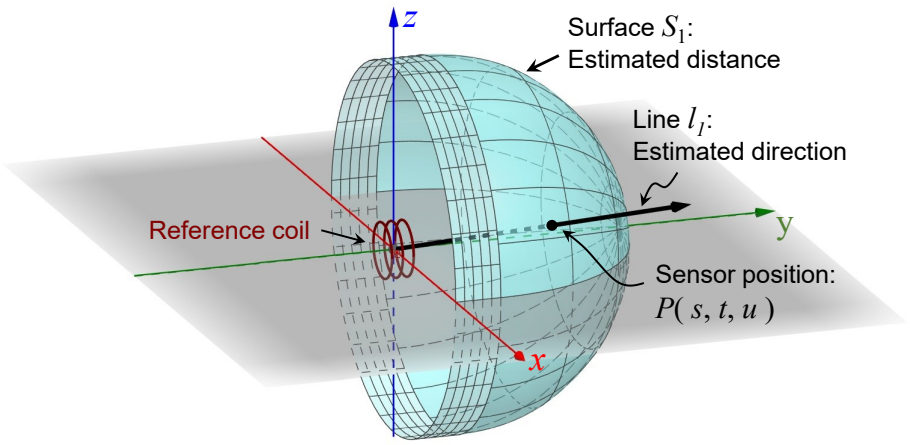

Figure 5.9: Overview of the localization method.

needs to be compensated beforehand. Generally, each sensor node needs its separate compensation, and hence the sensor installation cost can be relatively high. However, this research assumes that a large number of sensors are scattered in the environment. Hence, the newly installed sensor node can compensate its offset error using the data shared from previously installed adjacent sensor nodes. For this reason, the offset compensation will not be a big issue to adopt the proposed method for ambient intelligence.

5.2.4 Position estimation

The sensor position estimation in this work uses the DC magnetic field-based localization method proposed in Chapter 4. First, this section briefly reviews this method combining 3-DoF posture estimation introduced in the previous section. Fig. 5.9 shows an overview of the localization method with a single reference coil. The localization can be divided into two steps: distance estimation and direction estimation. The first distance estimation step estimates the distance between the reference coil and the sensor node using only the magnitude of the magnetic field measured by the sensor node. Then, it derives the equation of surface S_1 in Fig. 5.9. The subsequent direction estimation step estimates the equation of straight line l_1 representing the direction of the sensor node from the reference coil. This l_1 estimation is based on the direction information of the magnetic field measured by the sensor node. The intersection of surface S_1 and line l_1 is uniquely determined, and then the position of the sensor is identified. Following Sections 5.2.4 and 5.2.4 describe the details of the distance and direction estimation, respectively.

Distance estimation step

This step derives contour surface S_1 corresponding to the distance from the reference coil to the sensor $P(s,t,u)$. The localization requires the posture estimation results, which are explained with $\phi_{roll}, \phi_{pitch}, \phi_{yaw}$, and the geomagnetism vector $\mathbf{B}_{Sd}$ measured in the posture estimation phase. Let $\mathbf{B}_{Pe} = [b_{Px'e}, b_{Py'e}, b_{Pz'e}]$ denote the output of the sensor node when the system is injecting current to the reference coil. Here, $\mathbf{B}_{Pe}$ includes not only the magnetic field $\mathbf{B}_P = [b_{Px'}, b_{Py'}, b_{Pz'}]$ generated by the reference coil but also the geomagnetism $\mathbf{B}_{Sd}$. To obtain $\mathbf{B}_P$, we calculate $\mathbf{B}_P = \mathbf{B}_{Pe} - \mathbf{B}_{Sd}$. In addition to this, since $\mathbf{B}_P$ is expressed according to the $x'y'z'$-coordinate system, we perform coordinate transformation:

$$\mathbf{B}_{Pt} = [b_{Pxt}, b_{Pyt}, b_{Pzt}] = \mathbf{R}_z(\phi_{yaw})\ \mathbf{R}_y(\phi_{pitch})\ \mathbf{R}_x(\phi_{roll})\mathbf{B}_P. \tag{5.6}$$

According to Section 4.3, the equation of the surface S_1 is expressed as follows:

$$S_1 : \quad \begin{cases} x^2 + \left(y - \frac{1}{4}r_0\right)^2 + z^2 = r_0^2 & \text{if } |y| > \frac{1}{4}r_0, \\ x^2 + z^2 = r_0^2 & \text{otherwise,} \end{cases} \tag{5.7}$$

where r_0 in Eq. (5.7) is defined by Eq. (5.8).

$$r_0 = \left(\frac{|\mathbf{B}_{Pt}|}{\alpha}\right)^{-\frac{1}{\beta}}, \tag{5.8}$$

where α and β are approximation constants. When the coil specifications are given, α and β are easily obtained since the magnitude and direction of the DC magnetic field generated by a single reference coil at an arbitrary point can be calculated analytically [44].

Direction estimation step

The objective of the direction estimation step is to derive the equation of line l_1. As shown in Fig. 5.10, line l_1 is determined by two angles: λ and θ. Here, λ and θ are calculated as follows:

$$\begin{aligned} \lambda &= \text{atan2}\left(b_{Pzt}, b_{Pxt}\right), \\ \theta &= a_\theta \xi^3 + b_\theta \xi^2 + c_\theta \xi + d_\theta, \end{aligned} \tag{5.9}$$

where $a_\theta, b_\theta, c_\theta$, and d_θ are approximation constants which are derived by the relationship between the reference-sensor direction and the direction of magnetic field. ξ is defined by Eq. (5.10).

$$\xi = \pi/2 - \text{atan2}(b_{Pyt}, b_{Pzt}\sin\lambda + b_{Pxt}\cos\lambda). \tag{5.10}$$

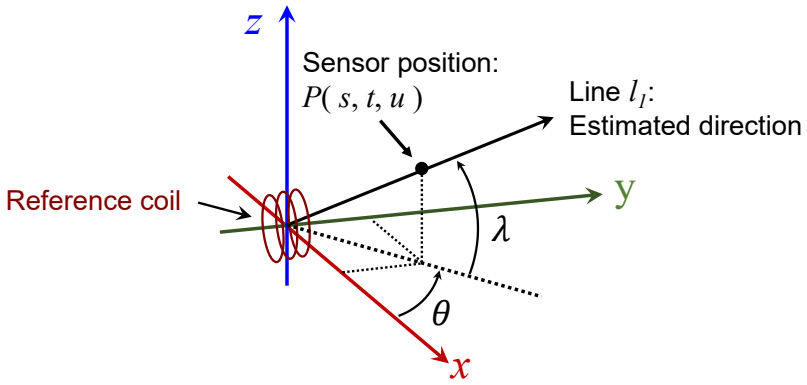

Figure 5.10: Line l_1 and definition of λ and θ.

The intersection of surface S_1 and line l_1 represents the position of the sensor node $P(s,t,u)$ and is expressed as follows:

$$\begin{aligned} s &= t\cos\lambda. \\ t &= \frac{r_0}{4}\tan^2\left(\frac{\pi}{2}-\theta\right)\frac{1+\sqrt{16+\frac{15}{\tan^2\left(\frac{\pi}{2}-\theta\right)}}}{1+\tan^2\left(\frac{\pi}{2}-\theta\right)}. \\ u &= t\sin\lambda. \end{aligned} \tag{5.11}$$

5.3 Hardware evaluation

This section validates the proposed method and examines the performance. Here, tracking in a small area often requires higher accuracy and update rate, whereas tracking in a wider area may tolerate relatively larger error and the low update frequency. For example, in a tabletop application, the system should provide tracking with a maximum error of several mm at an update rate of at least several Hz. On the other hand, when it comes to room-scale ambient intelligence, the system can tolerate a tracking error of several cm, and the update rate can be even reduced to around 1 Hz [125]. Therefore, the hardware evaluation in this section focuses on table-top tracking having the severer performance requirements. This work utilizes a coil whose diameter is ϕ68 mm $\times$ 30mm, and inductance is 10 mH as the reference coil for the tabletop-scale application, which is found in Fig. 5.5. The current injected to the reference coil is set to 1 A. As for room-scale tracking, Section 5.4.3 will show use cases in the range of several meters from the reference node.

Section 5.3.1 evaluates the accuracy of the 3-DoF posture estimation of the sensor node. Section 5.3.2 shows the localization accuracy of the proposed method. Then, Section5.3.3 shows the performance of the motion tracking function, and Section 5.3.4 evaluates the speed and update frequency of the proposed motion tracking system.

5.3.1 Posture estimation

This section evaluates the posture estimation performance of the proposed system. As we discussed in Section 5.1, the posture of the sensor node has 3-DoF expressed with three variables $\phi_{roll}, \phi_{pitch}, \phi_{yaw}$. This section discusses the 1-DoF estimation followed by the 3-DoF estimation.

Fig. 5.11 plots the angle estimation results when two angles out of $\phi_{roll}, \phi_{pitch}, \phi_{yaw}$ are set to 0 degree and only one angle is changed from -180 to 180 degrees. To show the static performance of the 1-DoF estimation, this work estimated each angle 10,000 times. Fig. 5.11 shows the averaged results. The posture estimation method based on the gravitational acceleration and geomagnetism can estimate 1-DoF angle with high accuracy.

On the other hand, some tabletop-scale applications require the real-time update and consequently cannot average many samples. Therefore, the system should be evaluated not only with the accuracy but also with the precision, where please remind that accuracy means how close the average value is to the actual value, and precision represents the variance of the measurement data. Fig. 5.12 plots the averages and standard deviations of the estimation errors in Fig. 5.11 to examine the accuracy and precision at the same time. The average estimation error of each angle is less than ± 2 degrees. Focusing on ϕ_{roll} and ϕ_{pitch}, the standard deviations are less than 0.23 degrees, and the system can achieve precise estimation. As for ϕ_{yaw} estimation, on the other hand, the standard deviation is 1.48 degrees at maximum, and the precision is lower compared to ϕ_{roll} and ϕ_{pitch} estimation. This difference originates from the precision difference between the accelerometer and magnetometer. Variable ϕ_{yaw} is estimated from the magnetometer output with a large standard deviation, while the other two variables ϕ_{roll} and ϕ_{pitch} are estimated from the accelerometer output with a small standard deviation. Here, the magnetometer embedded in the 6-axis sensor of the proposed system supports the data averaging [126] and can mitigate the output variation. Fig. 5.13 shows the ϕ_{yaw} estimation result with this averaging function. The averaging function reduces the standard deviation from 1.48 to 1.06 degrees and contributes to the higher precision. However, further averaging lowers the data rate and causes an insufficient update rate problem. Therefore, the proposed system just utilizes the averaged sensor output and does not conduct further averaging. The precision problem regarding motion tracking performance will be discussed in Section 5.3.3.

Fig. 5.14 shows the 3-DoF posture estimation results, where all the variables $\phi_{roll}, \phi_{pitch}, \phi_{yaw}$ are changed simultaneously. This work selected four combinations of $(\phi_{roll}, \phi_{pitch}, \phi_{yaw})$ = (a): (0, 0, 0), (b): (45, 0, 0), (c): (45, 45, 0), and (d): (45, 45, 45) in consideration of symmetry. Each posture is estimated 10,000 times and the average and standard deviation of the estimation error are calculated. In Fig. 5.14, x_{err} denotes the average angle estimation error in the x-axis of the sensor node, x_{SD} is the standard deviation, and the same for the y-axis and z-axis. Fig. 5.14 shows that the system can estimate the sensor axis directions with the maximum estimation error of 1.65 degrees

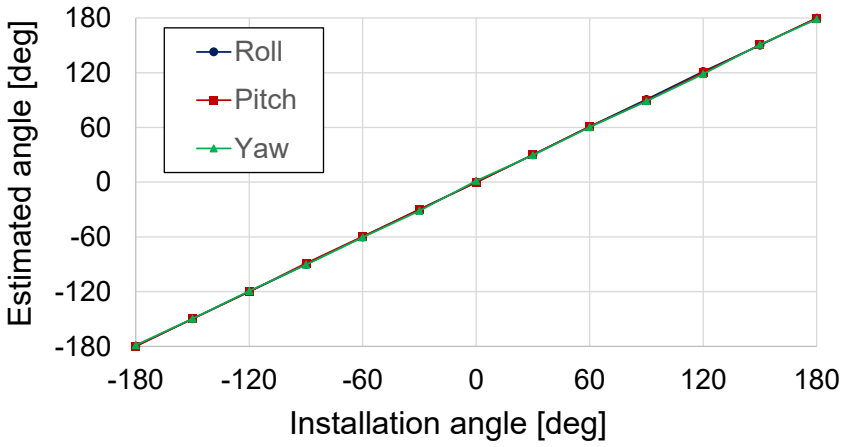

Figure 5.11: Result of 1-DoF sensor angle estimation.

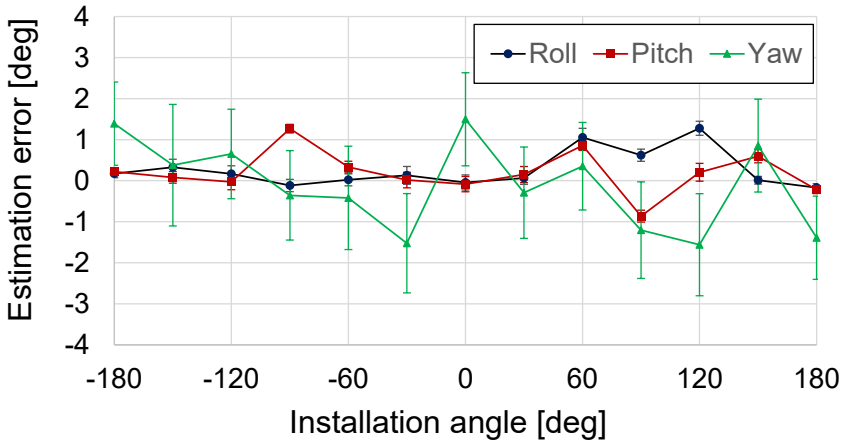

Figure 5.12: Angle estimation errors.

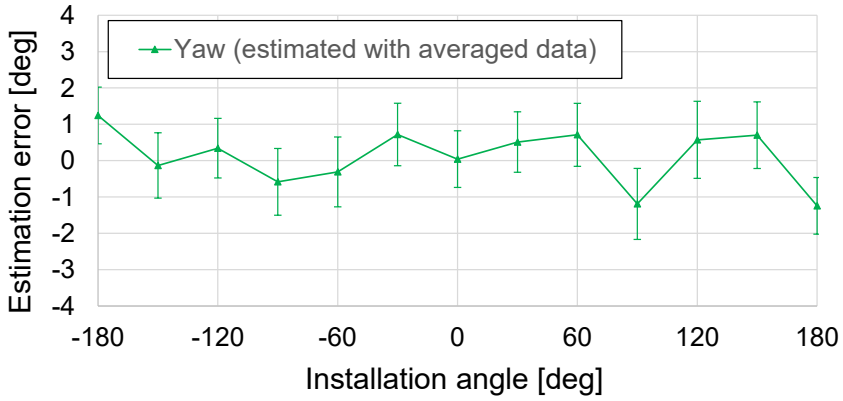

Figure 5.13: Result of yaw angle estimation based on the averaged sensor output.

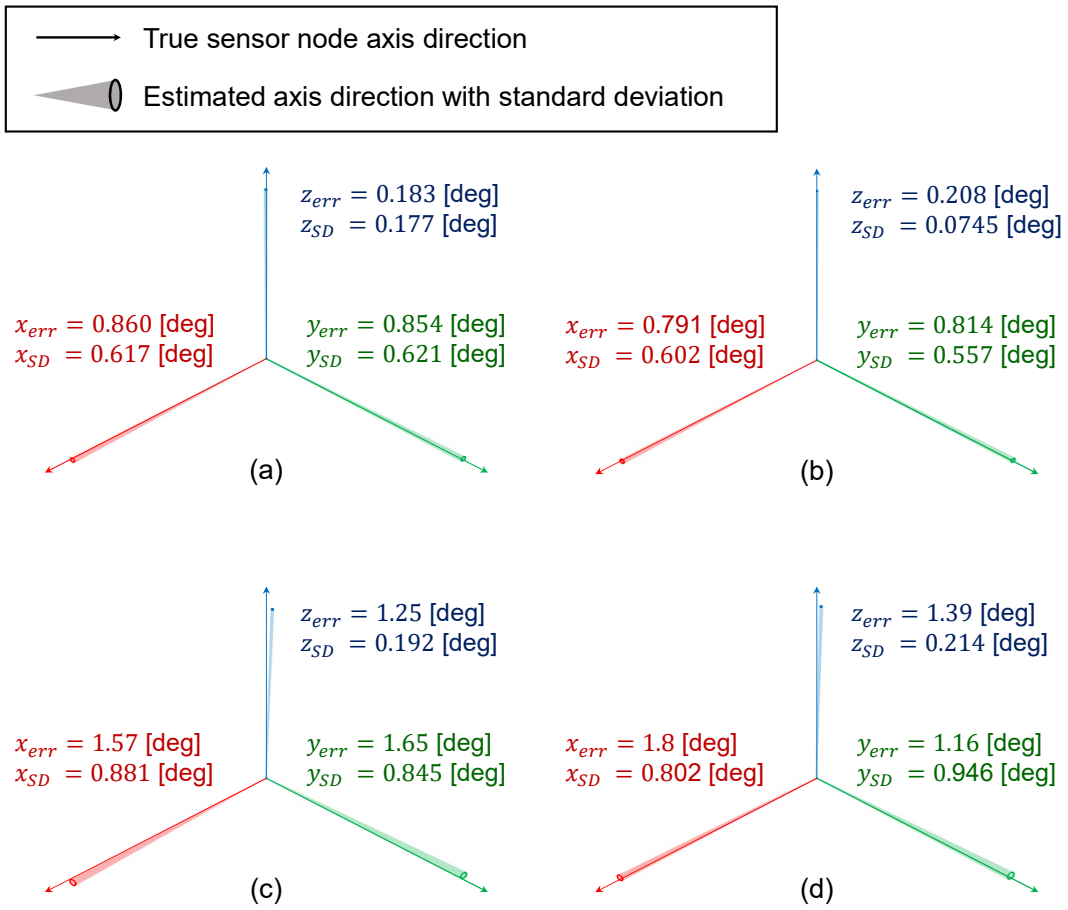

Figure 5.14: 3-DoF posture estimation result with various installation angles. (a): (ϕ_{roll}, ϕ_{pitch}, ϕ_{yaw}) = (0, 0, 0) [deg], (b):(ϕ_{roll}, ϕ_{pitch}, ϕ_{yaw}) = (45, 0, 0) [deg], (c):(ϕ_{roll}, ϕ_{pitch}, ϕ_{yaw}) = (45, 45, 0) [deg], (d): (ϕ_{roll}, ϕ_{pitch}, ϕ_{yaw}) = (45, 45, 45) [deg].

and the standard deviation is 0.946 degrees at maximum at any posture. In our daily environment, most applications tolerate the posture estimation error of 1.65 degrees, and then this work concludes that the system can estimate the posture of the sensor with sufficient accuracy and precision. Meanwhile, the posture estimation error affects the localization performance. Therefore, we will discuss the impact of the posture error on the localization accuracy in Section 5.4.1.

5.3.2 Localization

Fig. 5.15 shows the localization results in the area of 300 mm × 300 mm × 200 mm. The black points are the actual positions, the red cross marks are the positions estimated as the averages of 500 estimates, and the black bars around the red cross marks denote the error bars corresponding to one standard deviation. The reference coil is positioned

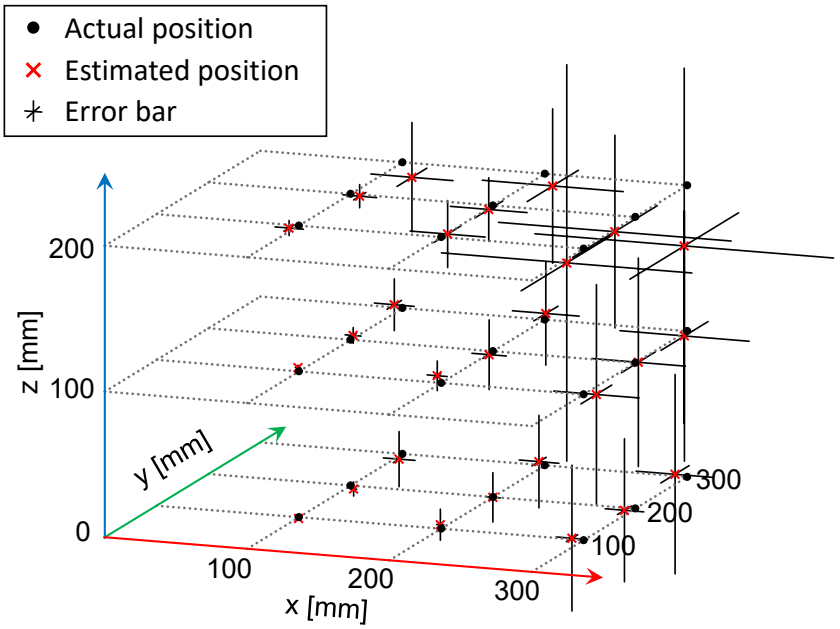

Figure 5.15: 3D localization result.

at (0, 0, 0). Fig. 5.15 indicates that accuracy and precision are high near the reference coil. On the other hand, both the accuracy and precision deteriorate at the points apart from the reference coil. Nevertheless, as the static localization performance, the system achieves the maximum localization error of 9.69 mm in the range of 350 mm from the reference coil. Please note that the localizable area is four times larger than the result shown in Fig. 5.15 since the localizable area of the proposed method is axially symmetric to the y-axis while Fig. 5.15 shows the result only in the region of $x \geq 0, z \geq 0$.

5.3.3 Motion tracking

Motion tracking requires dynamic position estimation, while ordinary localization requires static position estimation. In the motion tracking, the sensor position changes over time, and then we cannot average many samples. Therefore, it is more difficult than static localization. Accordingly, the system calculates and uses the average value of the latest 20 localization results, which means the data rate is unchanged while minimizing the effect of error fluctuation. Fig. 5.16 shows the tracking results when the sensor node moves at a speed of approximately 2.5 cm per second. The update frequency of the system is fixed to 6.25Hz to guarantee stable wireless communication. Fig. 5.16 indicates that the proposed motion tracking system can track the sensor position accurately, even with the single reference coil and small 6-axis sensor.

One of the advantages of the proposed system is the robustness to non-ferrous metal-

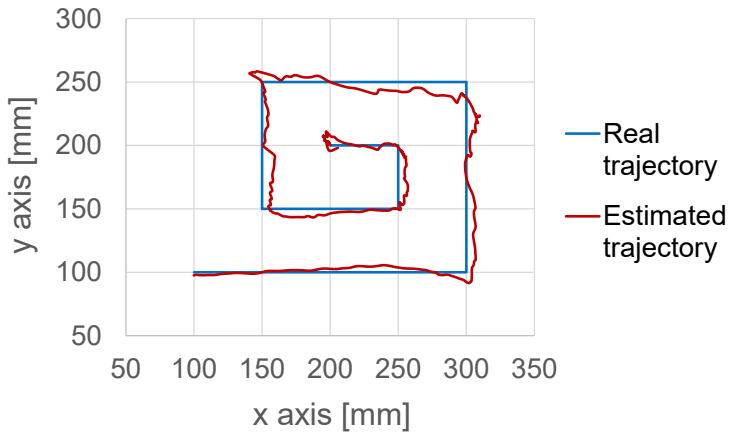

Figure 5.16: Motion tracking result.

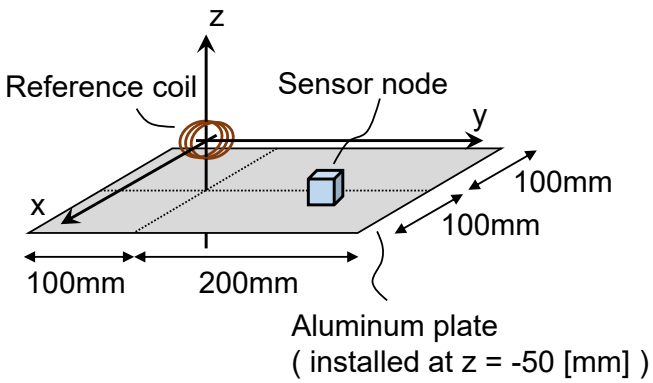

Figure 5.17: Motion tracking with aluminum plate.

lic materials, which are common in our daily environment, as explained in Section 4.4.5. To confirm this robustness, this work examined the motion tracking performance with the setup of Fig. 5.17, where a large aluminum plate whose thickness is 4 mm is installed at $z = -50$ [mm]. Please remind that the AC magnetic field-based methods are disturbed by the plate and they cannot localize or track the sensor position at all. Fig. 5.18 shows the motion tracking result. The sensor movement speed and the trajectory of the sensor node are identical with the experiment shown in Fig. 5.16. Fig. 5.17 indicates that the motion tracking accuracy does not degrade even though the aluminum plate is placed just below the tracking area.

5.3.4 Update frequency

Table 5.1 shows three key factors that determine the posture and location update rate of the current prototype: BLE communication, the overhead in the host PC, and the overhead in the MCU. The time required to finish each cycle is 65.98 ms, and the achieved

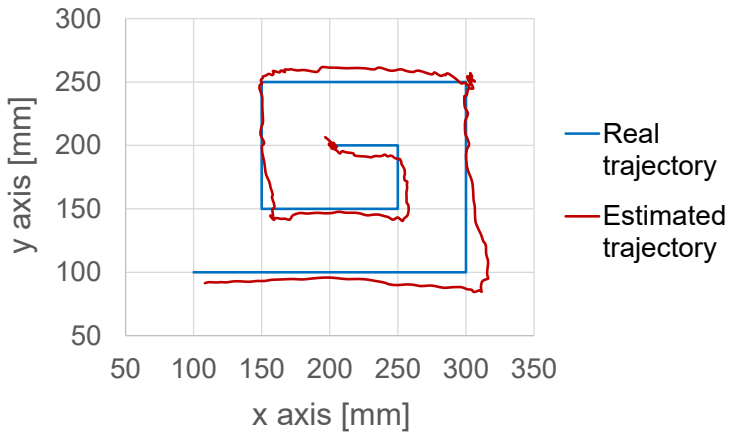

Figure 5.18: Motion tracking result with aluminum plate.

Table 5.1: Time profile of each function.

Function	Execution time [ms]
BLE communication	55.01
Overhead in host PC	6.20
Overhead in MCU	4.77
Total time	65.98 (15.16 Hz)

update rate is 15.16 Hz. In Table 5.1, BLE communication includes only the communication from the host PC to the sensor node because the communication from the sensor node to host PC, which takes a shorter time of 52.47 ms, is completed in parallel to the host PC to sensor communication. Likewise, other functions such as the coil enabling/disabling and measurement are all done in parallel to the BLE communication. Hence, those do not affect the update rate in the current configuration. Thus, the current update rate is mostly determined not by the measurement or computation but by the BLE communication. Therefore, if the wireless communication speed is enhanced, the entire update rate is significantly improved. Section 5.4.2 will introduce the execution times of other functions and discuss the achievable update rate of the proposed motion tracking system.

5.4 Discussion

This section discusses further details about the characteristics of the proposed motion tracking system. Section 5.4.1 investigates the localization error originating from the posture estimation error. Section 5.4.2 discusses the potentially available tracking speed supposing that the performance of the wireless communication circuit is sufficiently enhanced. Section 5.4.3 introduces some motion tracking examples in non-laboratory

daily environments.

5.4.1 Localization error induced by posture estimation error

As explained in Section 5.2, the proposed motion tracking method consists of two steps: 3-DoF posture estimation followed by 3-DoF localization. The localization step requires the estimated posture for the coordinate transformation from the sensor coordinate system to the absolute coordinate system, as explained in Section 5.2.4. Therefore, the posture estimation error invades the localization error through the coordinate transformation. To investigate the influence of the posture estimation performance on the localization error, this section conducts a simulation experiment. For evaluating the effect of the estimation error of a single variable on the localization error, let us assume that only ϕ_{yaw} contains the error and the other two variables, ϕ_{roll} and ϕ_{pitch}, are correctly estimated. Eqs. (5.6), (5.9), and (5.10) indicate that the yaw estimation error propagates to λ, ξ, and θ. ξ is utilized to derive θ, and consequently, the yaw estimation error causes estimation errors of λ and θ, where λ and θ determine the anchor to the sensor direction. To simplify the discussion and focus on the impact of the single variable, we assume $\lambda = 0$, which means all sensor nodes are located in the $xy-$plane. Let three sensor nodes be placed at points $A(100,300,0)$, $B(300,100,0)$, and $C(300,300,0)$, respectively. It is also assumed that all of the sensor axis match the absolute coordinate system, which means $(\phi_{roll}, \phi_{pitch}, \phi_{yaw}) = (0,0,0)$, while the estimated ϕ_{yaw} contains error.

The simulation result in Fig. 5.19 shows that the yaw estimation error degrades the localization accuracy. The localization errors become larger linearly as the yaw estimation error increases. Fig. 5.19 also indicates that the error increasing rate at point C is more significant than those at points A and B. The distance between point C and the reference node is larger than those of points A and B, and hence subtle angle estimation error results in a significant localization error in the xyz space. Here, this work limited the discussion to single variable θ and assumed $\lambda = 0$. If $\lambda \neq 0$, both λ and θ affect the localization error, which would result in a larger error. The discussion revealed that the effect of the yaw estimation error is considerable, even in $\lambda = 0$ situation. Therefore, to enhance the localization accuracy at the points apart from the reference node, we should improve the posture estimation accuracy first.

Besides, apart from the posture estimation error, in Fig. 5.19, we can see that the localization error cannot be zero even when the yaw estimation error is zero. This error originates from the approximation function explained in Section 5.2.4 and can be suppressed by introducing LUT (Look Up Table) or another more precise approximation function.

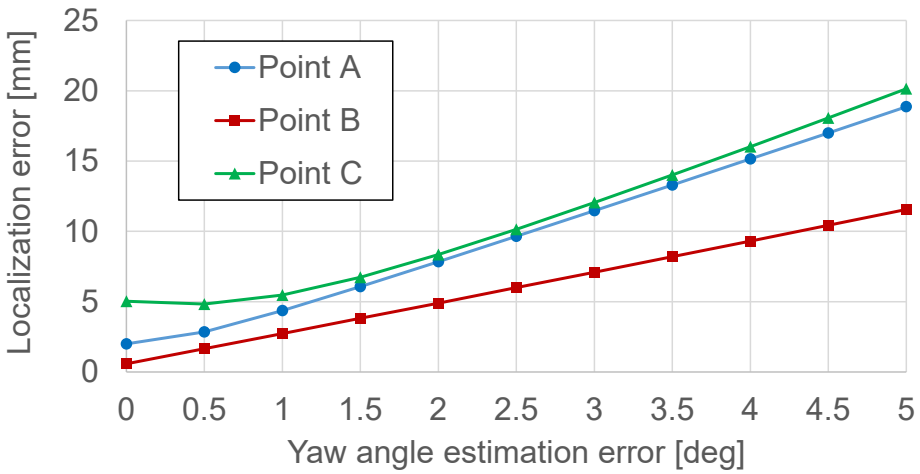

Figure 5.19: Localization error caused by the yaw estimation error.

5.4.2 Potentially available tracking speed

The update rate of the proposed motion tracking method is determined mostly by the BLE communication in the current configuration, as explained in Section 5.3.4. For future system enhancement, on the other hand, this section discusses the potentially available motion tracking speed supposing that the wireless communication speed is sufficiently enhanced.

There are two fundamental functions executed in the proposed system: enabling and disabling the reference coil, and the measurement. The reference coil utilized in the proposed method has a large inductance of 10 mH, and therefore it takes time to stabilize the current flowing through the coil. Fig. 5.20 shows the current change after the constant current source starts to inject the 1A current to the reference coil. The experiment is conducted in two environments, where one contains an aluminum plate, as shown in Fig. 5.17, and the other does not. Fig. 5.20 shows that the required time for the current stabilization is almost identical in both the environments, and the required time is 4.83 ms. Both coil-enabling and coil-disabling take nearly the same time, and hence the overall coil related function takes $4.83 \times 2 = 9.66$ ms.

Also, the sensor node requires the measurement time of accelerometer and magnetometer, and it includes overheads in the host PC and the MCU of the node. Table 5.2 listing those necessary times indicates that the system requires at least 34.58 ms for each localization, and hence the potentially available update rate is 28.92 Hz. Here, please note that the required time for the current stabilization depends on the maximum voltage applied to the coil. Therefore, the potentially available update rate can be higher than 28.92 Hz if we tune the hardware so that the constant current source can drive higher voltage.

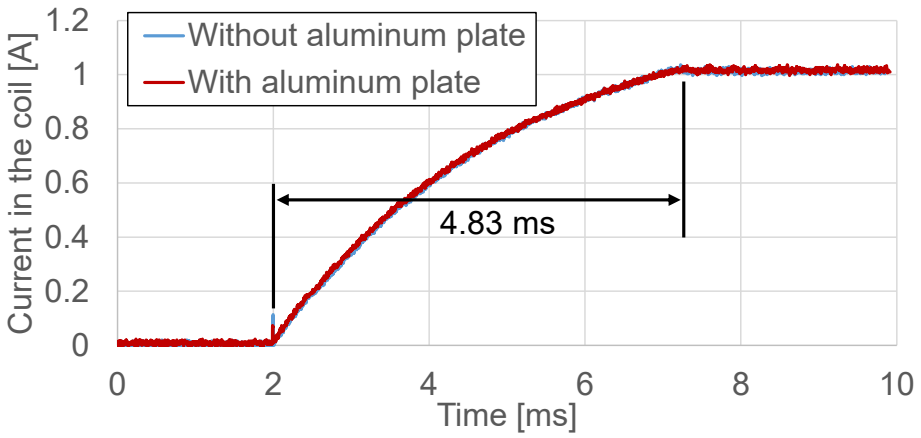

Figure 5.20: Stabilization of the current flowing through the reference coil.

Table 5.2: Time profile of each function.

Function	Execution time [ms]
Measurement of magnetic field	12.9
Measurement of acceleration	1.05
Coil enabling/disabling	9.16
Overhead in host PC	6.20
Overhead in MCU	4.77
total	34.58 (28.92 Hz)

5.4.3 Example in use

Finally, this section sets up some potential use cases and conducts experiments to demonstrate the practicality and the robustness of the proposed motion tracking system.

The purpose of this chapter is, as mentioned several times, to actualize ambient intelligence with an instant motion tracking system. Therefore, this work implemented dozens of trackers and evaluated whether the proposed tracking method can contribute to actualizing ambient intelligence based on LBS. In the proposed system, each tracker is identified by the ID number assigned for wireless communication, and therefore the system can track multiple sensors at the same time.

Fig. 5.21 shows the experimental environment and the system output via the LCD. Fig. 5.21 illustrates that the system estimates not only the position of the trackers but also the working status of the officer and his behavior. In this example, the system estimates the circumstance based on the object positions and the direction of the chair backrest. If the water bottle is moved to near the officer, the system considers that the officer is drinking water. As for the officer's working status, the system monitors the output of the tracker attached to the chair backrest and estimates the condition of

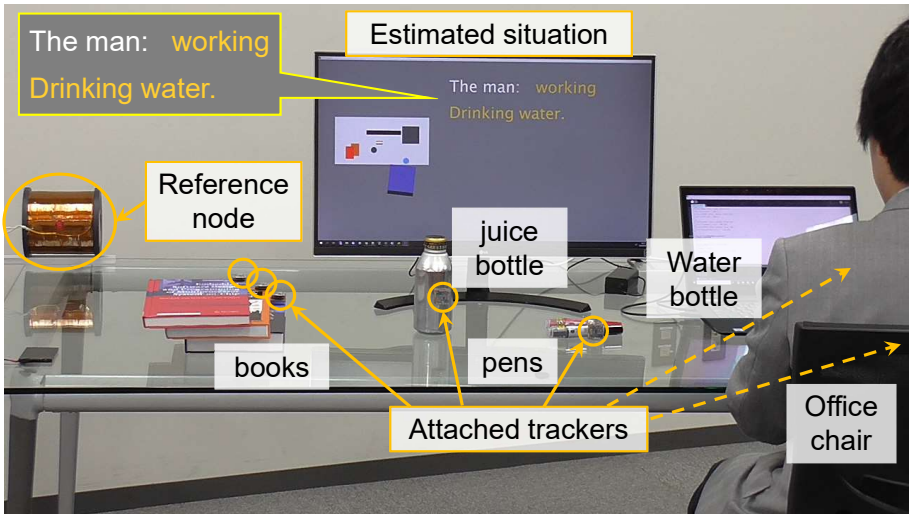

Figure 5.21: The system installed in an office environment with the proposed tracking technology provides a service based on ambient intelligence. The display indicates the estimated situation in addition to the locations of the objects with the trackers.

the office chair, as shown in Fig. 5.22. By sensing the conditions of the office chair, the system can know, for example, whether the officer is working, relaxing, or absent. Needless to say, machine learning techniques help advance the service and improve robustness and accuracy.

The trackers proposed in this chapter can be attached to not only objects but also men. When we attach the trackers to men, the system can estimate, for example, who met or talked to each other frequently, to whom s/he is often facing in the meeting, etc. For the demonstration, this work attached the trackers to two men and conducted an experiment. Fig. 5.23 shows that the system estimates two men are talking to each other based on the positions and directions of them and the facing duration.

The example use cases introduced above require the meter-scale motion tracking, which is indispensable to actualize a room-scale ambient intelligence. The experiments here demonstrate that the proposed system with a larger reference coil is also applicable to meter-scale motion tracking. The experiments in in Section 5.3, on the other hand, have demonstrated that the proposed system can also apply to the tabletop applications, which require a higher update rate and higher tracking accuracy. Also, the proposed system can work in a harsh environment that contains a metallic obstacle. Fig. 5.24 demonstrates that the system can track the sensor nodes even under the occlusion with the metallic plate. Thus, the robustness of the proposed system is experimentally confirmed.

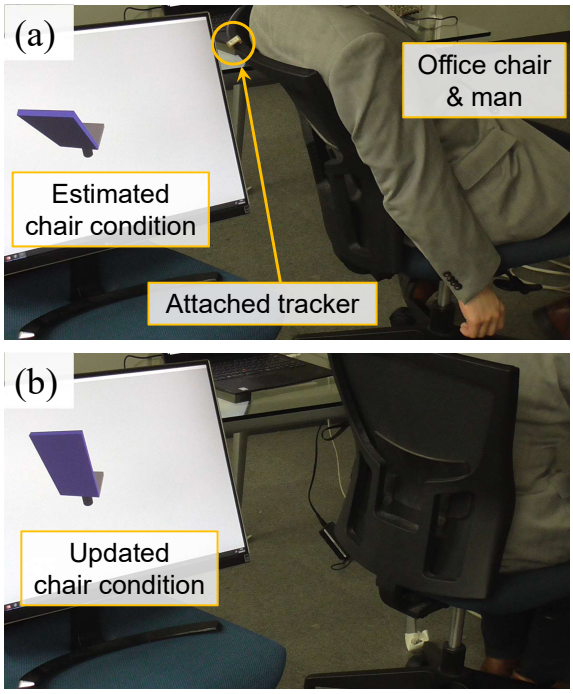

Figure 5.22: A tiny tracker attached to the backrest enables the system to estimate the office chair condition.

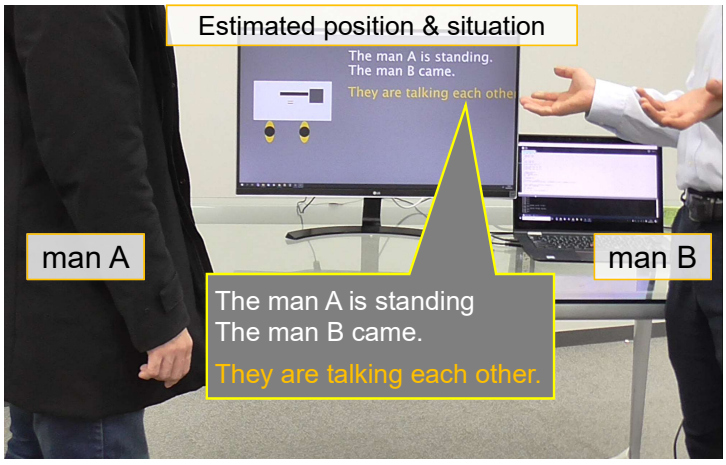

Figure 5.23: The proposed system successfully estimates the positions and directions of the men with the trackers and, as a result, recognizes the situation that they are talking each other.

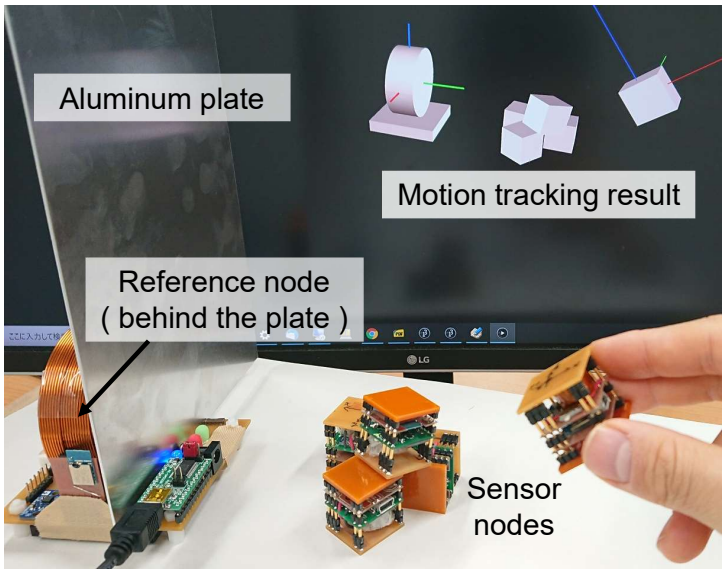

Figure 5.24: The proposed system can track the sensor nodes even when the reference node is occluded by a metallic plate.

5.5 Conclusion and future work

This chapter proposed a DC magnetic field-based 6-DoF motion tracking method with a single reference node. The proposed method is suitable for motion tracking in the daily environment since it can provide not only instant but also robust motion tracking even in the environment containing daily obstacles, which possibly cause occlusion problems and contain metallic material. The proposed method does not require any complex hardware structure or intensive computation, and hence motion tracking is readily enabled. The sensor node, which is used as the tracker, is small and thin, and hence we can attach it to anything around us. This instantness of the proposed method highly contributes to building the infrastructure for ambient intelligence. Although the demonstrated use cases aim to show the feasibility of the instant tracking in the room-scale environment, this chapter experimented in the harsh tabletop environment, which requires higher accuracy and update rate than the room-scale environment, to assess the performance bound of the proposed method. Experimental results showed that the proposed method can estimate the 3-DoF sensor posture of the sensor node with the maximum error of 1.65 degrees and achieved the 3-DoF position estimation with the maximum error of 9.69 mm in the range of 350mm from the reference node. The update rate achieved by the current hardware was 15.16 Hz and enough to provide real-time motion tracking. The update rate of the motion tracking is determined by the time of wireless communication handled by an off-the-shelf BLE circuit. The time profile analysis revealed that the proposed method can track the sensor node with the maximum speed of 28.92 Hz if the performance of the wireless communication is enhanced. Combining the high-performance wireless communication circuit with the proposed method can double the update rate, which is one of the future work.

Chapter 6

Conclusion and future work

6.1 Conclusion

Pervasive sensing technology contributes to IoT and AmI, which are both actively studied recent years since those can enhance our QoL significantly. AmI is currently considered to be the comprehensive concept including IoT and pervasive sensing. To change our daily environment into the AmI supported environment instantly, the tiny wireless tracker which can provide instant pervasive sensing, which is the concept presented in this dissertation, is highly demanded. General wireless tracker for pervasive sensing should be equipped with following three functions to make the tracker itself maintenance free: wireless communication, WPT, and localization. On the other hand, conventionally available technologies on these functions have problems on the sensor volume, feasibility, and the installation cost. To address these issues, this dissertation focused and solved four problems: the wireless communication, the WPT, the localization, and the motion-tracking based AmI.

Chapter 2 addressed the issues of wireless communication and proposed a compact VHF-band transmitter. Two major challenges here are the volume reduction of the transmitter and the start up time reduction of the LC OSC to enhance the energy efficiency per bit. Conventional transmitter structures suffer from the transmitter volume problem since they applied the dedicated antenna for efficient radiation. On the other hand, the size of the dedicated antenna is determined according to the wavelength of the signal, and hence cannot be smaller than a specific value. If the transmitter applies the smaller antenna than the required size, the radiation efficiency is significantly degraded, which is a crucial issue for the energy limited tiny sensor nodes for pervasive sensing. To solve this antenna volume issue, the proposed transmitter uses its equipped coil for radiation as well as oscillation, eliminating the need for an external antenna. With this feature, this work successfully prototyped the transmitter with the volume of 2.8 mm $\times$ 2.8 mm $\times$ 4.2 mm even with the large discrete components. To shorten the start up time of the LC OSC to enhance the energy efficiency, Chapter 2 devised a scheme that provides

a weak current to the coil for quick start of LC oscillation. Measurement results with prototyped transmitter showed that the time required for the stabilization of the oscillation is reduced from 400 ns to 40 ns and the minimum energy consumption of 205 pJ/b is achieved even with the bare baseband signal. Chapter 2 also proposed the energy efficient basedband encoding technique which can reduce the energy per bit from 205 pJ/b to 51.8 pJ/b.

Chapter 3 addressed the issues of WPT. The pervasive sensing requires 1-to-n WPT system, in which one power transmitter is responsible for multiple power receivers, while conventional research mainly has focused on 1-to-1 WPT systems. Three major challenges on WPT for pervasive sensing are to analyze the 1-to-n WPT system theoretically, to confirm the feasibility of the 1-to-n WPT system based on the analysis, and to establish the appropriate WPT receiver structure for the maintenance free pervasive sensor node. To address first two challenges, Chapter 3 derived theoretical formulas based on the circuit analysis and the theory of magnetics and reveled that the 1-to-n WPT system is feasible as long as the circuit constants are appropriately tuned. The simulation result showed that the power transmission efficiency can be more than several dozens of % even with the nearly zero coupling coefficient between the transmitter and receiver coils when the sufficiently large number of power receivers are scattered in the system. As for the WPT receiver circuit, Chaper 3 proposed the power receiver structure with the J-FET that the circuit automatically enters the WPT mode when the inner node energy is not available.

Chapter 4 studied the issue of the localization. Conventional localization methods suffer from the robustness problem since the camera based methods cannot avoid occlusion problem and the general AC magnetic field based methods cannot tolerate daily non-ferrous metallic material. Therefore, the major challenge on the localization for pervasive sensing is to establish the robust localization method with the low installation cost so that the localization function is instantly enabled. To solve this issue, Chapter 4 proposed a DC magnetic field based robust indoor 3D localization method with a single anchor coil. The proposed method estimates the sensor position from both geomagnetism and artificially generated DC magnetic field and is not affected by non-ferrous metallic objects. The proposed method does not require any pre-measurement or multi-anchor nodes in the minimal configuration, and hence it can realize instant 3D localization with lower installation cost. Chapter 4 experimentally evaluated the proposed method supposing tabletop-scale and room-scale applications. For table-top scale applications, the proposed method estimates the 3D position with the maximum error of 6.5 mm in the range of 250 mm. For room-scale applications, which require coverage area expansion with multiple anchor coils, the proposed method localizes the sensor with the maximum error of 14.7 cm in 3.0 m $\times$ 1.5 m area.

Chapter 5 tackled with the issue of the motion-tracking based AmI. Sensor nodes being equipped with only three element functions discussed in Chapters. 2, 3, and 4 acts as motion trackers and shall greatly contributes to AmI since AmI takes advantage

of all information around us including the motion information of sensor nodes. However, conventional motion tracking methods for AmI require the installation of dedicated equipment, which cannot be diverted to other application. Therefore, the major challenge here is to establish an instant motion tracking system that can readily enabled and is robust to our daily stuffs. To address this issue, Chapter 5 proposed an instant magnetic tracking system based on the developed technique in Chapter 4. The proposed tracking system enables us to track the movement and orientation of objects and persons only by attaching tiny electronic trackers to them. Experimental result revealed that the prototyped tracker whose size is 25.4mm $\times$ 25.4mm $\times$ 10.0 mm can estimate the 3-DoF sensor posture of the sensor node with the maximum error of 1.65 degrees and achieved the 3-DoF position estimation with the maximum error of 9.69 mm in the range of 350mm from the reference node. Other experiments conducted to show the practicability of the motion tracking-based AmI indicated that the room-scale motion tracking could estimate the user's behavior and status.

The works in this dissertation contribute to not only the pervasive sensing technology but also AmI and IoT since they take advantage of the pervasive sensing. With the proposed wireless communication method and WPT circuit structure, the sensor nodes become fully wireless and maintenance free. By integrating proposed localization method to the pervasive sensor nodes, the system is now relieved from high installation cost and low robustness. Furthermore, the demonstrated AmI environment with the proposed tracker indicates that our QoL shall be improved when the gathered information is associated with the location information.

6.2 Future work

This dissertation showed the feasibility and implementation of three basic components and the basic motion tracking function with those three components. With the actualized basic components and the function, the effectiveness of the concept of instant pervasive sensing is confirmed in its minimal configuration. However, the instant pervasive sensor node may be equipped with application-specific components to achieve special function to expand its application area as discussed with Fig. 1.10 in Chapter 1. Therefore, the future prospect of this research is to show the effectiveness of the concept of instant pervasive sensing in various applications by incorporating application-specific components into the sensor node. The future work on this prospect is to develop the sensor structure that allows us to easily install the application specific components to the basic sensor node. If the sensor structure which the components and functions are easily configured by user is developed, the application area of the proposed instant pervasive sensing concept expands significantly, and our QoL should be improved consequently.

The wireless trackable sensor node for instant pervasive sensing discussed in this dissertation can be attached not only to objects but also to persons, and allows us to

collect huge comprehensive information from our daily environment. To improve QoL of us human beings by utilizing this comprehensive information, the knowledge of psychology and behavioral science should be utilized as well as data analysis. For this reason, to take full advantage of the information gathered with pervasive sensors, another important future work is to set up a new research field on utilizing and processing this huge information, by collaborating with researchers in areas of data analysis, psychology, and behavioral science.

Bibliography

[1] A. W. Burks, "Electronic computing circuits of the eniac," *Proceedings of the IRE*, vol. 35, no. 8, pp. 756–767, 1947.

[2] A. W. Burks and A. R. Burks, "First general-purpose electronic computer," *Annals of the History of Computing*, vol. 3, no. 4, pp. 310–389, 1981.

[3] M. H. Weik, "A survey of domestic electronic digital computing systems. ballistic research laboratories report no. 971," *Aberdeen Proving Ground, MD: US Department of Commerce Office of Technical Services*, 1955.

[4] H. C. Nathanson, W. E. Newell, R. A. Wickstrom, and J. R. Davis, "The resonant gate transistor," *IEEE Transactions on Electron Devices*, vol. 14, no. 3, pp. 117–133, 1967.

[5] N. Streitz and P. Nixon, "The disappearing computer," *Communications-ACM*, vol. 48, no. 3, pp. 32–35, 2005.

[6] J. C. Augusto, H. Nakashima, and H. Aghajan, "Ambient intelligence and smart environments: A state of the art," in *Handbook of ambient intelligence and smart environments*. Springer, 2010, pp. 3–31.

[7] E. H. Aarts and J. L. Encarnação, *True visions: The emergence of ambient intelligence*. Springer Science & Business Media, 2006.

[8] E. Aarts, R. Harwig, and M. Schuurmans, "The invisible future: the seamless integration of technology into everyday life, chapter ambient intelligence," 2002.

[9] M. Arribas-Ayllon. Ambient intelligence: an innovation narrative. Accessed Nov. 4, 2020. [Online]. Available: https://www.academia.edu/1080720/Ambient_Intelligence_an_innovation_narrative

[10] P. Bellavista, G. Cardone, A. Corradi, and L. Foschini, "Convergence of manet and wsn in iot urban scenarios," *IEEE Sensors Journal*, vol. 13, no. 10, pp. 3558–3567, 2013.

[11] L. Da Xu, W. He, and S. Li, "Internet of things in industries: A survey," *IEEE Transactions on industrial informatics*, vol. 10, no. 4, pp. 2233–2243, 2014.

[12] A. Al-Fuqaha, M. Guizani, M. Mohammadi, M. Aledhari, and M. Ayyash, "Internet of things: A survey on enabling technologies, protocols, and applications," *IEEE communications surveys & tutorials*, vol. 17, no. 4, pp. 2347–2376, 2015.

[13] J. Wilkins. Beyond IoT: pervasive sensing. Accessed Dec. 10, 2020. [Online]. Available: https://www.automation.com/en-us/articles/2016-1/beyond-iot-pervasive-sensing

[14] A. Ricci, M. Grisanti, I. De Munari, and P. Ciampolini, "Improved pervasive sensing with RFID: An ultra-low power baseband processor for UHF tags," *IEEE transactions on very large scale integration (VLSI) systems*, vol. 17, no. 12, pp. 1719–1729, 2009.

[15] N. Davies and S. Clinch, "Pervasive data science," *IEEE Pervasive Computing*, vol. 16, no. 3, pp. 50–58, 2017.

[16] K. Lin, M. Chen, J. Deng, M. M. Hassan, and G. Fortino, "Enhanced fingerprinting and trajectory prediction for IoT localization in smart buildings," *IEEE Transactions on Automation Science and Engineering*, vol. 13, no. 3, pp. 1294–1307, 2016.

[17] C. Perera, A. Zaslavsky, P. Christen, and D. Georgakopoulos, "Context aware computing for the internet of things: A survey," *IEEE communications surveys & tutorials*, vol. 16, no. 1, pp. 414–454, 2013.

[18] M. Botts, G. Percivall, C. Reed, and J. Davidson, "OGC® sensor web enablement: Overview and high level architecture," in *International conference on GeoSensor Networks*. Springer, 2006, pp. 175–190.

[19] B. K. Kim, N. Tomokuni, K. Ohara, T. Tanikawa, K. Ohba, and S. Hirai, "Ubiquitous localization and mapping for robots with ambient intelligence," in *2006 IEEE/RSJ International Conference on Intelligent Robots and Systems*. IEEE, 2006, pp. 4809–4814.

[20] J. M. Rabaey, J. Ammer, T. Karalar, S. Li, B. Otis, M. Sheets, and T. Tuan, "Picoradios for wireless sensor networks: the next challenge in ultra-low power design," in *2002 IEEE International Solid-State Circuits Conference. Digest of Technical Papers (Cat. No. 02CH37315)*, vol. 1. IEEE, 2002, pp. 200–201.

[21] N. Miura, D. Mizoguchi, T. Sakurai, and T. Kuroda, "Analysis and design of inductive coupling and transceiver circuit for inductive inter-chip wireless superconnect," *IEEE Journal of Solid-State Circuits*, vol. 40, no. 4, pp. 829–837, 2005.

[22] D. Guermandi, S. Gambini, and J. Rabaey, "A 1 V 250 kpps 90 nm CMOS pulse based transceiver for cm-range wireless communication," in *ESSCIRC 2007-33rd European Solid-State Circuits Conference*. IEEE, 2007, pp. 135–138.

[23] S. Lee, J. Yoo, and H.-J. Yoo, "A 200-Mbps 0.02-nJ/b dual-mode inductive coupling transceiver for cm-range multimedia application," *IEEE Transactions on Circuits and Systems I: Regular Papers*, vol. 56, no. 5, pp. 1063–1072, 2009.

[24] S. Lee, K. Song, J. Yoo, and H.-J. Yoo, "A low-energy inductive coupling transceiver with cm-range 50-Mbps data communication in mobile device applications," *IEEE journal of solid-state circuits*, vol. 45, no. 11, pp. 2366–2374, 2010.

[25] K. Niitsu, N. Miura, M. Inoue, Y. Nakagawa, M. Tago, M. Mizuno, T. Sakurai, and T. Kuroda, "Daisy chain transmitter for power reduction in inductive-coupling CMOS link," *IEICE transactions on electronics*, vol. 90, no. 4, pp. 829–835, 2007.

[26] N. Miura, K. Kasuga, M. Saito, and T. Kuroda, "An 8Tb/s 1pJ/b 0.8 mm 2/Tb/s QDR inductive-coupling interface between 65nm CMOS GPU and 0.1 μm DRAM," in *2010 IEEE International Solid-State Circuits Conference-(ISSCC)*. IEEE, 2010, pp. 436–437.

[27] N. Miura, D. Mizoguchi, M. Inoue, K. Niitsu, Y. Nakagawa, M. Tago, M. Fukaishi, T. Sakurai, and T. Kuroda, "A 1 Tb/s 3 W inductive-coupling transceiver for 3D-stacked inter-chip clock and data link," *IEEE Journal of Solid-State Circuits*, vol. 42, no. 1, pp. 111–122, 2006.

[28] L. Murata Manufacturing Co. Crystal Units/Crystal Oscillators. Datasheet, Accessed Nov. 4, 2020. [Online]. Available: https://www.murata.com/~/media/webrenewal/support/library/catalog/products/timingdevice/crystalu/p79e.ashx

[29] C.-C. Nguyen, "Microelectromechanical devices for wireless communications," in *Proceedings MEMS 98. IEEE. Eleventh Annual International Workshop on Micro Electro Mechanical Systems. An Investigation of Micro Structures, Sensors, Actuators, Machines and Systems (Cat. No. 98CH36176*. IEEE, 1998, pp. 1–7.

[30] W.-T. Hsu, A. R. Brown, and K. R. Cioffi, "A programmable MEMS FSK transmitter," in *2006 IEEE International Solid State Circuits Conference-Digest of Technical Papers*. IEEE, 2006, pp. 1111–1120.

[31] B. Otis, Y. Chee, R. Lu, N. Pletcher, and J. Rabaey, "An ultra-low power MEMS-based two-channel transceiver for wireless sensor networks," in *2004 Symposium on VLSI Circuits. Digest of Technical Papers (IEEE Cat. No. 04CH37525)*. IEEE, 2004, pp. 20–23.

[32] D. Griffith, E. T.-T. Yen, K. Tsai, T. Kallerud, B. Goodlin *et al.*, "A crystal-less bluetooth low energy radio using a MEMS-based frequency reference system," in *2017 Joint Conference of the European Frequency and Time Forum and IEEE International Frequency Control Symposium (EFTF/IFCS)*. IEEE, 2017, pp. 181–184.

[33] B. Wheeler, F. Maksimovic, N. Baniasadi, S. Mesri, O. Khan, D. Burnett, A. Niknejad, and K. Pister, "Crystal-free narrow-band radios for low-cost IoT," in *2017 IEEE Radio Frequency Integrated Circuits Symposium (RFIC)*. IEEE, 2017, pp. 228–231.

[34] X. Zhang and A. B. Apsel, "A low-power, process-and-temperature-compensated ring oscillator with addition-based current source," *IEEE Transactions on Circuits and Systems I: Regular Papers*, vol. 58, no. 5, pp. 868–878, 2010.

[35] J. Wang, W. L. Goh, X. Liu, and J. Zhou, "A 12.77-MHz 31 ppm/°C on-chip RC relaxation oscillator with digital compensation technique," *IEEE Transactions on Circuits and Systems I: Regular Papers*, vol. 63, no. 11, pp. 1816–1824, 2016.

[36] J. Lee and S. Cho, "A 10MHz 80μW 67 ppm/°C CMOS reference clock oscillator with a temperature compensated feedback loop in 0.18 μm CMOS," in *2009 symposium on VLSI circuits*. IEEE, 2009, pp. 226–227.

[37] M. Choi, T. Jang, S. Bang, Y. Shi, D. Blaauw, and D. Sylvester, "A 110 nW resistive frequency locked on-chip oscillator with 34.3 ppm/°C temperature stability for system-on-chip designs," *IEEE Journal of Solid-State Circuits*, vol. 51, no. 9, pp. 2106–2118, 2016.

[38] O. Khan, B. Wheeler, D. Burnett, F. Maksimovic, S. Mesri, K. Pister, and A. Niknejad, "Frequency reference for crystal free radio," in *2016 IEEE International Frequency Control Symposium (IFCS)*. IEEE, 2016, pp. 1–2.

[39] Y. Wang, K. T. Chai, X. Mu, M. Je, and W. L. Goh, "A 1.5 ± 0.39 ppm/°C temperature-compensated lc oscillator using constant-biased varactors," *IEEE Microwave and Wireless Components Letters*, vol. 25, no. 2, pp. 130–132, 2015.

[40] E. O. Ates, A. Ergul, and D. Y. Aksin, "Fully integrated frequency reference with 1.7 ppm temperature accuracy within 0–80°C," *IEEE journal of solid-state circuits*, vol. 48, no. 11, pp. 2850–2859, 2013.

[41] F. Zhang, M. A. Stoneback, and B. P. Otis, "A 23 μA RF-powered transmitter for biomedical applications," in *2011 IEEE Radio Frequency Integrated Circuits Symposium*. IEEE, 2011, pp. 1–4.

[42] D. Barras, F. Ellinger, H. Jackel, and W. Hirt, "Low-power ultra-wideband wavelets generator with fast start-up circuit," *IEEE Transactions on Microwave Theory and Techniques*, vol. 54, no. 5, pp. 2138–2145, 2006.

[43] J. H. Kim, A. Tazarv, and M. M. Green, "Fast startup of LC VCOs using circuit asymmetries," *IEEE Transactions on Circuits and Systems II: Express Briefs*, vol. 64, no. 10, pp. 1172–1176, 2017.

[44] D. K. Cheng *et al.*, "Fundamentals of engineering electromagnetics," 1993.

[45] N. Tesla, "Apparatus for transmitting electrical energy." Dec. 1 1914, US Patent 1,119,732.

[46] S. Hui, "Planar wireless charging technology for portable electronic products and Qi," *Proceedings of the IEEE*, vol. 101, no. 6, pp. 1290–1301, 2013.

[47] Z. Bi, T. Kan, C. C. Mi, Y. Zhang, Z. Zhao, and G. A. Keoleian, "A review of wireless power transfer for electric vehicles: Prospects to enhance sustainable mobility," *Applied Energy*, vol. 179, pp. 413–425, 2016.

[48] A. Daga, J. M. Miller, B. R. Long, R. Kacergis, P. Schrafel, and J. Wolgemuth, "Electric fuel pumps for wireless power transfer: Enabling rapid growth in the electric vehicle market," *IEEE Power Electronics Magazine*, vol. 4, no. 2, pp. 24–35, 2017.

[49] F. Lu, H. Zhang, and C. Mi, "A review on the recent development of capacitive wireless power transfer technology," *Energies*, vol. 10, no. 11, p. 1752, 2017.

[50] P. S. Riehl, A. Satyamoorthy, H. Akram, Y.-C. Yen, J.-C. Yang, B. Juan, C.-M. Lee, F.-C. Lin, V. Muratov, W. Plumb *et al.*, "Wireless power systems for mobile devices supporting inductive and resonant operating modes," *IEEE Transactions on Microwave Theory and Techniques*, vol. 63, no. 3, pp. 780–790, 2015.

[51] N. Oodachi, H. Kudo, K. Ogawa, H. Shoki, S. Obayashi, and T. Morooka, "Efficiency improvement of wireless power transfer via magnetic resonance using the third coil," *ISAP 2010, paper ID*, vol. 52, 2010.

[52] A. M. Jawad, R. Nordin, S. K. Gharghan, H. M. Jawad, and M. Ismail, "Opportunities and challenges for near-field wireless power transfer: A review," *Energies*, vol. 10, no. 7, p. 1022, 2017.

[53] G. K. Ottman, H. F. Hofmann, A. C. Bhatt, and G. A. Lesieutre, "Adaptive piezoelectric energy harvesting circuit for wireless remote power supply," *IEEE Transactions on power electronics*, vol. 17, no. 5, pp. 669–676, 2002.

[54] H. F. Leung and A. P. Hu, "Modeling the contact interface of ultrasonic power transfer system based on mechanical and electrical equivalence," *IEEE Journal of Emerging and Selected Topics in Power Electronics*, vol. 6, no. 2, pp. 800–811, 2017.

[55] V. F.-G. Tseng, S. S. Bedair, and N. Lazarus, "Acoustic wireless power transfer with receiver array for enhanced performance," in *2017 IEEE Wireless Power Transfer Conference (WPTC)*. IEEE, 2017, pp. 1–4.

[56] M. G. Roes, J. L. Duarte, M. A. Hendrix, and E. A. Lomonova, "Acoustic energy transfer: A review," *IEEE Transactions on Industrial Electronics*, vol. 60, no. 1, pp. 242–248, 2012.

[57] A. Denisov and E. Yeatman, "Ultrasonic vs. inductive power delivery for miniature biomedical implants," in *2010 International Conference on Body Sensor Networks*. IEEE, 2010, pp. 84–89.

[58] V. F.-G. Tseng, S. S. Bedair, and N. Lazarus, "Phased array focusing for acoustic wireless power transfer," *IEEE transactions on ultrasonics, ferroelectrics, and frequency control*, vol. 65, no. 1, pp. 39–49, 2017.

[59] X. Bao, W. Biederman, S. Sherrit, M. Badescu, Y. Bar-Cohen, C. Jones, J. Aldrich, and Z. Chang, "High-power piezoelectric acoustic-electric power feedthru for metal walls," in *Industrial and Commercial Applications of Smart Structures Technologies 2008*, vol. 6930. International Society for Optics and Photonics, 2008, p. 69300Z.

[60] S. D. Jarvis, J. Mukherjee, M. Perren, and S. J. Sweeney, "Development and characterisation of laser power converters for optical power transfer applications," *Iet Optoelectronics*, vol. 8, no. 2, pp. 64–70, 2014.

[61] J. Fakidis, S. Videv, S. Kucera, H. Claussen, and H. Haas, "Indoor optical wireless power transfer to small cells at nighttime," *Journal of Lightwave Technology*, vol. 34, no. 13, pp. 3236–3258, 2016.

[62] V. Iyer, E. Bayati, R. Nandakumar, A. Majumdar, and S. Gollakota, "Charging a smartphone across a room using lasers," *Proceedings of the ACM on Interactive, Mobile, Wearable and Ubiquitous Technologies*, vol. 1, no. 4, pp. 1–21, 2018.

[63] N. Shinohara, "Beam control technologies with a high-efficiency phased array for microwave power transmission in japan," *Proceedings of the IEEE*, vol. 101, no. 6, pp. 1448–1463, 2013.

[64] K. Huang and X. Zhou, "Cutting the last wires for mobile communications by microwave power transfer," *IEEE Communications Magazine*, vol. 53, no. 6, pp. 86–93, 2015.

[65] E. Y. Chow, C.-L. Yang, Y. Ouyang, A. L. Chlebowski, P. P. Irazoqui, and W. J. Chappell, "Wireless powering and the study of rf propagation through ocular tissue for development of implantable sensors," *IEEE Transactions on Antennas and Propagation*, vol. 59, no. 6, pp. 2379–2387, 2011.

[66] J. Dai and D. C. Ludois, "A survey of wireless power transfer and a critical comparison of inductive and capacitive coupling for small gap applications," *IEEE Transactions on Power Electronics*, vol. 30, no. 11, pp. 6017–6029, 2015.

[67] G. A. Covic and J. T. Boys, "Inductive power transfer," *Proceedings of the IEEE*, vol. 101, no. 6, pp. 1276–1289, 2013.

[68] A. Kurs, A. Karalis, R. Moffatt, J. D. Joannopoulos, P. Fisher, and M. Soljačić, "Wireless power transfer via strongly coupled magnetic resonances," *science*, vol. 317, no. 5834, pp. 83–86, 2007.

[69] J. Xia, X. Yuan, J. Li, S. Lu, X. Cui, S. Li, and L. M. Fernández-Ramírez, "Foreign object detection for electric vehicle wireless charging," *Electronics*, vol. 9, no. 5, p. 805, 2020.

[70] S. Kim, J. S. Ho, L. Y. Chen, and A. S. Poon, "Wireless power transfer to a cardiac implant," *Applied Physics Letters*, vol. 101, no. 7, p. 073701, 2012.

[71] IEEE Standards Coordinating Committee *et al.*, "IEEE standard for safety levels with respect to human exposure to radio frequency electromagnetic fields, 3kHz to 300GHz," *IEEE C95. 1-1991*, 1992.

[72] A. S. Poon, S. O'Driscoll, and T. H. Meng, "Optimal frequency for wireless power transmission into dispersive tissue," *IEEE Transactions on Antennas and Propagation*, vol. 58, no. 5, pp. 1739–1750, 2010.

[73] M. Mark, T. Björninen, L. Ukkonen, L. Sydänheimo, and J. M. Rabaey, "SAR reduction and link optimization for mm-size remotely powered wireless implants using segmented loop antennas," in *2011 IEEE Topical Conference on Biomedical Wireless Technologies, Networks, and Sensing Systems*. IEEE, 2011, pp. 7–10.

[74] Y.-T. Liao, H. Yao, A. Lingley, B. Parviz, and B. P. Otis, "A 3-μW CMOS glucose sensor for wireless contact-lens tear glucose monitoring," *IEEE Journal of Solid-State Circuits*, vol. 47, no. 1, pp. 335–344, 2011.

[75] N. Kuyvenhoven, C. Dean, J. Melton, J. Schwannecke, and A. Umenei, "Development of a foreign object detection and analysis method for wireless power systems," in *2011 IEEE Symposium on Product Compliance Engineering Proceedings*. IEEE, 2011, pp. 1–6.

[76] Wireless Power Consortium *et al.*, "System description wireless power transfer volume I: Low power part 1: Interface definition version 1.1," 2012.

[77] Y.-C. Wang and C.-W. Chiang, "Foreign metal detection by coil impedance for ev wireless charging system," in *Proceedings of the EVS28 International Electric Vehicle Symposium Exhibition, KINTEX, Goyang, Korea*, 2015, pp. 3–6.

[78] Z. N. Low, J. J. Casanova, P. H. Maier, J. A. Taylor, R. A. Chinga, and J. Lin, "Method of load/fault detection for loosely coupled planar wireless power transfer system with power delivery tracking," *IEEE Transactions on Industrial Electronics*, vol. 57, no. 4, pp. 1478–1486, 2009.

[79] S.-J. Huang, J.-L. Su, S.-H. Dai, C.-C. Tai, and T.-S. Lee, "Enhancement of wireless power transmission with foreign-object detection considerations," in *2017 IEEE 6th Global Conference on Consumer Electronics (GCCE)*. IEEE, 2017, pp. 1–2.

[80] C.-J. Chen, T.-H. Chu, C.-L. Lin, and Z.-C. Jou, "A study of loosely coupled coils for wireless power transfer," *IEEE Transactions on Circuits and Systems II: Express Briefs*, vol. 57, no. 7, pp. 536–540, 2010.

[81] D.-W. Seo, J.-H. Lee, and H. S. Lee, "Study on two-coil and four-coil wireless power transfer systems using Z-parameter approach," *ETRI Journal*, vol. 38, no. 3, pp. 568–578, 2016.

[82] D.-W. Seo, "Comparative analysis of two-and three-coil WPT systems based on transmission efficiency," *IEEE Access*, vol. 7, pp. 151 962–151 970, 2019.

[83] H.-J. Chu, G.-J. Tsai, K.-W. Chiang, and T.-T. Duong, "GPS/MEMS INS data fusion and map matching in urban areas," *Sensors*, vol. 13, no. 9, pp. 11 280–11 288, 2013.

[84] H. Liu, H. Darabi, P. Banerjee, and J. Liu, "Survey of wireless indoor positioning techniques and systems," *IEEE Transactions on Systems, Man, and Cybernetics, Part C (Applications and Reviews)*, vol. 37, no. 6, pp. 1067–1080, 2007.

[85] M. Andries, O. Simonin, and F. Charpillet, "Localization of humans, objects, and robots interacting on load-sensing floors," *IEEE Sensors Journal*, vol. 16, no. 4, pp. 1026–1037, 2015.

[86] F.-j. Zhu, Z.-h. Wei, B.-j. Hu, J.-g. Chen, and Z.-m. Guo, "Analysis of indoor positioning approaches based on active RFID," in *Wireless Communications, Networking and Mobile Computing, 2009. WiCom'09. 5th International Conference on*. IEEE, 2009, pp. 1–4.

[87] S. He and S.-H. G. Chan, "Wi-Fi fingerprint-based indoor positioning: Recent advances and comparisons," *IEEE Communications Surveys & Tutorials*, vol. 18, no. 1, pp. 466–490, 2016.

[88] C. Yang and H.-R. Shao, "WiFi-based indoor positioning," *IEEE Communications Magazine*, vol. 53, no. 3, pp. 150–157, 2015.

[89] C. Wu, Z. Yang, Y. Liu, and W. Xi, "WILL: Wireless indoor localization without site survey," *IEEE Transactions on Parallel and Distributed Systems*, vol. 24, no. 4, pp. 839–848, 2013.

[90] F. Zafari, I. Papapanagiotou, and K. Christidis, "Microlocation for internet-of-things-equipped smart buildings," *IEEE Internet of Things Journal*, vol. 3, no. 1, pp. 96–112, 2016.

[91] R. Figueiredo, A. Dehban, A. Bernardino, J. Santos-Victor, and H. Araújo, "Shape-based attention for identification and localization of cylindrical objects," in *IEEE International Conference on Development and Learning and on Epigenetic Robotics (ICDL-EpiRob)*, vol. 18, 2017, p. 21.

[92] D. Murray and A. Basu, "Motion tracking with an active camera," *IEEE transactions on pattern analysis and machine intelligence*, vol. 16, no. 5, pp. 449–459, 1994.

[93] K. Kjærside, K. J. Kortbek, H. Hedegaard, and K. Grønbæk, "Ardresscode: augmented dressing room with tag-based motion tracking and real-time clothes simulation," in *Proceedings of the central european multimedia and virtual reality conference*, 2005.

[94] V. Pasku, A. De Angelis, G. De Angelis, D. D. Arumugam, M. Dionigi, P. Carbone, A. Moschitta, and D. S. Ricketts, "Magnetic field-based positioning systems," *IEEE Communications Surveys & Tutorials*, vol. 19, no. 3, pp. 2003–2017, 2017.

[95] G. De Angelis, V. Pasku, A. De Angelis, M. Dionigi, M. Mongiardo, A. Moschitta, and P. Carbone, "An indoor AC magnetic positioning system," *IEEE Transactions on Instrumentation and Measurement*, vol. 64, no. 5, pp. 1267–1275, 2015.

[96] J. Blankenbach, A. Norrdine, and H. Hellmers, "A robust and precise 3D indoor positioning system for harsh environments," in *Indoor Positioning and Indoor Navigation (IPIN), 2012 International Conference on*. IEEE, 2012, pp. 1–8.

[97] W. Kim, J. Song, and F. C. Park, "Closed-form position and orientation estimation for a three-axis electromagnetic tracking system," *IEEE Transactions on Industrial Electronics*, vol. 65, no. 5, pp. 4331–4337, 2017.

[98] J. Huang, T. Mori, K. Takashima, S. Hashi, and Y. Kitamura, "IM6D: magnetic tracking system with 6-DOF passive markers for dexterous 3D interaction and motion," *ACM Transactions on Graphics (TOG)*, vol. 34, no. 6, p. 217, 2015.

[99] K.-Y. Chen, S. N. Patel, and S. Keller, "Finexus: Tracking precise motions of multiple fingertips using magnetic sensing," in *Proceedings of the 2016 CHI Conference on Human Factors in Computing Systems*, 2016, pp. 1504–1514.

[100] E. Whitmire, L. Trutoiu, R. Cavin, D. Perek, B. Scally, J. Phillips, and S. Patel, "Eyecontact: scleral coil eye tracking for virtual reality," in *Proceedings of the 2016 ACM International Symposium on Wearable Computers*, 2016, pp. 184–191.

[101] F. S. Parizi, E. Whitmire, and S. Patel, "AuraRing: Precise electromagnetic finger tracking," *Proceedings of the ACM on Interactive, Mobile, Wearable and Ubiquitous Technologies*, vol. 3, no. 4, pp. 1–28, 2019.

[102] E. Whitmire, F. Salemi Parizi, and S. Patel, "Aura: Inside-out electromagnetic controller tracking," in *Proceedings of the 17th Annual International Conference on Mobile Systems, Applications, and Services*, 2019, pp. 300–312.

[103] J. Blankenbach, A. Norrdine, H. Hellmers, and E. Gasparian, "A novel magnetic indoor positioning system for indoor location services," in *Proceedings of the 8th International Symposium on Location-Based Services*, 2011, pp. 1–11.

[104] P. H. Chen, R. Shirai, and M. Hashimoto, "Coverage-scalable instant tabletop positioning system with self-localizable anchor nodes," in *Proceedings of the 24th International Conference on Intelligent User Interfaces: Companion*. ACM, 2019, pp. 57–58.

[105] S. Song, C. Hu, B. Li, X. Li, and M.-H. Meng, "An electromagnetic localization and orientation method based on rotating magnetic dipole," *IEEE Transactions on Magnetics*, vol. 49, no. 3, pp. 1274–1277, 2013.

[106] J. M. DiMicco, A. Pandolfo, and W. Bender, "Influencing group participation with a shared display," in *Proceedings of the 2004 ACM conference on Computer supported cooperative work*, 2004, pp. 614–623.

[107] K. Ara, N. Kanehira, D. O. Olguin, B. N. Waber, T. Kim, A. Mohan, P. Gloor, R. Laubacher, D. Oster, A. S. Pentland *et al.*, "Sensible organizations: Changing our businesses and work styles through sensor data," *Journal of Information Processing*, vol. 16, pp. 1–12, 2008.

[108] T. Bergstrom and K. Karahalios, "Conversation votes: enabling anonymous cues," in *CHI'07 Extended Abstracts on Human Factors in Computing Systems*, 2007, pp. 2279–2284.

[109] T. Bergstrom and K. Karahalios, "Conversation Clock: Visualizing audio patterns in co-located groups," in *2007 40th Annual Hawaii International Conference on System Sciences (HICSS'07)*. IEEE, 2007, pp. 78–78.

[110] A. Madan and A. S. Pentland, "Vibefones: Socially aware mobile phones," in *2006 10th IEEE International Symposium on Wearable Computers*. IEEE, 2006, pp. 109–112.

[111] T. Kim, A. Chang, L. Holland, and A. S. Pentland, "Meeting mediator: enhancing group collaborationusing sociometric feedback," in *Proceedings of the 2008 ACM conference on Computer supported cooperative work*, 2008, pp. 457–466.

[112] K. Fujita, Y. Itoh, H. Ohsaki, N. Ono, K. Kagawa, K. Takashima, S. Tsugawa, K. Nakajima, Y. Hayashi, and F. Kishino, "Ambient Suite: enhancing communication among multiple participants," in *Proceedings of the 8th International Conference on Advances in Computer Entertainment Technology*, 2011, pp. 1–8.

[113] K. Fujita, Y. Itoh, K. Takashima, K. Nakajima, Y. Hayashi, and F. Kishino, "Ambient party room: A room-shaped system enhancing communication for parties or gatherings," in *2013 IEEE Virtual Reality (VR)*. IEEE, 2013, pp. 1–4.

[114] R. van Langevelde, M. van Elzakker, D. van Goor, H. Termeer, J. Moss, and A. Davie, "An ultra-low-power 868/915 MHz RF transceiver for wireless sensor network applications," in *2009 IEEE Radio Frequency Integrated Circuits Symposium*. IEEE, 2009, pp. 113–116.

[115] J. Bae, L. Yan, and H.-J. Yoo, "A low energy injection-locked FSK transceiver with frequency-to-amplitude conversion for body sensor applications," *IEEE Journal of Solid-state circuits*, vol. 46, no. 4, pp. 928–937, 2011.

[116] A. Moradi and M. Sawan, "An energy-efficient high data-rate 915 MHz FSK wireless transmitter for medical applications," *Analog Integrated Circuits and Signal Processing*, vol. 83, no. 1, pp. 85–94, 2015.

[117] C.-S. Wang, G. A. Covic, and O. H. Stielau, "Power transfer capability and bifurcation phenomena of loosely coupled inductive power transfer systems," *IEEE transactions on industrial electronics*, vol. 51, no. 1, pp. 148–157, 2004.

[118] W. Zhang, S.-C. Wong, K. T. Chi, and Q. Chen, "Analysis and comparison of secondary series-and parallel-compensated inductive power transfer systems operating for optimal efficiency and load-independent voltage-transfer ratio," *IEEE Transactions on Power Electronics*, vol. 29, no. 6, pp. 2979–2990, 2013.

[119] K. Aditya and S. S. Williamson, "Comparative study of Series-Series and Series-Parallel compensation topologies for electric vehicle charging," in *2014 IEEE*

23rd international symposium on industrial electronics (ISIE). IEEE, 2014, pp. 426–430.

[120] R. Ota, N. Hoshi, and J. Haruna, "Design of compensation capacitor in S/P topology of inductive power transfer system with buck or boost converter on secondary side," *IEEJ Journal of Industry Applications*, vol. 4, no. 4, pp. 476–485, 2015.

[121] Y. H. Sohn, B. H. Choi, E. S. Lee, G. C. Lim, G.-H. Cho, and C. T. Rim, "General unified analyses of two-capacitor inductive power transfer systems: Equivalence of current-source SS and SP compensations," *IEEE Transactions on Power Electronics*, vol. 30, no. 11, pp. 6030–6045, 2015.

[122] F. Ternan, "Radio engineers handbook," *New York, McGraw-Hill Book Co*, p. 472, 1943.

[123] S. LaScalza, J. Arico, and R. Hughes, "Effect of metal and sampling rate on accuracy of flock of birds electromagnetic tracking system," *Journal of biomechanics*, vol. 36, no. 1, pp. 141–144, 2003.

[124] T. Ozyagcilar, "Implementing a tilt-compensated ecompass using accelerometer and magnetometer sensors," *Freescale semiconductor, AN*, vol. 4248, 2012.

[125] K. Liu, X. Liu, and X. Li, "Guoguo: Enabling fine-grained indoor localization via smartphone," in *Proceeding of the 11th annual international conference on Mobile systems, applications, and services*, 2013, pp. 235–248.

[126] S. Microelectronics, "LSM9DS1 iNEMO inertial module: 3D accelerometer, 3D gyroscope, 3D magnetometer," *LSM9DS1 datasheet, Mar*, 2015.